Chinese Journal of Catalysis 43 (2022) 2057–2090

available at www.sciencedirect.com

ScienceDirect

journal homepage: www.sciencedirect.com/journal/chinese-journal-of-catalysis

Review

MXenes for electrocatalysis applications: Modification and hybridization

Xue Bai, Jingqi Guan *

Institute of Physical Chemistry, College of Chemistry, Jilin University, Changchun 130021, Jilin, China

ARTICLE INFO

Article history:
Received 25 December 2021
Accepted 28 January 2022
Available online 20 June 2022

Keywords:
Hydrogen evolution reaction
MXene
Oxygen evolution reaction
Oxygen reduction reaction
Water splitting

ABSTRACT

Two-dimensional carbides, nitrides, and carbonitrides (MXenes) play important roles in promoting the development of sustainable energy because they have abundant reactive sites on their surfaces. An increasing number of MXenes with diverse elements and composites have been predicted and synthesized for electrocatalysis applications since the first report of a Ti-Mo-based MXene for the hydrogen evolution reaction (HER). Herein, we summarize the progress of MXene-based electrocatalysts for the HER, the oxygen evolution reaction, and the oxygen reduction reaction, including regulated pristine MXenes and modified hybrid MXenes, from both theoretical and experimental perspectives. A brief overview on MXene synthesis is presented first, accompanied by a discussion on the relationship between electrocatalytic properties and M, X, T, vacancies, and morphologies. After reviewing strategies in terms of atom substitution, functional modification, defect engineering, and morphology control, we emphasize the construction of heterojunctions between MXenes and other nanostructures, such as metal nanoparticles, oxides, hydroxides, sulfides, and phosphides. We finally discuss prospects for the future development of MXene-based electrocatalysts.

1. Introduction

The impending depletion of fossil fuels and irreversible environmental pollution require more research devoted to developing sustainable energy. The development of green and efficient approaches to producing renewable fuels is an acknowledged strategy that satisfies energy demands while reducing CO_2 emissions. Electrochemical processes are important for expanding clean energy. H_2O, N_2, CO_2, and O_2, which are abundant on Earth, can be transformed into fuels and chemicals by appropriate electrocatalysis [1,2]. For example, water electrolysis, which involves the hydrogen and oxygen evolution reactions (HER and OER), produces hydrogen, and hydrogen peroxide, which is the product of the oxygen reduction reaction (ORR) and is an oxidant/bleach commonly used in industry. Unfortunately, highly efficient electrocatalysts are usually based on precious metals, which limits the wide applicability of electrocatalysis. Therefore, the development of highly active and cost-effective electrocatalysts is a crucial objective.

Two-dimensional (2D) layered materials (graphene oxide, molybdenum disulfide, layered double hydroxides, etc.) have attracted significant interest owing to their unique electronic and structural properties [3–6]. As a new family of two-dimensional materials, transition metal carbides, nitrides, and carbonitrides (MXenes) have been widely used in photo/electrocatalysis [7–9], energy storage [10–14], electromagnetic interference shielding [15–18], sensing [19–21], and oth-

* Corresponding author. E-mail: guanjq@jlu.edu.cn
This work was supported by the National Natural Science Foundation of China (22075099) and the Education Department of Jilin Province (JJKH20220967KJ).
DOI: 10.1016/S1872-2067(21)64030-5 | http://www.sciencedirect.com/journal/chinese-journal-of-catalysis | Chin. J. Catal., Vol. 43, No. 8, August 2022

er electrochemical fields since they were first discovered in 2011. An MXene has the general formula $M_{n+1}X_n$ (n = 1–3), where M is an early transition metal, X is carbon or nitrogen, and the M and X atomic layers alternate (Fig. 1) [22]. However, an MXene is usually present in the form of $M_{n+1}X_nT_x$, where T represents surface functional groups (–O, –OH, or –F), because the exposed layers of metal atoms are inevitably oxidized. Significantly, $M_5X_4T_x$ (with nine atomic layers) has been successfully synthesized, which further strengthens the MXene family [23,24].

Qiao *et al*. synthesized a C_3N_4/Ti_3C_2 hybrid film that exhibits OER activity with an overpotential (η_{10}) of 420 mV at 10 mA cm^{-2}, demonstrating the use of an MXene-based hybrid in electrocatalysis for the first time [25]. Vojvodic *et al*. [26] subsequently reported that pristine Mo_2CT_x and Ti_2CT_x are HER active both theoretically and experientially. In contrast to other 2D materials, some MXenes showed good HER performance on both their edge and basal planes owing to the abundance of metal and functional group sites that not only act as HER active sites but also provide hydrophilicity and conductivity. Sites containing the F-functional group are considered advantageous for the ORR because they adsorb and activate O_2, while the O-functional group adsorbs suitable HER intermediates. While highly adjustable and accessible O-, OH-, or F-functional groups can be optimized to enhance electrocatalytic properties, this strategy is generally insufficient for wide electrocatalysis applications. Heteroatoms (B, C, N, S, etc.) are doped into the $M_{n+1}X_nT_x$ lattice to replace the original M, X, and T atoms when optimizing the electronic structure of an MXene at the atomic scale, resulting in enhanced HER and additional OER/ORR activity. Such substitutions and adsorptions in an MXene change its electronic environment and coordination structure, which lowers the reaction energy barrier. Using low-temperature plasma techniques, Guo introduced N into $Ti_3C_2T_x$ using mixed NH_3/Ar plasma, which lowered the ΔG_{max} values of the HER and OER from 2.82 and 2.33 V to 0.92 and 1.83V, respectively [27]. The ΔG_H of B-doped Ti_2CO_2 was calculated to be −0.097 V [28]. However, owing to the small variety and poor stabilities of existing MXenes, previous doping and substitution experiments led to limited improvements in the electrocatalytic performance of the original MXenes, while MXene-based composites displayed better performance. Shapter *et al*. synthesized Ru@B-$Ti_3C_2T_x$ by decorating B-doped Ti_2CO_2 with Ru NPs, which led to a further decrease in ΔG_H to 0.002 V [29]. Apart from metal nanoparticles, MXenes have been decorated with other highly active materials, including, oxides, sulfides, phosphates, and carbon materials, among others [30]. Rout *et al*. [31] loaded $NiFe_2O_4$ NPs onto Ti_3C_2 to produce a sandwich structure that displayed bifunctional electrocatalytic HER/OER activity in 0.5 mol/L KOH. The *in-situ* growth of active species on MXenes is generally an effective strategy for the syntheses of high-performance hybrids that not only inherit the intrinsic activity of the MXene, but also contains new sites that catalyze the HER, OER, and ORR. Moreover, MXenes display excellent potential in other electrocatalytic reactions, such as the N_2 reduction reaction (NRR) [32–35], CO_2 reduction reaction (CO_2RR) [36–40], and methanol oxidation reaction (MOR) [41–44], among others. The abundant OH-terminal groups in $Ti_3C_2T_x$ were shown to favor the NRR by DFT calculations and experimentally [45]. However, Zheng *et al*. [46] reported an NRR catalyst (F-$Ti_3C_2T_x$), in which F-termini accounted for 48% of all terminal groups. O-vacancy-containing MoO_3, which was grown *in situ* on $Ti_3C_2T_x$, also showed the ability to bind intermediates in the NRR [47]. The ability of a Ti-based MXene to resist carbon monoxide poisoning has been reported, thereby greatly improving the stability of the MOR catalyst [48,49].

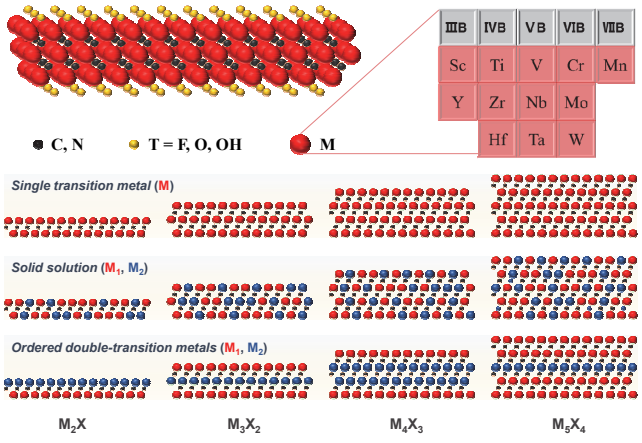

Fig. 1. Structural diagrams of typical MXenes.

MXene-based electrocatalyst design and synthesis advancements involving hybrid or other methods have recently been reported. In this review, we begin by discussing MXene preparation and the effects of atomic species, terminal functional groups, defects, and dimensions on their HER, OER, and ORR performance, and conclude with a strategy for modifying MXene-based electrocatalysts that involves theoretical calculations and experiments. Improving kinetics by increasing the number of active sites and promoting thermodynamics by increasing the intrinsic catalytic activity of the active sites are the two main strategies adopted. Specific strategies for enhancing MXene catalytic activity include functional modification, atom substitution, defect engineering, morphology control, and heterojunction construction. We finally discuss prospects for the future development of MXene-based electrocatalysts.

2. MXene fundamentals for the electrocatalytic HER/OER/ORR

2.1. Basic concepts and computational methods

In a similar manner to conventional catalysis, the active sites of an electrocatalyst aid the reaction process by reducing the activation energy through the formation of suitable intermediates, thereby accelerating the reaction. An electrocatalyst is mainly assessed in terms of its overpotential, Tafel slope, and Faraday efficiency (FE), among others. The overpotential is the difference between the actual voltage required to drive the reaction and the theoretical voltage required by thermodynamics. The Tafel slope is an indicator of the reaction rate; it represents the additional voltage required to increase the current density by a factor of ten, while the FE is the participation

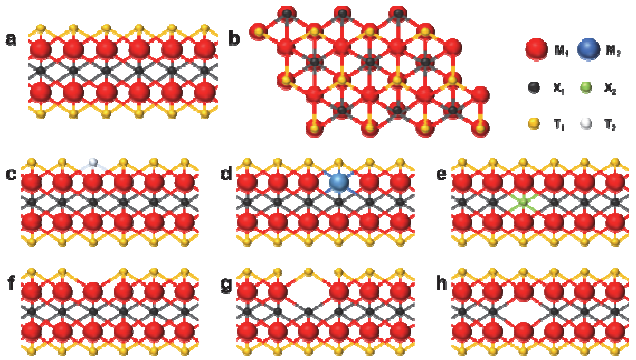

Fig. 2. Theoretical calculational model of an MXene. Side (a) and top (b) views of a pristine MXene; Side views of T-doped (c), M-doped (d), and X-doped (e) MXenes; Side views of V_T-MXene (f), V_M-MXene (g); and V_X-MXene (h).

efficiency of an input electron in a specified reaction in the electrocatalytic system.

In addition, the Gibbs free energy for adsorption (ΔG_{ads}) is a vital thermodynamic catalysts parameter. According to the Sabatier principle, reactants are adsorbed and desorbed during catalytic reactions. Therefore, moderate bonding, in which active site $\Delta G_{ads} = 0$, is the thermodynamic basis of catalysis. Density functional theory (DFT) is a low-cost computational method for estimating ΔG_{ads} that uses a computational hydrogen electrode (CHE). DFT calculations involve the following steps: (1) The construction of a catalyst model and the identification of potential active sites, which is easy for well-ordered MXenes (Fig. 2). The formation energy of the built model is calculated to determine material rationality. (2) Intermediates formed by the reactants at the active site are then predicted. For the HER, DFT calculations focus on the thermodynamics of proton/electron transfer between H atoms and active sites at a given potential. Every intermediate and charge-transfer process should ideally be accurately calculated for more complex processes, which is challenging. In addition, to better approach a realistic electrocatalyst system, electrode-surface polarization following voltage application and solvent effects are also simulated, taking dynamic effects into account. (3) The calculated ΔG_{ads} values are plotted as volcano plots to predict the application potentials of various materials in the electrocatalysis process. In addition, the density of states (DOS) of the system can also be calculated by DFT, with Fermi levels lying in the conduction band used as indicators of high conductivity.

2.2. HER mechanism on an MXene

The electrocatalytic HER is a cathodic water-decomposition reaction that involves a two-step electron-transfer process [50]. First, H^+ gains an electron and is adsorbed by the catalyst (Volmer step), after which the adsorbed hydrogen (H*) is desorbed from the catalyst surface to form H_2. Because the intrinsic surface chemistry and electronic structures of catalysts are different, the desorption process generally follows two mechanisms (Fig. 3(a)): (1) The combination of two H* to form H_2 (Tafel step); and (2) the reaction of H^+ with H* with the removal of an electron from the catalyst to release hydrogen (Heyrovsky step) [51]. Under neutral and alkaline conditions, water molecules are adsorbed instead of H^+ to form H*, H_2, or OH^- [52]. The Gibbs free energy for hydrogen adsorption (ΔG_H*) is the main parameter used to evaluate the HER activity of an electrocatalyst. A ΔG_H* value closer to zero leads to better HER

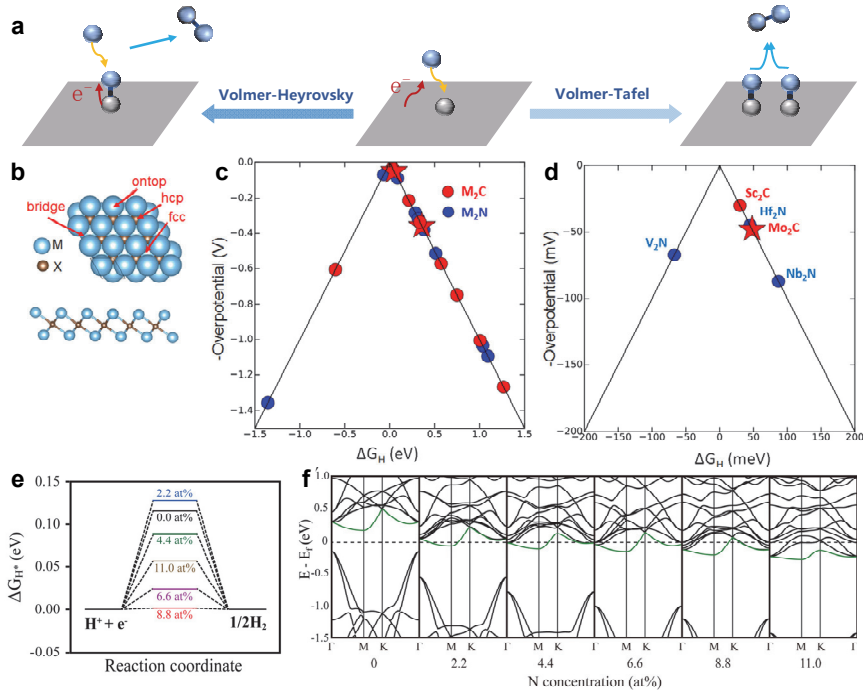

Fig. 3. (a) Schematic diagram of the HER mechanism. (b) Top view of the structure of bare MXene with different adsorption sites. (c) HER volcano plot (d) Enlargement of the top of the volcano. (a–d) Reprinted with permission from Ref. [26]. Copyright 2016, American Chemical Society. (e) ΔG_{H^*} under standard conditions at $U_{SHE} = 0$ V. (f) Band structures at each nitrogen-doping concentration. Each green solid line corresponds to the conduction band. (e,f) Reprinted with permission from Ref. [57]. Copyright 2021, American Chemical Society.

performance; that is, catalysts at the top of the volcano in the volcano diagram are the most active. This assessment also works in alkaline media because the volcano map only moves up and down rather than left to right with increasing pH [53,54]. However, the OH^- in an alkaline electrolyte occupies active sites for hydrogen adsorption and impedes the HER; hence ΔG_{OH^*} impacts the overall HER activity [55]. In addition, the Tafel slope is used to describe the kinetics of the HER, with a smaller Tafel slope indicative of faster kinetics. Tafel slopes of 30, 40, and 120 mV dec^{-1} correspond to Tafel, Heyrovsky, and Volmer rate-determining steps, respectively. The large Tafel slope of the Volmer step is attributable to weak interactions between H^+ and the surface of the catalyst or the high barrier required to break strong covalent O–H bonds in alkaline media. In general, an electrocatalyst exhibits a higher acidic HER current than an alkaline HER current at a given potential [56].

The HER potentials of uniquely anisotropic pristine 2D MXenes have been demonstrated by DFT calculations and experimentally. The combination of T and H*, as the outermost atomic layer, greatly affects HER performance. Surface -O groups rather than –F or –OH groups are active HER sites. The ΔG_H values of most M_2X systems are greater than zero, with the ΔG_H (0.03 eV) of Sc_2C closest to zero (Figs. 3(b)–(d)) [26]. Mo-based and Cr-doped Ti-based MXenes exhibit better performance than Ti-based MXenes. The different electronic states of nitrogen and carbon lead to electronic rearrangement in the X–M–O bond, which affects the electronic states of oxygen. Therefore, transition metals or heteroatoms are implanted into MXenes to alter their electronic states and optimize hydrogen adsorption. Chung *et al.* [57] calculated the effect of replacing C or O in Ti_2CO_2 with N on HER performance. Doping with N was observed to weaken the Ti–O bond, resulting in more of the O-electrons bonding to H, which lowers ΔG_H. The optimal ΔG_H of 0.001 eV was obtained when doped with 8.8% N (Fig. 3(e), (f)). Peng *et al.* [58] synthesized Co-intercalated $Ti_3C_2T_x$:Co by the molten salt method, which showed better alkaline HER performance (η_{10} = 103.6 mV) than $Ti_3C_2T_x$. Even as a carrier, MXene/nanoparticle synergy is superior to that of other two-dimensional materials; the mass activity of the Pt nanoparticles on MXene was found to be 70-times higher than that of 20 wt% Pt/C [59].

2.3. OER/ORR mechanism on MXenes

The OER is the anodic reaction associated with water decomposition, while the ORR is the cathodic reaction of a battery. They are both relatively complex four-electron transfer processes involving OH*, O*, and OOH* intermediates, the mechanisms of which are shown in Figs. 4(a) and (b). Noticeably, despite the OER and ORR passing through the same intermediates, a good OER catalyst does not always catalyze the ORR. The OER follows almost identical reaction pathways in acidic and alkaline media, with the exception that the participants in the reaction are water molecules and hydroxide ions, respectively [60]. Moreover, oxygen is released in two ways: (1) two O* intermediates combine to form O_2 ($2O^* \rightarrow 2^* + O_2$), and (2) OOH* releases O_2 through a proton-coupled electron-transfer process ($OOH^* + OH^- \rightarrow * + O_2 + H_2O$).

The first mechanism associated with the ORR involves a direct four-electron transfer reaction, which can be divided into the following two pathways, depending on the catalyst:

Dissociative:

$$O_2 + 2^* \rightarrow 2O^* \quad (1)$$

$$2O^* + 2H^+ + 2e^- \rightarrow 2OH^* \quad (2)$$

$$2OH^* + 2H^+ + 2e^- \rightarrow 2H_2O + 2^* \quad (3)$$

Associative:

$$O_2 + * \rightarrow O_2^* \quad (4)$$

$$O_2^* + H^+ + e^- \rightarrow OOH^* \quad (5)$$

$$OOH^* + H^+ + e^- \rightarrow O^* + H_2O \quad (6)$$

$$O^* + H^+ + e^- \rightarrow OH^* \quad (7)$$

$$OH^* + H^+ + e^- \rightarrow H_2O + * \quad (8)$$

Bidentate adsorption sites facilitate the release of O=O in the dissociative mechanism, whereas the associative process takes place at terminal adsorption sites [61].

The second mechanism involves a two-step two-electron transfer reaction, in which O_2 gains two electrons to form H_2O_2, after which H_2O_2 gains two electrons to form two H_2O molecules:

$$O_2 + 2H^+ + 2e^- \rightarrow 2H_2O_2 \quad (9)$$

$$H_2O_2 + 2H^+ + 2e^- \rightarrow 2H_2O \quad (10)$$

Owing to the complex nature of the reaction intermediates, "$\Delta G_{H^*} - \Delta G_{OH^*}$" corresponds to the abscissa of the OER volcano diagram. The left leg of the volcano diagram corresponds to strong interactions between oxygen and the catalyst, where the formation of OOH* is the rate-determining step, while the right leg corresponds to weak oxygen/catalyst combinations, where the formation of O* determines the rate of the overall reaction [62,63]. In a similar manner to the HER, ideal OER catalysts are located at the top of the volcano diagram. On the other hand, ΔG_{OH^*} can be used as a separate descriptor on the ORR volcano map. Small overpotentials and low Tafel slopes are indicators of high OER/ORR electrocatalytic activity. Theoretical calculations have shown that each intermediate has a Gibbs free energy of formation of 1.23 V, which is equivalent to a zero free energy for each reaction when a voltage of 1.23 V is applied, with minimal OER/ORR overpotential [61]. However, because the quantitative relationship "$\Delta G_{OOH^*} = \Delta G_{OH^*} + 3.2 \pm 0.2$ eV" exists for the OER/ORR, even an optimal catalyst will have a non-zero overpotential [54]. Adjusting the ΔG values of intermediates or controlling the proportions of various intermediates can enhance catalytic efficiency. Chorkendorff *et al.* [64]

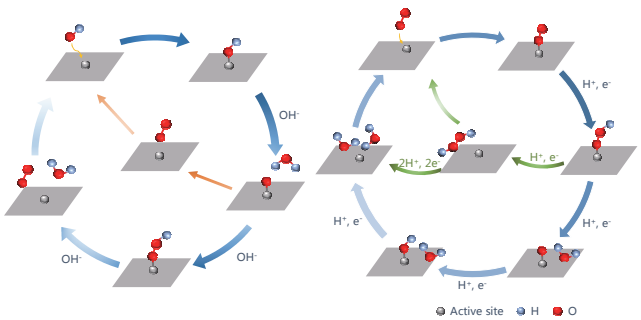

Fig. 4. Schematic diagrams showing the mechanisms associated with the OER (a) and ORR (b).

covered a Pt surface with a Cu monatomic layer, which weakened OH binding to Pt and improved ORR performance eightfold compared to the uncovered catalyst.

While the intrinsic OER/ORR activity of an MXene is almost negligibly small, its high surface energy enables the MXene to combine with the OER/ORR active phase to improve its uniformity and stability. Dispersing OER/ORR-active cobalt species on the surfaces of MXenes has been extensively studied. Peng *et al*. [65] prepared an HER/OER/ORR three-function electrocatalyst by anchoring CoS_2 on an MXene. Zhu *et al*. [66] synthesized Ti_2NT_x@MOF-CoP (average particle size: 466 nm) by wrapping MOF-CoP with Ti_2NT_x sheets. The introduction of Ti_2NT_x prevented CoP aggregation and accelerated electron transport between nanoparticles, thereby greatly reducing the impedance from 284 Ω (MOF-CoP) to 49 Ω. Only 1.61 V was required by Ti_2NT_x@MOF-CoP to totally decompose water under alkaline conditions. In addition, single-atom catalysts based on MXenes, where Pt, Ru, Ni, Fe, and Co are adsorbed on the MXene surfaces at the atomic level, are attractive for the OER and ORR.

3. MXene properties and syntheses

3.1. MXene properties

One M atom is coordinated to six atoms (X and T) in the MXene hexagonal lattice, and T groups are attached to Ti atoms above the hollows of three adjacent X atoms in the proposed stable configuration [67]. The presence of T groups enables MXenes to effectively contact water (contact angle < 35°), which is conducive to water adsorption at active sites during oxidation [68,69]. Owing to the large number of metal layers, the properties of an MXene (from metal to semiconductor) are mainly determined by the *d*-orbital of M, while hybridization between the orbitals of T, X, and M shifts the Fermi energy level, thereby changing the electronic properties of the MXene [70]. MXene-based catalysts transfer charge faster than graphene-based catalysts. However, inevitable vacancy defects, metal oxidation, and sheet aggregation reduce MXene conductivity. In addition, the outermost metal influences conductivity more than the inner metal in an MXene with five or seven atomic layers.

Preparing good MXene-based electrocatalysts can require demanding processes; therefore, exploring MXene stability, including corrosion, heat, and tensile resistance, is vitally important. Generally, dispersed MXene monolayers are less stable than aggregated sheets, whether in water or air. $Ti_3C_2T_x$ begins to form an oxide at 200 °C in oxygen, and is further converted into amorphous carbon and gas (CO_2, CO, CH_4, H_2O) at 1000 °C. However, Ti_3C_2 exists in a metastable state, and a series of MXene derivatives can be synthesized in an argon atmosphere by controlling the heating conditions [71,72]. Stability at high temperatures is greatly influenced by the synthesis method and the structure of the MXene. V_2CT_x, Ti_2CT_x, and Ti_3C_2 show critical structural-collapse temperatures of 375, 400, and 1200 °C, respectively, in an argon atmosphere [73–75]. Sun *et al*. [76] used DFT calculations to study the mechanical properties of Ti-based MXenes subjected to deformation (Fig. 5). The T groups, especially oxygen, cause electrons to move out of the plane along the C–Ti–O unit to prevent the irreversible collapse of the Ti framework when strained through Ti–C bond stretching [77]. The Young's moduli of single-layer $Ti_3C_2T_x$ and $Nb_4C_3T_x$ are 330 and 386 GPa, respectively, which are high for reported solution-processable materials [78,79].

3.2. MXene synthesis

In theory, 12 M atoms can form 72 types of single metal MXene, including carbides and nitrides with three, five, or seven atomic layers, but realizing these experimentally is challenging [22,80]. MXenes are generally prepared using two strategies: top-down and bottom-up. Bottom-up strategies

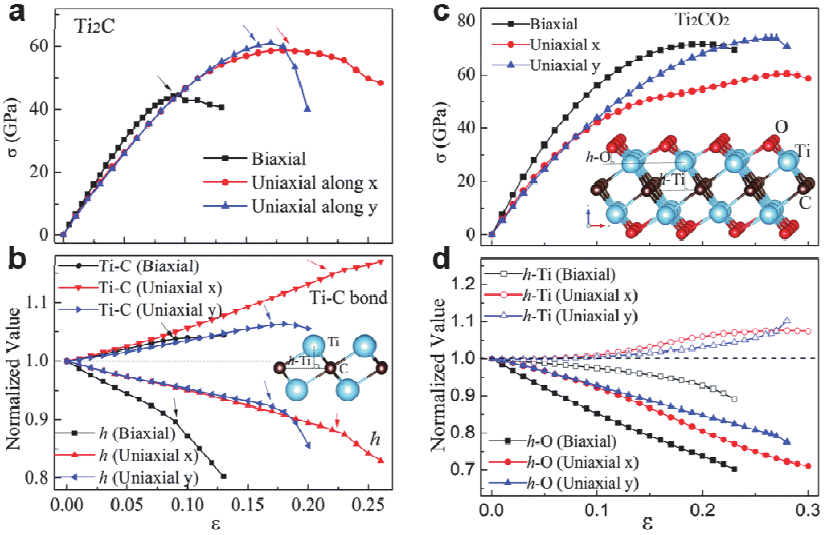

Fig. 5. Calculated stress-strain curves of 2D Ti_2C (a) and 2D Ti_2CO_2 (c). (b) Variations in the bond lengths (Ti–C) and out-of-plane heights of Ti atoms. (d) Variations in the out-of-plane heights of Ti atoms and O atoms. Reprinted with permission from Ref. [76]. Copyright 2016, American Physical Society.

enable thickness to be controlled and form MXenes with few defects. For example, α-Mo_2C has been synthesized by Ren *et al*. through chemical vapor deposition [81], while Sang *et al*. [24] synthesized Ti_4C_3 and Ti_5C_4 by homogeneously growing TiC on a Ti_3C_2 template. On the other hand, the first MXenes were top-down prepared by etching the IIIA, IVA, or VA element (A) from MAX, which contains only one more atomic A layer than the MXene. Top-down etching remains a simple and fast way of synthesizing MXenes, and we mostly concentrate on various etching methods herein.

3.2.1. *High-temperature annealing*

Although some commonly used MAXes have been commercialized, novel MXenes are always derived from laboratory-synthesized MAXes. High-temperature treatment of a mixture of metal M, Al, and graphite powder is the most frequently used method for preparing a MAX in the laboratory [82]. Typically, Ti_3AlC_2 is prepared by uniformly mixing Al, and C powders in a 3:1.5:2 molar ratio, ball milling, and then annealing at 1350 °C [83]. Mo-MAX and a bimetallic Mo and Ti-MAX were also obtained using this method [84]. In a similar manner, Wu *et al*. [85] synthesized Ti_3AlC_2 by placing a 1:1:1.8 molar ratio of TiH_2/Al/TiC in a graphite mold coated with boron nitride. Excess aluminum is required because it is partially lost during annealing. In addition, Ti_3AlC_2 can be prepared by annealing a 1:1 mixture of Ti_2AlC and TiC powders at high temperature under argon [86]. Hot pressing has also been used to synthesize MAX; for example, Barsoum *et al*. [87] prepared Nb_4AlC_3 by *in-situ* hot pressing a Nb, Al, and C powder mixture at 330 MPa and 1700 °C.

3.2.2. *Etching*

Because the M-X bond is more stable than the M–Al bond, the elemental Al in $M_{n+1}AlC_n$ can be removed by the action of fluoride (Fig. 6(a)) [88]. Commonly used fluoride ion etchants include HF and HCl/LiF solutions. The MAX precursor is usually ground into small particles prior to etching to prevent the reaction from only occurring on the surface [89]. In addition, a reasonable combination of etchant concentration and etching time is particularly important. The MXene is not formed when the corresponding MAX is weakly etched; on the other hand, the MXene is further oxidized when too strongly etched. Usually, the etchant concentration is proportional to the number of MAX layers, with the removal of Al in Ti_2AlC and Ti_3AlC_2 requiring 10% and 50% HF, respectively [90]. Moreover, a Ti-based MAX is more easily etched than a Ta-based MAX with the same number of layers because Ta and Al combine more strongly [82]. In addition, Alhabeb *et al*. [91] found that an oxidant is required for HF to effectively remove Si or Ga from a MAX. This method can also be used to synthesize bimetallic MXenes [84]. Recently, bimetallic $Mo_4VC_4T_x$ (with nine atomic layers) was successfully synthesized by treatment with 48%–51% HF [23]. In addition, NH_4HF_2 is a superior etchant because it simultaneously corrodes and strips, and is milder and safer than HF and HCl/LiF, which are advantages [92,93].

A halide-containing electrolyte can convert a MAX into an MXene when activated by voltage, which integrates MXene synthesis with its electrochemical applications. Zhi *et al*. [94] removed Al atoms from V_2AlC in the absence of a strong acid or base using V_2AlC as the cathode and a mixture of 21 M LiTFSI and 1 mol/L $Zn(OTf)_2$ as the electrolyte. V–Al bonds were broken by the attack of F^-; consequently, Al atoms were etched to form V_2C. The etching kinetics of the less-reducing Cl^- was enhanced by the addition of NH_4OH and TMAOH (Fig. 6(b)) [95], with MXene flakes with diameters of up 18.6 nm obtained under these mild conditions. However, a prolonged applied voltage during electro-etching resulted in the oxidation of metal M on the MXene surface.

The first hexagonal Ti_4N_3 was prepared in a molten fluoride salt mixture (KF, LiF, and NaF) [96]. Later, a completely fluoride-free molten salt method was developed for the synthesis of $Ti_3C_2Cl_2$ and Ti_2CCl_2 [97]. The substitution reaction between the MAX and molten $ZnCl_2$ produced the Zn-based MAX; Zn then separated from the MAX and dissolved in $ZnCl_2$ owing to the reducibility of Zn^{2+} in the molten salt (Fig. 6(c)). Nevertheless, V_2C and Ti_2N could not be prepared, even after etching the corresponding precursors (V_2ZnC and Ti_2ZnN). Furthermore, the unique alkali solubility of aluminum metal enables it to be etched by strong alkali [98–100]. Zhang *et al*. [100] successfully synthesized $Ti_3C_2T_x$ (T = OH, O) by treating the MAX with 27.5 mol/L NaOH at high temperature under argon (Fig. 6(d)). High concentrations and high temperatures are required to soluble $Al(OH)^{4-}$ and Na^+ intercalation, while argon inhibited MXene oxidation. Notably, MXene obtained by alkali treatment was 92 wt% pure, with a layer spacing of up to 2 nm. However, thin sheets synthesized by this method were only one-eighth the transverse size of those synthesized by fluoride etching [101].

3.2.3. *Delamination*

Etched MXenes have multilayered accordion-like structures. As was observed during the stripping of other 2D materials, the

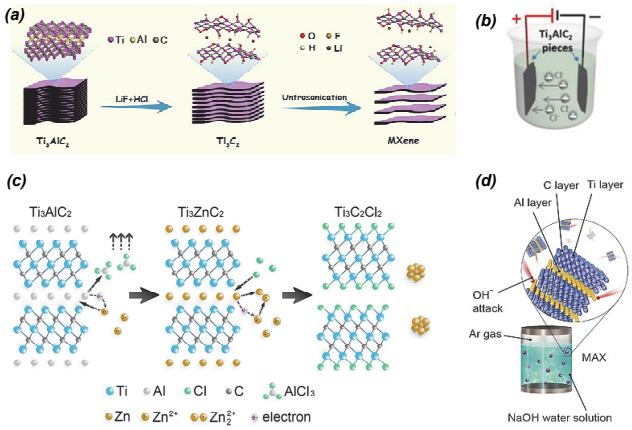

Fig. 6. (a) Schematic diagram showing the formation of an MXene by fluoride etching. Reprinted with permission from Ref. [88]. Copyright 2020, Elsevier. (b) Fluoride-free electro-etching equipment with a dual electrode system. Reprinted with permission from Ref. [95]. Copyright 2018, Wiley-VCH. (c) Schematic diagram showing the mechanism for the synthesis of an MXene in a Lewis-acid molten salt. Reprinted with permission from Ref. [97]. Copyright 2019, American Chemical Society. (d) Schematic diagram of the device used to react Ti_3AlC_2 in an aqueous NaOH solution. Reprinted with permission from Ref. [100]. Copyright 2018, Wiley-VCH.

addition of an intercalator expands the MXene layer spacing. First, the etching agent is removed from the MXene obtained from concentrated HF by washing with deionized water to pH 7. At this time, water molecules insert into the MXene layers to reduce electrostatic interactions. The mixture of MXene and deionized water is then ultrasonicated under an inert gas to produce a dark green suspension of fewer-layer MXene [102]. MXenes were also stripped through water washing and ultrasonication when a concentrated solution of LiF in aqueous HCl was used as the etching agent [103]. Yang *et al*. [104] prepared 0.6-nm-thick Ti_3C_2 flakes using an ultrasonic cell crusher; unfortunately, the 2D structure of the MXene was damaged by long-term ultrasonication [105].

No additional intercalators are required when HCl/LiF is used as the etching agent due to the presence of Li^+. Excess Li^+ diffuses into the MXene layers, resulting in spontaneous peeling and delamination of multilayer $Ti_3C_2T_x$ flakes, even in the absence of additional ultrasonication [106]. K^+, Na^+, and other metal cations are often used to delaminate MXenes. The Ti_3C_2 layer spacing increased from 0.99 to 1.25 nm by oscillating in 6 mol/L KOH for 72 h; however, the flakes were narrower [107]. Wang *et al*. [108] reported that the intercalation of Na^+ into $Ti_3C_2T_x$ by electrolysis in a Na^+-containing electrolyte resulted in the widening of the layer spacing, from 7.7 to 10.1 Å (Fig. 7). NaOH can also shear $Ti_3C_2T_x$ nanosheets into 2.82-nm-wide, 1.81-nm-thick quantum dots during intercalation under similar alkaline conditions.

Organic cations embedded in MXene layers balance terminal negative charges (fluoride, oxide, etc.), which is conducive to increasing the interlayer space. The use of basic organic molecules, such as tetraalkylammonium hydroxide and isopropylamine, as intercalators results in large MXene layer spacings due to their large radii [109]. The (002) XRD peak for TBA-$Ti_3C_2T_x$ (prepared using TBAOH) was observed at 2θ = 5.6°, which is lower than that (2θ = 7.0°) of the K^+-intercalated K-$Ti_3C_2T_x$ [110,111]. Ammonium hydrogen fluoride, which can decompose into HF and NH_4^+, has also been used to prepare few-layer NH_4^+-intercalated MXenes [93,112]. Dimethyl sulfoxide (DMSO)

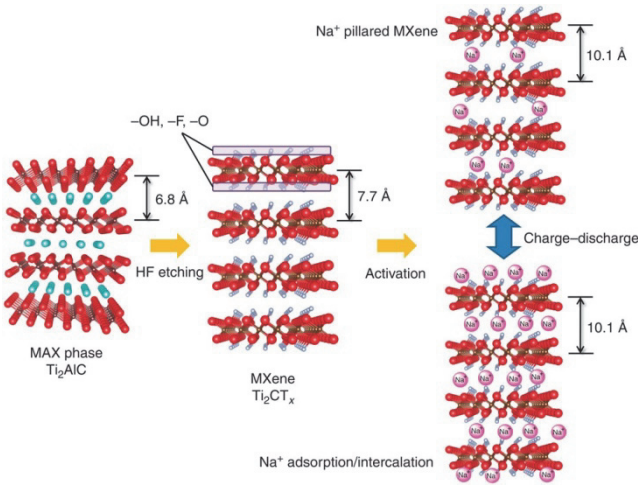

Fig. 7. MXene synthesis and increased interlayer spacing by Na^+ intercalation. Reprinted with permission from Ref. [108]. Copyright 2015, Macmillan Publishers Limited.

has also been used to separate stacked $Ti_3C_2T_x$. Wang *et al*. [113] embedded $Ti_3C_2T_x$ with DMSO and prepared ultrathin (1.85-nm-thick) nanosheets that only contained one-to-two layers of the MXene. Yang *et al*. [114] used ultrasonic stripping under nitrogen to prepare layered Ti_3C_2 in DMSO. In addition, the DMSO increased the MXene layer spacing when assisted by cationic PDDA [115]. The few-layer MXene was separated from the unreacted MAX or multi-layer MXene by centrifugation, after which the MXene powder was vacuum-dried or freeze-dried and stored under oxygen-free conditions to avoid oxidation.

4. MXene characterization

The performance of an electrocatalyst, including its initial potential, Tafel slope, electrochemical active surface area, and conductivity, can be directly measured by simple linear sweep voltammetry, cyclic voltammetry, and AC impedance experiments; however, providing an understanding of its intrinsic active sites and catalysis mechanism, which provide theoretical bases for designing excellent catalysts and improving their performance, requires the use of other characterization methods.

High resolution scanning electrochemical microscopy (SECM) can focus on nanoscale active sites on the surfaces of MXenes and locate the factors responsible any observed increase in electrocatalytic activity. Using a positive SECM feedback pattern diagram, Neale *et al*. found that Fc is reduced slowly on both $Ti_4N_3T_x$ and M-$Ti_4N_3T_x$, indicative of poor MXene conductivity (Figs. 8(a)–(f)) [116]. The acidic HER catalytic activity on the base plane of V-$Ti_4N_3T_x$ is higher than that on the edge according to the SG-TC pattern diagram. Furthermore, the SECM and energy dispersive X-ray spectroscopy (EDS) results showed that both the conductivity and catalytic activity of V-$Ti_4N_3T_x$ improved with increasing V content. On the other hand, the higher applied voltage associated with the OER facilitates catalyst phase transformation. Therefore, observing changes in the electronic structure of the catalyst during the reaction and correctly identifying the active center is particularly important. X-ray photoelectron spectroscopy (XPS) is used to reveal elemental compositions and valence changes; it can be used to analyze elemental oxygen and fluorine on the MXene surface and determine the nature of the bonding between the transition metals and C, N, or O [103]. The 2*p* peaks of metal atoms or alloys show positive shifts in their XPS peaks following the OER, which indicates that valence is related to the catalytic performance of the OER [117]. The valences of the Ni and Co in $NiCoO_x$ bound to an MXene were not significantly different following the OER, as was observed for the hydroxide metal centers (Fig. 8(g)) [118,119]. However, the sulfide, phosphate, and selenide (etc.) metal centers were converted into oxides during the OER. The Co-P and Co-Se peaks of CoP/MXene and Co_7Se_8/MXene were absent after the OER, while a new O 1*s* peak ascribable to Co–O bonds was observed at 529 eV [120]. In addition, the anionic P and Se contents were observed to decrease dramatically during the OER, with PO_x and SeO_x species also generated, as evidenced by peaks at 133.5

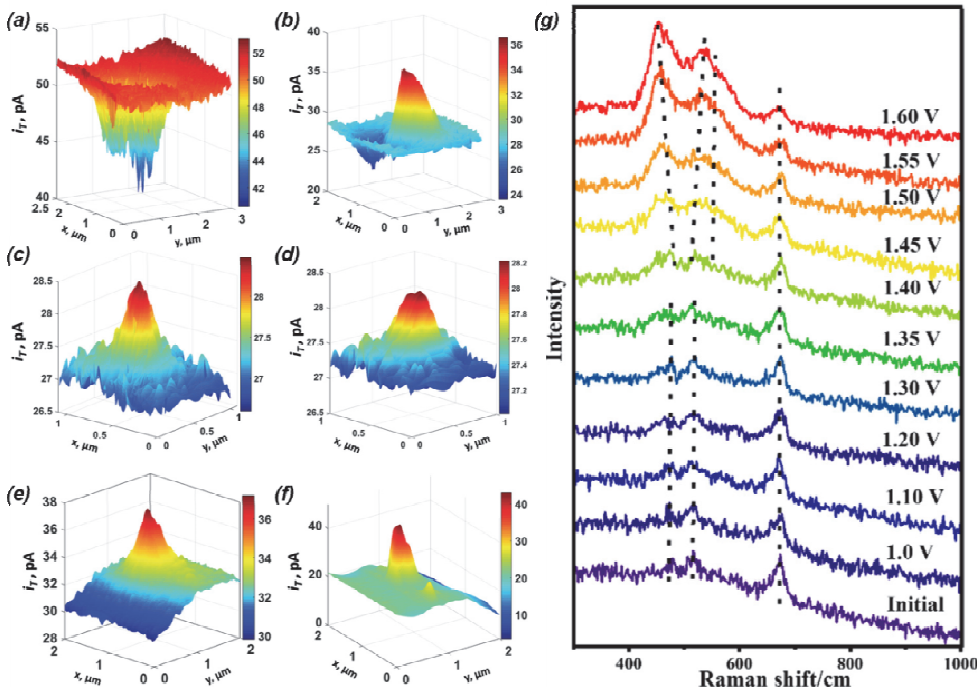

Fig. 8. Feedback mode (a,c,e) and corresponding SG-TC mode (b,d,f) SECM images of three V-$Ti_4N_3T_x$ samples. Reprinted with permission from Ref. [116]. Copyright 2020, WILEY-VCH. (g) *In-situ* Raman spectra of $NiCo_2O_4$/MXene at various applied potentials. Reprinted with permission from Ref. [118]. Copyright 2020, American Chemical Society.

and 60 eV in the P 2*p* and Se 3*d* spectra. Interestingly, the metal oxide and anionic oxide components exhibited opposite behavior, promoting and inhibiting the OER, respectively.

The structures and coordination states of individual atoms in catalysts can be analyzed by X-ray absorption near edge structure (XANES) and extended X-ray absorption fine structure (EXAFS) methods. In particular, XANES and EXAFS are indispensable for studying single-atom catalysts. Average atomic valences can be determined from absorption edge shifts observed in the XANES spectra. The absorption edge of Ru in Ru-SA/$Ti_3C_2T_x$ synthesized by Sun *et al.* [121] was observed to lie between that of Ru foil and RuO_2, which indicates that the Ru in this sample has an oxidation number of between zero and four. In addition, a clear intensity maximum was observed at 4.6 $Å^{-1}$ in the wavelet transform (WT) EXAFS contour plot, which corresponds to a combination of Ru and O; however, no Ru–Ru bond appears to have formed, consistent with Ru atoms dispersed at the atomic level. The EXAFS-fitted bonding model was used in theoretical calculations aimed at further exploring active sites and the reaction mechanism. The dispersed Ru-O_2 sites on Ru-SA/$Ti_3C_2T_x$ were found to promote acidic HER, OER, and ORR activities. Ru-O_2 sites exhibited a smaller $|\Delta G_{O^*}-\Delta G_{OH^*}|$ than single O sites (0.47 vs. 1.95 eV) during the OER, while the highest barrier (0.33 eV) on Ru-SA/$Ti_3C_2T_x$ is associated with the formation of H_2O in the multistep ORR, which is still lower than that for $Ti_3C_2T_x$ (1.32 eV). The ORR exhibited a half-wave potential of 0.80 V in 0.1 mol/L $HClO_4$, and η_{10} values for the OER and HER were determined to be 290 and 70 mV, respectively. Wang *et al.* [122] grew black phosphorus *in situ* on an MXene during heating, and observed the Ti absorption edge to shift to a lower energy in the XANES spectrum, which is attributable to the formation of Ti–O–P bonds in BP-$Ti_3C_2T_x$ (Figs. 9(a) and (b)). Two absorption peaks were observed at 2151.6 and 2153.8 eV in the P K-edge absorption spectrum, consistent with electron transport from P 1*s* to O 2*p*. In addition, the presence of P enlarged the coordination number of Ti (from 3.4 to 5.4) and lengthened the Ti–O bond (from 2.06 to 2.08 Å) (Fig. 9(c)), which reveals that the construction of the BP-$Ti_3C_2T_x$ interface perturbs the electronic environment.

In-situ electrochemical Raman spectroscopy provided a clear reason for the improved electrocatalytic activity; the red-shifted E_g peak, blue-shifted F_{2g} peak, weakened A_{1g} peak, and the new peak at 562 cm^{-1} confirmed the formation of CoO_2 and NiOOH from $NiCo_2O_4$ when the external pressure required by the OER was applied [118]. Oxidation of the MXene surface, which is detrimental to catalytic performance, was also detected by Raman spectroscopy [123]. Moreover, the Raman data show that the addition of the MXene contributes to the formation of an ordered structure. For example, Co-CNT/Ti_3C_2 exhibited a smaller I_D/I_G ratio than Co-CNT, consistent with the presence of highly ordered carbon and higher ORR activity in the former [124].

Other *in situ* characterization techniques are also widely used in the electrocatalysis field. For example, catalytic properties were observed to improve as the MXene (002) XRD peak shifted to lower angles, demonstrating that larger layer spacings favor faster electrocatalysis kinetics [110]. Antonietti *et al.* [125] verified the formation of Fe-N-C by XPS, IR, UV-VIS, and XANES spectroscopies, which was not observed in other blank controls and were determined to be the catalytic sites. In addition, Qiu *et al.* [126] found that water adsorbed on the surface of NiFe-LDH/MXene/NF exhibited weaker O–H bonds than

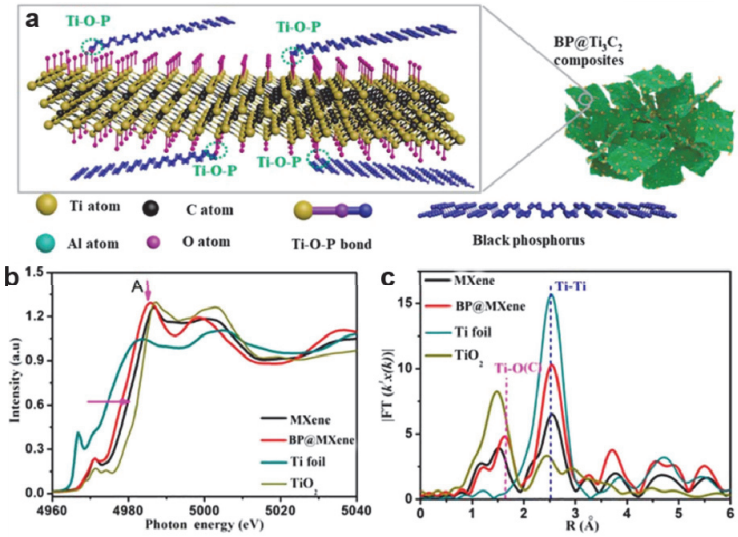

Fig. 9. (a) Structure diagram for BP@MXene; Normalized Ti K-edge XANES spectra (b) and k^3-weighted Fourier-transformed Ti K-edge XANES spectra (c). Reprinted with permission from Ref. [122]. Copyright 2021, American Chemical Society.

those adsorbed on the surface of NiFe-LDH/NF, thereby enabling facile water splitting to produce hydrogen and oxygen, and accelerating the alkaline HER and OER kinetics of NiFe-LDH/MXene/NF.

5. Factors that affect electrocatalysis properties

5.1. Surface functional groups

Owing to its large surface energy, the suspended metallic bonds of an MXene are always connected to H, OH, F, O, or other functional groups to maintain stability, and account for more than 7.54 wt% of the total mass and significantly, which impacts electrocatalysis performance [127]. Different MXenes have different optimal functional-group adsorption sites on their surfaces that are usually located at Fcc and Hcp metal atoms; hence, the active sites are also different.

Studies have shown that MXenes can catalyze the HER. With the exception of Hf_2N, V_2N, and W_2N, whose active sites are metals, the active sites of most MXenes are surface oxygens [26,116]. However, MXenes prepared by fluoride etching inevitably contain F-terminal groups that are not conducive to the HER. Calculations have shown that, instead of adsorbing hydrogen, the F group releases hydrogen by stripping a hydrogen from a nearby hydroxyl group [128]. HER performance declined with increasing number of F terminals (Figs. 10(a) and (b)) and, due to the weakness of the M–F bond, Mo_2CF_x releases HF more easily than H_2 [129]. Fortunately, the oxygen/MXene combination is more stable, despite the higher electronegativity of fluorine (Fig. 10(c)). Hence, F is replaced with oxygen and OH during washing, which improves HER performance. From a thermodynamics perspective, the $|\Delta G_H|$ values of $Ti_3C_2O_2$, Ti_2CO_2, and W_2CO_2 are close to zero at oxygen-coverage rates of 100%, indicative of good HER activity. M_2CO_2, which combines with hydrogen too strongly, also displayed improved HER performance at high hydrogen coverage because the formed hydroxyl groups poorly adsorb hydrogen. For example, Nb_2CO_2, V_2CO_2, $Ti_3C_2O_2$, and $Cr_3C_2O_2$ promote the HER at H-coverage rates of 0–3/8, 4/8–6/8, 1/8–6/8, and 3/8–6/8, respectively [130]. From a thermodynamics perspective, oxygen-rich MXenes are poorly conductive, with Ti_2CO_2 even exhibiting semiconductor behavior. Generally, a certain amount of H or F doping is required to improve electron-transport efficiency [131]. For example, the original Nb_2CO_2 with 1/9 hydrogen coverage is a good catalyst for the HER, with metallic conductivity and a $|\Delta G|$ of 0.036 eV [132].

The ORR and OER pathways involve several intermediates and are more complex than those of the HER. Therefore, appropriate catalyst/intermediate binding strengths are key to improving OER/ORR catalytic performance. Interactions between unterminated MXenes and various intermediates are too strong, and F- and O-functionalized MXenes to bind weakly to

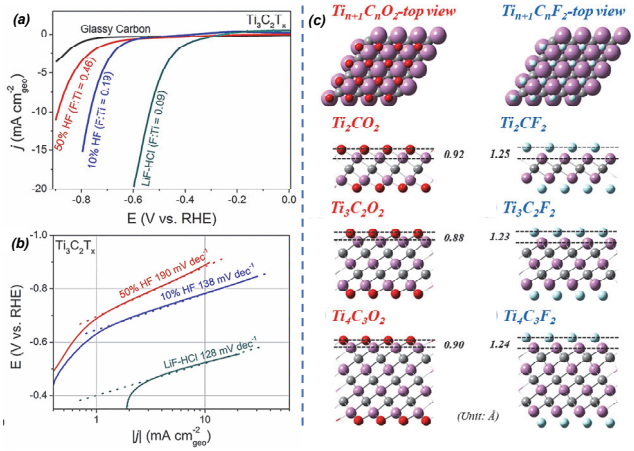

Fig. 10. LSV (a) and Tafel plots (b) of various $Ti_3C_2T_x$ systems. (a,b) Reprinted with permission from Ref. [129]. Copyright 2017, American Chemical Society. (c) Optimized structures of selected MXenes. The distances between the terminators and the first Ti layer are also shown. Reprinted with permission from Ref. [133]. Copyright 2018, American Chemical Society.

such intermediates, both of which are not conducive to the OER/ORR [134]. OH-terminated Nb_2C showed good ORR catalytic potential; however, the H atoms of the –OH moieties were consumed with –OH irreversibly converted into –O. Although the original MXenes are almost OER/ORR inactive, the surface terminals of modified MXenes influence the OER/ORR. Li *et al.* [133] found that a low O/F ratio was beneficial to the ORR when Pt metal was added to the MXene surface. A strong covalent bond was formed between Ti and C at a high F content, with electrons on C more easily transferred to Pt and intermediates through Ti–C bonds, which stimulated the reduction reaction and improved ORR performance.

5.2. Metals and nonmetals in the lattice

In addition to surface functional groups, HER activity is also determined by the metallic and nonmetallic elements in the MXene lattice. The reticular lattices of $M_{n+1}X_n$ 2D materials are very conducive to electron transport, and their high conductivities provide foundations for good electrocatalytic performance, which largely depend on the type of transition metal [135]. $M_{n+1}C_nO_2$ is more conductive when M is a VB or VIB metal rather than a IIIB and IVB metal [130,136]. As the active site for the HER, the oxygen functional group is simultaneously connected to the internal transition metal and externally adsorbed hydrogen; hence, the stability of the O–H bond determines the electron-donating ability of the transition metal. ΔG_H becomes more positive as more electrons are transferred from the metal to the oxygen [136]. MXenes based on Mo and Ti have been most frequently studied as HER catalysts, with the former showing stronger catalytic activity than the latter [26].

In addition to monometallic MXenes, 2D ordered or disordered bimetallic MXenes also show HER catalysis potential. The ΔG_H values of MXenes implanted with various TMs show a periodic pattern related to the electronegativity of the TM [132]. $TiVCO_2$, which was screened by Wang *et al.* [136] using theoretical calculations, exhibited outstanding HER performance, regardless of whether or not the metal atoms are uniformly distributed. Müller *et al.* [137] synthesized a compound based on cobalt-replaced bulk molybdenum carbide (β-Mo_2C:Co), which was referred to as "Mo_2CT_x:Co" (Figs. 11(a)–(c)). About 0.16 mol% of the Mo atoms were replaced by Co atoms; despite the number of active sites not changing in this case, the six oxygen active sites near each cobalt atom were found to have a lower $|\Delta G_H|$ (0.40 *vs.* 0.61 eV). Significantly, Mo_2CT_x:Co exhibited higher HER performance in 1 mol/L H_2SO_4 at current densities greater than 20 mA cm^{-2}, even when the Mo_2CT_x:Co loading was one-tenth that of Mo_2CT_x. By adding metals to $Ti_4N_3T_x$, Neale *et al.* [116] synthesized a series of nitrides (M-$Ti_4N_3T_x$; M = V, Cr, Mo, or Mn) in which M replaced some of the Ti. The addition of V, Cr, and Mo was found to benefit the HER of the original $Ti_4N_3T_x$, while the addition of Mn was found to be detrimental.

Because N has fewer vacant electron orbitals than C, nitrides theoretically adsorb hydrogen more strongly than carbides [138]. Li *et al.* [139] assumed that a transition metal carbonitride monolayer MXene (M_3CNT_x) consisted of separate atomic carbon and nitrogen layers and performed systematic theoretical calculations. With the exception of Ti_3CNO_2 and Nb_3CNO_2, all examined carbonitrides were found to be unsuitable for the electrocatalytic HER (Figs. 11(d)–(f)).

5.3. Vacancy defects

A few perfect MXene crystals have been synthesized. Some of the vacancy defects in the MAX are inherited by the prepared MXene. Moreover, some M and C atoms are exfoliated as the A layer is removed to form atomic vacancies (V_M or V_C) during etching (Figs. 12(a)–(e)). The presence of vacancies alters the electronic structure of the MXene surface, further affecting its

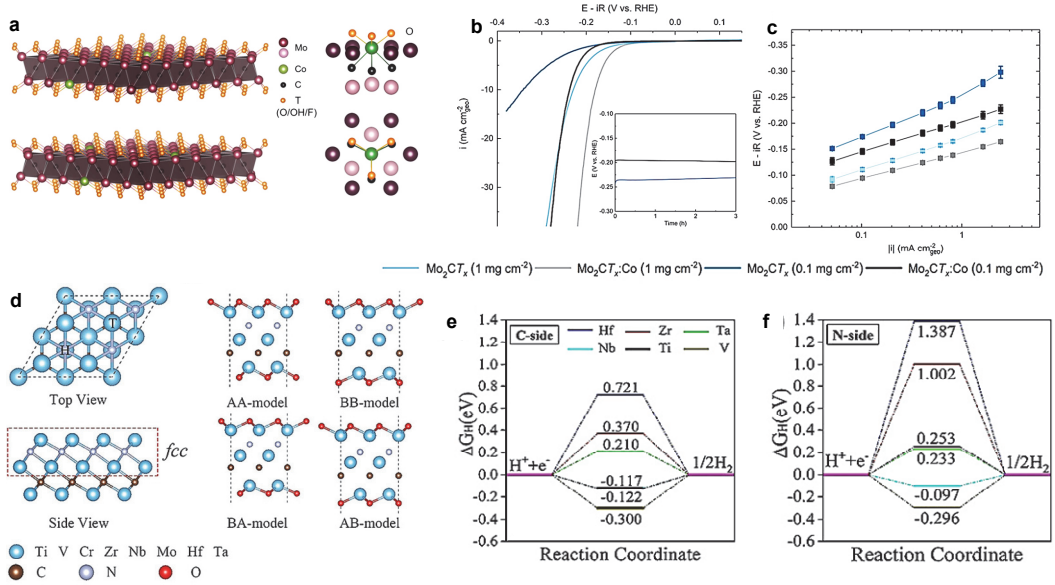

Fig. 11. (a) Model of the Mo_2CT_x:Co structure; LSV curves (b) and Tafel plots (c). (a–c) Reprinted with permission from Ref. [137]. Copyright 2019, American Chemical Society. (d) Top and side views of transition metal carbonitride models; Values of ΔG_H on the C-sides (e) and N-sides (f) of MXenes Reprinted with permission from Ref. [139]. Copyright 2018, Wiley-VCH.

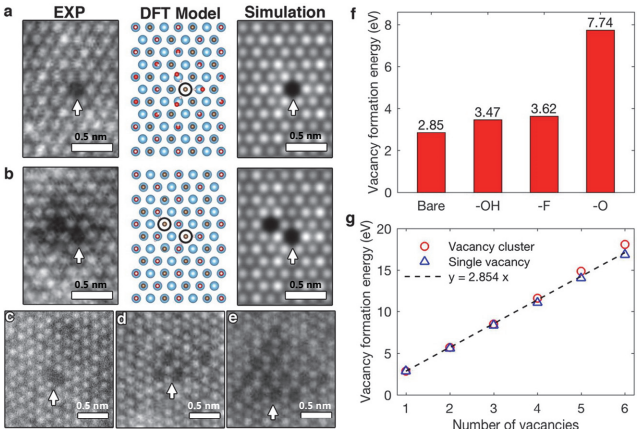

Fig. 12. (a–e) HAADF-STEM images of defects in single-layer $Ti_3C_2T_x$. (f) V_{Ti} formation energies on bare Ti_3C_2 and terminated single-layer $Ti_3C_2T_x$ (g) Formation energy of $V_{Ti}C$ clusters as a function of the V_{Ti} number. Reproduced with permission [140]. Copyright 2016 American Chemical Society.

electrocatalytic performance.

Theoretical calculations showed that vacancy formation is a thermodynamically feasible process, with the formation energies of carbon vacancies in MXenes lower than those of graphene and MoS_2. Functional groups, such as oxygen, on the MXene surface stabilize vacancies (Fig. 12(f)) [140]. Indeed, hydrogen still tends to bind to the oxygen sites on the MXene surface even when defect sites are present. However, bonding between the proton and the metal vacancy becomes metastable when an appropriate cathode voltage is applied, with the initial catalyst potential decreasing with increasing hydrogen coverage on the metal vacancies [141]. Vacancies also cause oxygens to become displaced; oxygens around a metal vacancy that move away from the vacancy carry less negative charge and interact more strongly with hydrogen [142]. In contrast, carbon vacancies weaken oxygen/hydrogen surface interactions. Therefore, poor HER performance caused by excess negative ΔG_H can be adjusted by increasing the number of carbon vacancies, while poor HER performance caused by excess positive ΔG_H can be adjusted by increasing the number of metal vacancies. For instance, the $W_{1.33}C$ synthesized by Rosen *et al.* [141] showed better catalytic performance for the HER under acidic conditions than W_2C.

While vacancies affect electrocatalytic performance thermodynamically, their surrounding are also important. Single vacancy sites generate V^2 sites or larger vacancy clusters under strong etching conditions; these sites/clusters interrupt or block the large and continuous conductive network of an MXene (Fig. 12(g)) [143]. Nucleation sites provided by such vacancies promote MXene oxidation. Ti^{4+} (anatase TiO_2) is always initially formed near a vacancy, with accumulated electrons at the steps and edges of flakes also leading to Ti oxidation [144]. The positive charges at metal vacancies also promote C^{4+} oxidation, with aggregation leading to amorphous carbon. These oxidation products inhibit electron transport and impede the electrocatalysis kinetics of the MXene.

5.4. Dimensions

The dimensions of MXene flakes depend on the raw materials and etching and ultrasonication conditions. Recent studies have shown that the hydrogen-adsorbing abilities and electrical conductivities of MXenes are related to the number of metal layers, which can influence electrocatalytic MXene performance, with ΔG_H even changing sign for a given metal. For example, W_2CO_2 and $W_3C_2O_2$ have ΔG_H values of 0.55 and −0.46 eV, respectively, a difference of about 1 eV [145]. Unfortunately, no clear relationship appears to exist between the number of metal layers and hydrogen-adsorption properties. Vanadium carbide exhibits an adsorption energy that is negatively correlated with thickness, while niobium carbide and tantalum carbide, which also belong to group VB, do not show similar trends. In addition, the ability of an MXene to transfer electrons depends on the number of metal layers, among which Ti-, Zr-, and Hf-based MXenes are the most obvious. The conductivity of monolayer $Ti_3C_2T_x$ was measured to be approximately 6.76×10^5 S m^{-1}, while Ti_2CO_2 exhibited semiconducting properties [140].

At least two MXene flakes are generally prepared experimentally. Layer stacking reduces the specific surface area of the MXene and the number of exposed Ti-O active sites, which is not conducive to hydrogen adsorption. TBA-$Ti_3C_2T_x$, D-$Ti_3C_2T_x$, and K-$Ti_3C_2T_x$ synthesized with different intercalators reportedly have different numbers of layers with different spacing, and exhibit specific surface areas of 46.8, 130, and 10.0 m^2 g^{-1}, respectively (Figs. 13(a) and (b)) [111]. The Tafel slopes of the catalysts supported on K-$Ti_3C_2T_x$ exceed 250 mV dec^{-1}, while those supported on TBA-$Ti_3C_2T_x$ and D-$Ti_3C_2T_x$ are 65 and 70 mV dec^{-1}, respectively. In addition, because catalytically active sites usually exist on basal planes, a small MXene with a damaged basal plane has a larger HER overpotential [129]. Moreover, a 3D configuration can stabilize an MXene, thereby avoiding collapse and ensuring full active-site exposure (Fig. 13(c)). Figs. 13(d)–(f) show that the 3D MXene retains its stereostructure and is evenly re-dispersed in water after being pressed at 150 MPa, while 2D MXene is tightly gathered [146].

6. MXene design principles for electrocatalysis applications

6.1. Improving MXene stability

The large specific surface area of a 2D MXene accelerates its reaction kinetics; however, this is always accompanied by a large surface energy that leads to strong interlayer stacking and aggregation, which is not conducive to exposing the electrocatalytic active sites. Moreover, the resistance of stacked MXene is much higher than that of monolayer MXene, even with good electron transport between layers. Therefore, ensuring that MXene does not stack during the catalytic reaction is an important catalyst-stability prerequisite. Inserting intercalators into MXene interlayers is a good method for supporting nanosheets and weakening van der Waals forces. Intercalators can be organic macromolecules, surfactants, or nanoparticles, among others, that bind and stabilize the MXene [147,148]. Notably, the intercalator needs to be conductive, otherwise,

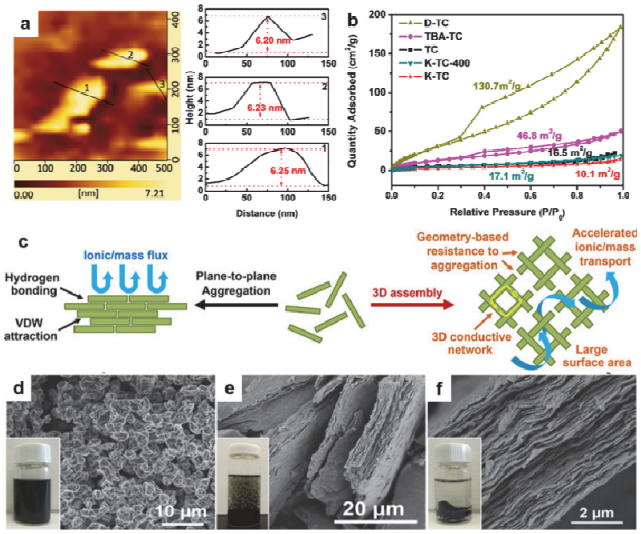

Fig. 13. (a) AFM image of TBA-$Ti_3C_2T_x$. (b) Ar adsorption and desorption isotherms. Reprinted with permission from Ref. [111] Copyright 2019, American Chemical Society. (c) Depicting the merits of a 3D MXene. SEM images of 3D Ti_3C_2 (d), pristine Ti_3C_2 MXene after being compressed (e), and vacuum filtered Ti_3C_2 MXene (f). The insets show images of materials dispersed in water after ultrasonication. Reprinted with permission from Ref. [146]. Copyright 2018, American Chemical Society.

charge transfer is affected.

Furthermore, porous 3D MXene models need to be designed and constructed to balance gravitational and repulsive forces between sheets and avoid MXene aggregation [149]. Wang *et al*. [122] synthesized a 3D folded BP@MXene film, in which black phosphorus forms Ti–O–P bonds to the MXene, which not only enhanced electron transport, but also greatly improved MXene stability. Gogotsi *et al*. [150] synthesized hollow spherical $Ti_3C_2T_x$ using PMMA as the template, which could be uniformly dispersed in an aqueous solution. Qiu *et al*. [146] constructed a 3D MXene framework in which CoP was uniformly dispersed using isotropic capillary forces; However, the 3D framework exhibited poor conductivity owing to the limited contact surface of the sphere. Nevertheless, CoP@3D Ti_3C_2-MXene exhibited alkaline HER/OER performance, and its ECSA was 1.9-times that of the lamellar CoP@Ti_3C_2-MXene analogue. In conclusion, the effect of intercalation and architectural design are exploratory directions for improving MXene stability and avoiding self-stacking.

6.2. *Improving MXene conductivity*

MXene conductivity depends greatly on elemental composition and the number of layers. Theoretical calculations can be used to guide and design structural adjustments by rationally controlling the raw materials. MXene oxidation in the environment or at high voltages, which is fatal for electrical conductivity, is an important factor that needs to be considered. Electron transport and charge exchange mainly involve the non-metallic carbon layer and the complete metal phase inside the MXene [151]. However, aerobic or aqueous oxygen can lead to metal oxidation and the eventual destruction of the MXene structure. The resistance of the MXene film prepared by Ahn *et al*. [152] was 10^5 times higher following oxidation. Koo *et al*. [153] reported that MXene oxidation in aqueous media involves nucleophilic addition (Fig. 14(a)), with metal oxides, amorphous carbon, CO_2, and CH_4 (etc.) formed as products; the reaction mechanism also pH-dependent. Under acidic conditions, H^+ is adsorbed by –OH groups to form Ti–OH_2 moieties in which Ti is clearly electron deficient and more easily attacked by electrons (Fig. 14(b)). On the other hand, Ti–O^- adsorbs cations and water to form solvent cages under alkaline conditions, which separate the oxidizing agent from the Ti to slow down the reaction. Therefore, electrons are clearly localized at metal atoms under acidic conditions, which accelerates the oxidation process. Reducing protonation and avoiding electron localization on the metal can improve MXene oxidation resistance.

6.3. *Increasing intrinsic MXene activity*

Efficient active sites are electrocatalysis cornerstones, and improving active sites can significantly improve electrocatalytic performance. The surface functional groups of an MXene are its reactive sites; therefore, their designs must be first considered. On the one hand, increasing the amounts of specific functional groups is a necessary objective. For instance, oxygen-functionalized MXenes have been synthesized for the HER, while F- or S-functionalized MXenes have been synthesized for the ORR or Li-ion-battery applications [154,155]. On the other hand, improving the bonding and coordination states of the original functional groups is also necessary to achieve a moderate capacity for adsorbing intermediates. The reasonable introduction of doping and vacancies can regulate ΔG, as shown by DFT calculations, and experiments can be designed guided by calculations.

A large specific surface area, which corresponds to high active-site availability, is worth considering during catalyst de-

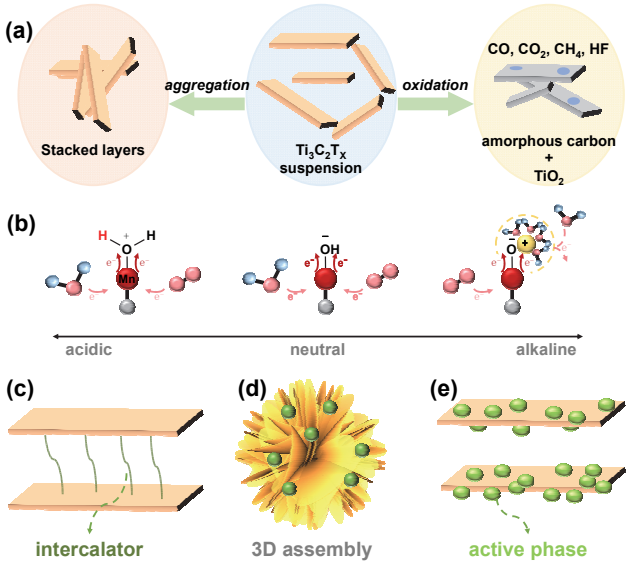

Fig. 14. (a) Degradation of $Ti_3C_2T_x$ in various environments. (b) MXene oxidation mechanisms at various pH values. Three methods for improving the structure and activity of an MXene: (c) layer-spacing expansion; (d) stereo-model assembly; (e) active-phase decoration.

sign. Owing to their strong potential for interfacial coupling and charge transfer, MXenes are mostly used to load catalysts and form heterojunctions, which not only avoids MXene sheet stacking, but also disperses the catalyst and improves its utilization rate. The vertical growth of MoS_2 on an MXene is the most typical example, as it exposes a large number of edge active sites. While the active sites mainly correspond to active phases, the contribution of the MXene cannot be ignored, especially when designing OER and ORR catalysts. Unfortunately, simple mixing cannot achieve the optimal effect, and the main design philosophy involves growing active phases *in situ* without destroying the MXene structure, thereby ensuring simultaneous activity and electrical conductivity. The overall design principle is shown in Figs. 14(c)–(e).

7. Strategies for improving electrocatalysis performance

7.1. Surface modification

The electronic state of an MXene is related to its surface functional groups, which affects its electrocatalytic performance. Seh *et al*. [129] synthesized a series of MXenes with different F-coverage rates and found that the F end groups were detrimental to the HER. Oxygen-functionalized MXenes were prepared by alkalization and annealing after HF etching to afford electrocatalysts with high HER activities. The acidic HER performance (η_{10} = 190 mV) of E-$Ti_3C_2O_x$ synthesized by Su *et al*. [154] was found to be superior to that of E-$Ti_3C_2(OH)_x$ (η_{10} = 217 mV) or E-$Ti_3C_2T_x$-450 (η_{10} = 266 mV). However, the Ti_2CT_x synthesized by Xie *et al*. [131] exhibited a smaller η_{10} for the HER than alkalized Ti_2CT_x, with F contents of 15.12% and 3.43%, respectively. Highly active catalytic sites are provided by O-terminals, while high conductivity is provided by F-terminals, and charge transfer is accelerated by constructing heterojunctions at O-terminals. Zhang *et al*. [221] synthesized fluorine-free I-Na-$Ti_3C_2T_x$ nanosheets in one step using alkali etching; these sheets were 100–300 nm in transverse size and showed high HER activities, with η_{10} values of 139, 299, and 217 mV under acidic, neutral, and alkaline conditions, respectively, after MoS_2 loading.

Substituting P and S atoms for O atoms on the MXene surface can improve HER activity from thermodynamics and kinetics perspectives. Zhang *et al*. [156] chose the $Ti_8C_4O_8$ tetramer of Ti_2CO_2 as a theoretical calculational model and presumed that P doping occurred through replacement of the top oxygen atoms. P-doping was calculated to lead to an O $2p_x$ to O $2p_z$ orbital change, which interacted with H 1s and strengthened the adsorption. The ΔG_H of $Ti_8C_4O_6P_2$ was optimized to 0.05 eV. In addition, the $Ti_8C_4O_8$ bandgap decreased from 0.92 eV to almost 0 eV during the addition of P, which greatly improved charge mobility. Guided by theoretical calculations, Kang *et al*. [157] synthesized P-Mo_2CT_x by calcining red phosphorus and Mo_2CT_x in flowing argon. Notably, the phosphating process not only introduced phosphorus atoms into the entire Mo_2CT_x sample to form Mo–P and P–O bonds, but also increased the number of Mo–O bonds in the nanosheets due to the larger layer spacing, which led to more active sites. P-Mo_2CT_x exhibited a charge-transfer resistance of 175 Ω at an overpotential of 150 mV, which is much smaller than that (810 Ω) of Mo_2CT_x under the same conditions. The combined effect of conductivity and the number of active sites led to a lower η_{10} for the acidic HER.

Single-atom electrocatalysts have been studied because they show high atom-utilization rates and excellent catalytic activities. For example, Guan *et al*. [158] dispersed single-atom manganese on N-doped graphene, in which Mn is coordinated to four nitrogen atoms; this catalyst is highly active toward water oxidation. Bao *et al*. [159] doped Pt atoms into MoS_2 to regulate H* adsorption on S and activate the inert MoS_2 plane for HER catalysis. In a similar manner, MXene-based single-atom catalysts, which are synthesized by doping metal atoms on their surfaces or replacing functional groups with metal atoms, are also HER/OER/ORR candidates. Transition metals that are more electronegative or have more d-electrons can combine with the O atoms on the surface of an MXene to form higher occupied states near the Fermi level and improve conductivity [156,160,161]. Moreover, the TM atoms adsorbed on the surface tend to be located near the middle vacancies of three adjacent oxygen atoms, which forms three kinds of oxygen atom as active sites for the HER [162,163]. The observed optimal HER performance is mainly ascribable to the following two reasons. On the one hand, TM-atom modification leads to a change in the reaction mechanism for H* adsorption (from Heyrovsky to Tafel); on the other hand, electron transfer from TM to O atom reduces the energy barrier for hydrogen desorption [162]. Zhao *et al*. [36] successfully synthesized SA-Cu-MXene by selectively etching Al atoms from $Ti_3(Al_{1-x}Cu_x)C_2$ and leaving Cu atoms on the MXene; the Cu is coordinated to three O atoms with Cu–O bond lengths of about

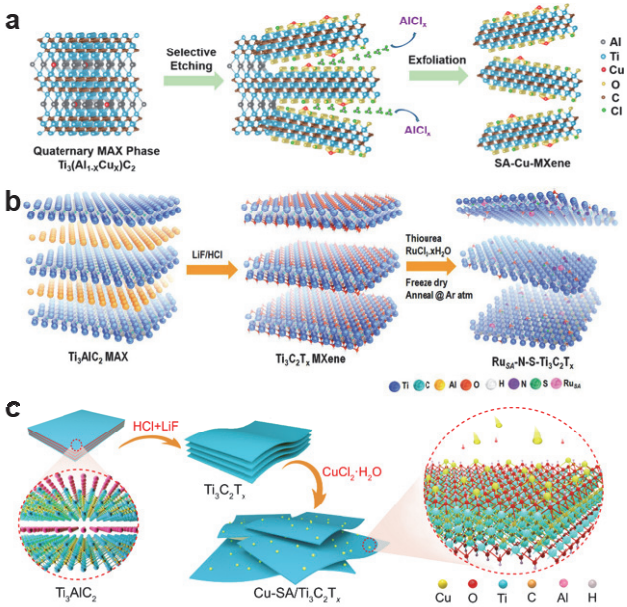

Fig. 15. Syntheses of SA-Cu-MXene (a), Ru_{SA}-N-S-$Ti_3C_2T_x$ (b), and Cu-SA/$Ti_3C_2T_x$ (c). (a) Reprinted with permission from Ref. [36]. Copyright 2021, American Chemical Society. (b) Reprinted with permission from Ref. [165]. Copyright 2019, Wiley-VCH. (c) Reprinted with permission from Ref. [167]. Copyright 2021, Macmillan Publishers Limited.

1.92 Å (Fig. 15(a)). In addition to etching, freeze-drying is a more common method of fixing metal atoms onto ready-made MXenes. Highly active noble metal atoms are preferably selected, with Pt fixed to a hydrophilic MXene by the spontaneous reduction of Pt cations [164]. He and coworkers [165] successfully anchored Ru atoms onto the surface of N- and S-doped $Ti_3C_2T_x$ (Fig. 15(b)). The coordination of isolated Ru to N and S altered the electronic structure of the MXene to deliver a ΔG_H of 0.08 eV. HER activity was significantly higher in an acidic solution, with an η_{10} value of 76 mV reported (down from 453 mV). Ru_{SA}-N-$Ti_3C_2T_x$ prepared by Zhang *et al*. [166] exhibited an even lower ΔG_H value of 0.039 eV and showed excellent catalytic HER activity at all pH values, with η_{10} values of only 27, 23, and 81 mV in 1 mol/L KOH, 0.5 mol/L H_2SO_4, and 1 mol/L PBS, respectively. Nevertheless, transition metal atom doping does not always promote the HER. For example, $|\Delta G_H|$ was still greater than 0.2 eV, irrespective of the TM added to Hf_2CO_2, Zr_2NO_2, Hf_2NO_2, and Y_2NO_2. Cu-based single-atom Cu-SA/$Ti_3C_2T_x$, with a Cu valence state of between zero and one, was synthesized by Sun *et al*. [167] using the freeze-drying method (Fig. 15(c)). Cu-SA/$Ti_3C_2T_x$ exhibited a ΔG_H (–0.35 eV) even further from zero than that of Cu-NP/$Ti_3C_2T_x$ (0.18 eV), indicative of inferior HER performance; however, it was able to catalyze the reduction of CO to multi-carbon products.

Furthermore, the metal-oxygen sites on the surface of an MXene provide favorable processes for catalyzing the OER/ORR. Cu-Ti_2NO_2 (0.24 eV) and Ni/Cr_2CO_2 (0.16 eV) exhibited low theoretical overpotentials for the OER, which is attributable to enhanced electronic states near the Fermi level [135,168]. Zhang *et al*. [169] explored the OER/ORR performance of double-atom catalysts (DAC) consisting of Fe/Co/Ni atoms and a Ti_2CO_2 substrate through DFT calculations. A total of 48 adsorption models were simulated using six diatomic models and eight adsorption modes (Figs. 16(a) and (b)). The minimum Gibbs free energy profiles (Figs. 16(c) and (d)) show descending left-to-right steps for the ORR and right-to-left steps for the OER; hence, Ni1/Ni2- and Fe1/Ni2-DACS were predicted to show good bifunctional OER/ORR activities. Using high-temperature annealing and cation exchange, Wang *et al*. [170] synthesized Co SAs/Mo_2C, in which Co is adsorbed at vacancies between three adjacent Mo atoms. The catalyst showed enhanced OH* adsorption because d electrons were transferred from Mo to Co along the Co–Mo_3 bond. Compared with other Co monatomic catalysts, Co SAs/Mo_2C exhibited better OER performance, including a higher turnover frequency and superior methanol resistance. The Co–N bond was found to increase the oxidation state of Co when the substrate was NC, and its ability to bind OH* was so weak that it was extremely susceptible to methanol.

7.2. Lattice substitution

Theoretical calculations have shown that the electrocatalytic properties of an MXene depend on the elements in the hexagonal lattice, including M and X. Lattice substitution involves replacing the original atoms in the MXene lattice by injecting

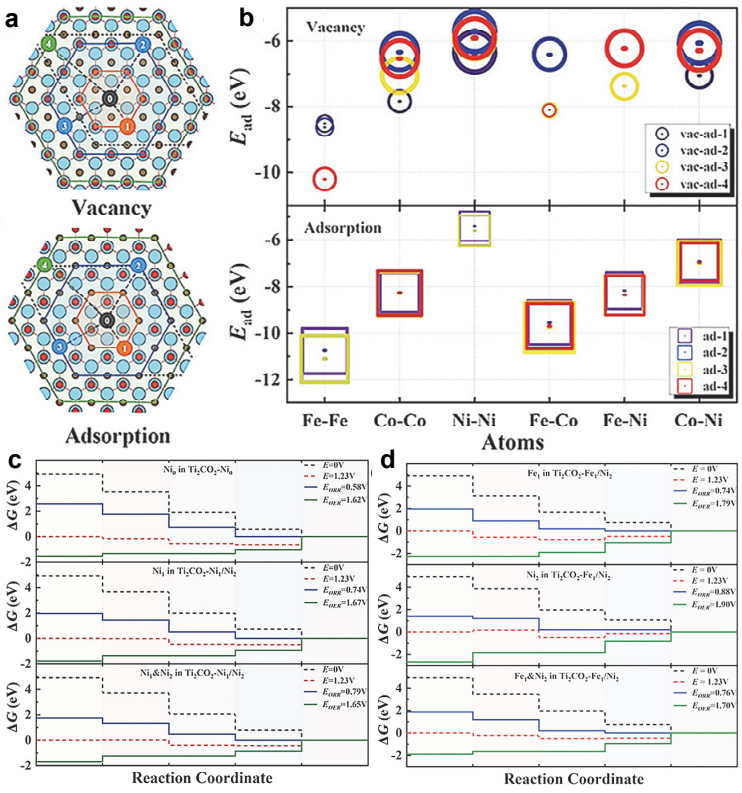

Fig. 16. (a) Four different oxygen vacancy sites and four different neighboring adsorption sites for the 4 × 4 supercell structure. (b) Theoretical calculational results for six pairs of metal atoms adsorbed onto the eight DAC sites in (a). (c,d) Calculated Gibbs free energy differences (ΔG) for the elementary reaction steps along OER and ORR pathways. Reprinted with permission from Ref. [169]. Copyright 2021, Wiley-VCH GmbH.

other metal or nonmetal atoms, and is regarded to be a trouble-free strategy for preparing MXenes containing various elements. Such modification preserves the hexagonal packing structure of the MXene but disturbs the electronic structure, thereby altering interactions between the original active sites and reaction intermediates. Notably, lattice substitution is mainly used to improve the intrinsic HER activity of an MXene. Indeed, improving OER/ORR activities, which MXenes are not endowed with, is difficult.

7.2.1. *Metal atom substitution*

Compared with common Ti-, Mo-, V-, Cr-, and Nb-based MXenes, those based on middle and late transition metals are more favorable for electrocatalysis but are difficult to synthesize [80]. Theoretical calculations revealed that implanting transition metal atoms into M_2XO_2 changes ΔG_{H^*}, reduces the HER barrier, avoids MXene aggregation, and improves HER activity [162,171]. Consequently, developing optimal catalysts by doping metals into MXenes has become a considerable focus.

Gold, silver, and platinum-group elements were the first metal dopants. Wang *et al*. [172] synthesized $Mo_2TiC_2T_x$-Pt_{SA} by immobilizing Pt atoms in the Mo vacancies of $Mo_2TiC_2T_x$ double-transition-metal MXene nanosheets. The modified MXene exhibited extremely high HER activity in 0.5 mol/L H_2SO_4 owing to the dispersed Pt atoms and strong Pt–C bonds, with low overpotentials of 30 and 77 mV at 10 and 100 mA cm^{-2}, respectively, a low Tafel slope (30 mV dec^{-1}), and high stability (100 h) observed. Nevertheless, Zhou *et al*. [132] found that Pt and Pd were unable to improve the conductivities of MXenes with semiconductor properties; therefore, they only activated MXenes with metallic properties. The addition of almost all precious metals was found to improve the HER activity of M_2CO_2, with $|\Delta G_H| < 0.1$ eV at O sites; however, doping Pt, Os, or Au into M_2NO_2 led to inferior activities [162].

Substitution with an inexpensive transition metal can also effectively promote the HER. An isolated Nb can enter the $Ti_3C_2O_2$ lattice by substituting for Ti and residing in the same coordination environment as the Ti. The two types of oxygen atom near the introduced Nb have ΔG_{H^*} values of −0.14 and −0.23 eV, which are different to that of the original lattice (−0.25 eV) and alleviate strong hydrogen adsorption [173]. A small amount of Co substitution in a Mo-based MXene also led to similar properties and outstanding HER performance [137]. However, theoretical calculations revealed that excess Fe, Co, and Ni doped into Mo_2CO_2 at levels of 6.25, 8.33, and 12.5 mol%, respectively, led to ΔG_{H^*} values that were further from zero to varying degrees, which is detrimental to the HER [163]. Ni doping into bimetallic MXenes led to various changes in hydrogen adsorption behavior. Miao *et al*. [174] synthesized D-Mo_2TiC_2/Ni by replacing Mo atoms with Ni through electrochemical stripping and *in-situ* reduction, with the Ni-doped system showing a lower overpotential than D-Mo_2TiC_2.

In addition to single/double-metal substitution, alloying is regarded to be another method for improving the HER performance of an MXene [84,175–178]. Geometrical and electronic synergy resulting from differences in the radii and electronegativities of the various metal atoms in an MXene affects its electrocatalytic performance (Fig. 17) [176]. Guided by DFT calculations, Su *et al*. [177] selected a series of undeveloped 2D MXene ordered binary alloys (OBAs) with outstanding HER activities that even exceed those of Pt. As for OBA synthesis, Gogotsi *et al*. found that the type of metal and annealing temperature influences the OBA structure. Alloys are more stable with Mo in their outer layers, while Ti atoms can occupy the entire outer layer of an MXene devoid of Mo atoms. However, $Mo_2TiC_2T_x$, with only Mo present in two surface layers, did not show potential for HER catalysis because of its semiconductor properties [84]. Therefore, the syntheses of 2D ordered bimetallic alloy MXenes that exhibit good catalytic HER performance need to be further explored.

7.2.2. *Substituting nonmetal atoms*

Carbonitride-based MXenes are more catalytically active than the corresponding carbides. Replacing entire atomic layers of C with N hardly boosts the HER performance of an MXene. Therefore, $Ti_3(C,N)_2O_2$, which is stable owing to the strong Ti–N bond formed by substituting a single carbon atom, has been studied more extensively [179]. The C atoms in $Ti_3C_2T_x$ are replaced with N atoms to form N–Ti–O bonds when annealed in an ammonia atmosphere (Fig. 18(a)) [180]. However, the N 1*s* XPS spectrum exhibits a peak at 396.4 eV only at temperatures higher than 600 °C, indicative of the presence of nitrogen in the lattice site. Consequently, N-$Ti_3C_2T_x$@600 exhibited a lower η_{10} of 198 mV compared to N-$Ti_3C_2T_x$@200 (560 eV) and N-$Ti_3C_2T_x$@400 (410 eV) that are not lattice substituted. Meanwhile, N-$Ti_3C_2T_x$@600 exhibited the lowest resistance and the largest ECSA, which is ascribable to lattice destruction through nitrogen substitution. The solvothermal method can also be used to introduce N into the MXene lattice to form Ti–N bonds, which are the predominant active sites. The carbides can be doped with nitrogen atoms by ultrasonication in ammonia in the presence of $NaBH_4$, which promotes the elimination of oxygen functional groups and provides NH_3 with the opportunity to attack defect sites [181]. The ratio–N

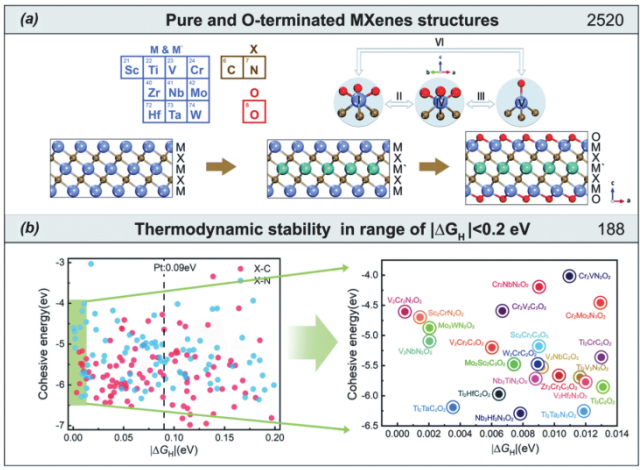

Fig. 17. DFT calculational system. (a) Structure of an OBA and possible oxygen adsorption sites. (b) Promising OBA HER catalysts. Reprinted with permission from Ref. [176]. Copyright The Royal Society of Chemistry 2020.

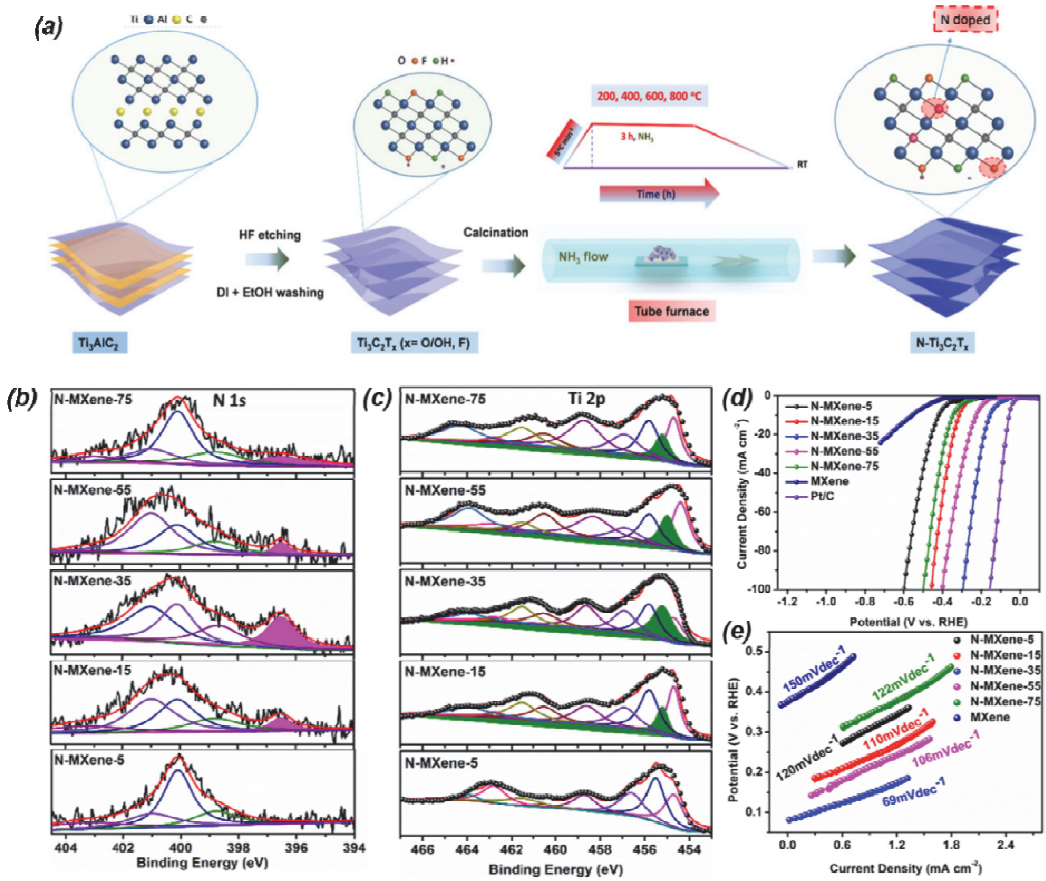

Fig. 18. (a) Synthesis of a N-doped MXene. Reprinted with permission from Ref. [180]. Copyright 2019, American Chemical Society. (b,c) Deconvoluted XPS spectra of N-MXene-T; LSV traces (d) and Tafel slopes (e) of N-MXene-T. Reprinted with permission from Ref. [182]. Copyright 2020, Elsevier.

bond ratio was observed to first increase and then decrease with as the reaction temperature was increased from 5 to 75 °C (Figs. 18(b) and (c)) [182]. N-MXene-35, which contains the largest number of Ti–N bonds, presented appreciably improved HER activity, with a low overpotential and small Tafel slope (Figs. 18(d) and (e)).

Lattice carbon atoms were not dominantly substituted during nitrogen doping due to the large activation energy; rather functional group substitution and surface adsorption occurred. Therefore, the MA(CN) precursor can be *in-situ* etched to give MXenes with specific lattice C/N replacements. Considering the positive effect of nitrogen doping on the electrocatalytic performance of an MXene, other heteroatoms, such as sulfur and boron, which have similar properties to nitrogen, have also been introduced into MXenes to improve their catalytic activities. Using DFT, Li *et al.* [28] calculated that B-doped Ti_2CO_2 has a ΔG_H of −0.097 eV, which is close to that (−0.09 eV) of Pt. X-Ti_2CO_2 (X = P, S) also has a small free energy ($|\Delta G_H| < 0.2$); however, the ΔG_H values of the X-Mo_2CO_2 (X = N, B, P, S) Mo-based MXenes were calculated to be further from zero than that of Mo_2CO_2. In addition, Berber *et al.* [183] found that B and B + N doping did not significantly affect the semiconductor properties of Sc_2CF_2, whose bandgap was calculated to be in the 0.55–0.24 eV range.

A new type of MBene containing less-electronegative nonmetallic atomic B layers was theoretically recently predicted to exhibit excellent HER activity. Firstly, most 2D MBenes are metallic, although Hf- and Zr-based MBenes may be semi-metallic [184]. Fe_2B_2, Cr_4B_6, and Mn_2B_2 have theoretical ΔG_{H^*} values that are very close to zero [185–187]. Nonetheless, MBene is less stable than the corresponding MXene. Ni_2ZnB and Ni_3ZnB_2 were successfully synthesized by Fokwa *et al.* [188]; however, because conventional etching methods cannot eliminate Zn, further studies aimed at preparing MBenes with high HER activities are needed.

Because of they are less electronegative than nitrogen and sulfur atoms, phosphorus atoms are deemed to exhibit better potential for effectively enhancing HER performance. An *et al.* [189] successfully doped phosphorus atoms into V_2CT_x by heating triphenylphosphine with V_2CT_x at 500 °C, which increased the layer spacing from 0.79 to 1.03 nm while maintaining the original hexagonal structure. Instead of forming P–O or P–V bonds during doping, the P atoms were more inclined to form thermally stable C–P bonds that have high electron-donating capacities and balance the energy barriers for H^+ reduction and H_{ad} desorption. As a result, the HER activity of P-doped V_2CT_x in 0.5 mol/L H_2SO_4 is noticeably better than that of pristine V_2CT_x, with an η_{10} of −163 mV and a Tafel slope of 74 mV dec^{-1}.

Few studies have examined how doping MXenes with nonmetallic atoms affect OER and ORR performance. Que *et al.* [190] successfully prepared N-doped few-layered Ti_3C_2 by

subjecting a solid solution of $Ti_3C_{1.8}N_{0.2}$ and $Ti_3C_{1.6}N_{0.4}$ to *in-situ* acid etching. The nitrogen atoms in the $Ti_3C_{2-x}N_x$ nanosheets synthesized by this process mainly exist in the following four forms: N-Ti (nitride), N-5 (pyrrolic), N-Q (quaternary), and N-6 (pyridine nitrogen), with the electron-donating effect of N-6 the main reason for the observed enhancement in OER activity. In addition, the improved surface wettability and electrical conductivity led to an increase in active-site utilization and promoted the OER. $Ti_3C_{1.6}N_{0.4}$ nanosheets required overpotentials of 245.8 and 450 mV in 1 mol/L KOH to yield current densities of 1.0 and 10 mA cm^{-2}, respectively, with a Tafel slope of 216.4 mV dec^{-1}.

7.3. Defect engineering

Defect engineering has been widely used to modify MXenes. Designing vacancies that improve the electrocatalytic performance of an MXene is challenging but necessary. Acid etching during MXene formation is the simplest method for introducing metal or C/N vacancies. Defects size and density on an MXene can be effectively regulated by controlling the concentration of the etching solution, etching time, and temperature [143]; however this method is not very accurate because it is incapable of creating specific defects and over-etching is common. Differences in the strengths of atomic interactions can be used to control defects formed by acid etching. Rosen *et al*. [191] etched two metals, namely Al and Sc, from the $(Nb_{2/3}Sc_{1/3})_2AlC$ quaternary MAX solid solution to precisely form $Nb_{1.33}CT_x$ with metal vacancies (Figs. 19(a)–(c)). Zhang *et al*. [192] first routinely removed Ti atoms from Ti_3CNT_x with HF to expose carbon and nitrogen atoms. Owing to electronegativity differences, the carbon atoms near the nitrogen were etched to form pyridine-N, pyridine-N-O, and pyrrole-N (Figs. 19(d)–(i)). Each of the three types of nitrogen contains a lone pair of electrons, which facilitates active-intermediate adsorption and promotes the OER/ORR.

Doping metal atoms into MXene vacancies is a valuable method for improving electrocatalytic performance; d electrons become redistributed between the doped M and its surroundings, which changes the electronic state of the MXene in a manner that is advantageous for the HER. The acidic HER activity of $Mo_2TiC_2T_x$-Pt_{SA} is much higher than that of $Mo_2TiC_2T_x$-V_{Mo}, and both exhibited better activity than $Mo_2TiC_2T_x$ [172]. DFT calculations revealed that Fe doping into the Ti vacancy of Ti_3N_2 potentially led to catalytic HER activity with an optimized ΔG_H value [193]. In addition, Wang *et al*. [194] examined how embedding TM atoms in the V_3O_3 vacancy of V_2CO_2 influences HER performance. TM atoms bonded to three O atoms promoted charge transfer; hence the surface O atoms gained electrons from the V atoms, which weakened the O–H bonds. The ΔG_H of Ni-V_2CO_2 (25% coverage) was determined to be −0.01 eV, with oxygen atoms that are not bonded to TMs acting as HER active sites (Figs. 19(j) and (k)).

Theoretical calculations showed that filling T vacancies (T = O, OH, F) with specific metal atoms is beneficial for the OER/ORR, as it moderates the oxygen- and water-adsorption strengths of the MXene. Decorating T vacancies with Pt and Pd altered the surface *d*-band center of Nb_2CT_2, which led to low theoretical η_{OER} and η_{ORR} values that are indicative of high ORR and OER activities [134,195,196]. Furthermore, the effects of Pt decoration on the OER/ORR properties of nonmetal carbide MXenes, ordered bimetal carbide MXenes, nitride MXene (Ti_4N_3), and carbonitride MXene have been investigated computationally [138], which showed that the electronegativity of the metal and the vacant orbital of the terminator are related to the performance of the recombinant MXene catalyst. Among them, Nb_2CF_2-V_F-Pt, $Nb_4C_3F_2$-V_F-Pt, and $Cr_2TiC_2F_2$-V_F-Pt exhibited the best catalytic ORR/OER activities. However, the high barriers for hydrogenation and oxygen dissociation inhibited the ORR when Pt atoms were doped into Nb vacancies [134].

As another vacancy engineering protocol, electrocatalytically active substances with vacancies can be *in-situ* generated or loaded onto MXene substrates. Long *et al*. [197] synthesized oxygen-vacancy-rich TiO_2 nanoparticles *in situ* on the surface of

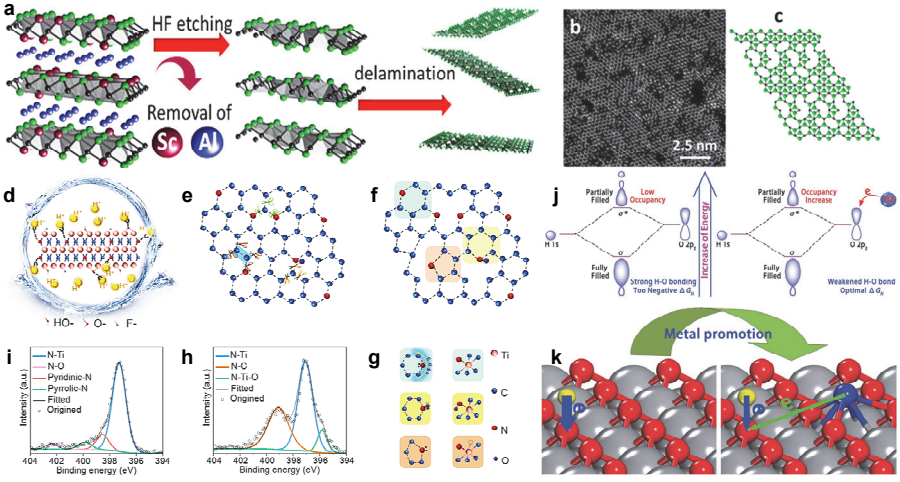

Fig. 19. (a) Synthesis of $Nb_{1.33}CT_x$; HRTEM image (b) and the top-view schematic (c) of $Nb_{1.33}CT_x$. Reprinted with permission from Ref. [191]. Copyright 2018, American Chemical Society. (d–f) Formation of defects in Ti_3CNT_x. (g) Three types of N active site; N 1*s* XPS spectra of Ti_3AlCN (h) and Ti_3CNT_x (i). Reprinted with permission from Ref. [192]. Copyright 2021, Elsevier. (j,k) Modulating the HER performance of V_2CO_2 by introducing a transition metal onto the surface. Reprinted with permission from Ref. [194]. Copyright 2016, WILEY-VCH.

an MXene using the ethanol solvothermal method, with the product displaying excellent OER/ORR performance. In addition, they also loaded V_O-SnO_2 onto an MXene surface [198]. The oxygen vacancies in the oxide altered the electronic structures of Ti and Sn, which acted as OER/ORR sites to accelerate charge transfer. With the aim of improving the electronic properties of MXenes, V_O-Nb_2O_5/Nb_2C [199], V_S-CdS/Ti_3C_2 [200], and o-P-$CoTe_2$/MXene [201] were also synthesized using calcination and solvothermal methods (Figs. 20(a)–(c)). Hao *et al.* [202] appropriately doped P atoms into TiO_2/$Ti_3C_2T_x$ to form V_O-TiO_2, which showed excellent alkaline HER performance (η_{10} = 97 mV) under light and applied voltage. In a similar manner, Tian *et al.* [203] *in-situ* supported TiO_2 and MoS_2 on Ti_3C_2, and then reduced Mo^{4+} using a hydrothermal reaction to create V_{Mo} while preparing Mo_xS@TiO_2@Ti_3C_2 (Fig. 20(d)). The discontinuous lattice fringes observed for MoS_2 verified that V_{Mo} had formed, leading to faster charge separation and more-efficient carrier transfer. The double Ti_3C_2/MoS_2 cocatalyst greatly boosted the Mo-vacancy utilization efficiency.

7.4. Controlling the morphology

2D MXenes tend to stack during electrode preparation, which hinders the exposure of electrocatalytic active sites [204]; consequently, MXene morphologies have been regulated to improve active-site utilization. Owing to the quantum confinement effect, MXene nanodots derived from nanosheets contain high proportions of active sites and surface defects and are expected to have great applications potential in the electrocatalysis field [45]. MXene nanoparticles approximately 50 nm in size were prepared by ultrasonicating flakes, and smaller MXene quantum dots were obtained by directly treating MAX powder with acid [105,205]. $Ti_3C_2T_x$ quantum dots prepared from Ti_3AlC_2 powder exhibited a high degree of oxidation and were almost carbon QDs without Ti-related nanoparticles. Layered MXene nanosheets were directly transformed into nanodots in a one-step hydrothermal process in the presence of aqueous ammonia [206]. MX@C nanodot hybrids with core-shell structures composed of MXD nanodots and carbon shells, exhibited good HER kinetics under alkaline conditions, with a Tafel slope of 32 mV dec^{-1}. The MXene itself did not show catalytic ORR behavior; however, the addition of MXene nanostructures to the ORR electrocatalyst increased its conductivity and improved reaction selectivity. Loading MXene nanoparticles on carbon nitride, which retains its original structure, led to a flow of electrons from the former to the latter. The electron-less state and inherent hydrophilicity of an MXene promote the adsorption and reduction of oxygen [105].

Cutting an MXene into one-dimensional fibers can increase its specific surface area and improve electrocatalytic performance. Hydroxide ions can be used as a "pair of scissors" to cut MAX into 50-nm-wide fibers, after which metal-ion etching proceeds as usual to produce MXene fibers (Figs. 21(a)–(c)) [207]. Ti atoms and even carbon atoms are easily oxidized by hydroxide, which is not advantageous for the HER; however, the Ti_3C_2 NFs exhibited a specific surface area more than seven times that of the corresponding flakes, which resulted in a low η_{10} of 169 mV and a Tafel slope of 97 mV/dec in 0.5 mol/L sulfuric acid. The morphological structure of the fiber was unaffected at hydroxide concentrations below 8 mol/L. However, 0.5 mol/L NaOH is capable of cutting MXene into small (10-nm-diameter) highly functionalized particles when the aluminum in MAX is initially removed with HF, which inhibits the HER [45].

Despite the main body retaining its 2D sheet structure, changes in the MXene stacking structure can greatly affect electrocatalytic performance. The conventionally prepared MoS_2/MXene transformed into a special nanoroll structure that

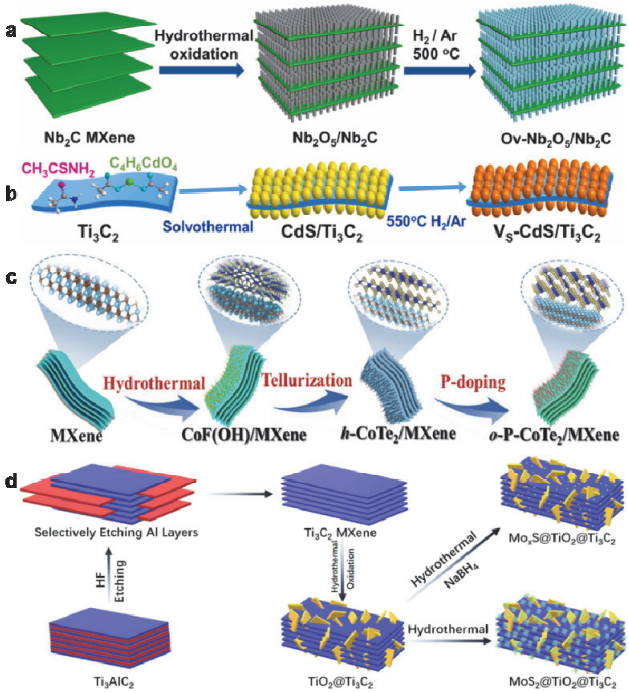

Fig. 20. Syntheses of V_O-Nb_2O_5/Nb_2C (a), V_S-CdS/Ti_3C_2 (b), o-P-$CoTe_2$/MXene (c), and Mo_xS@TiO_2@Ti_3C_2 (d). (a) Reprinted with permission from Ref. [199]. Copyright 2020, Elsevier. (b) Reprinted with permission from Ref. [200]. Copyright 2021, Elsevier. (c) Reprinted with permission from Ref. [201]. Copyright 2021, Wiley-VCH. (d) Reprinted with permission from Ref. [203]. Copyright 2019, Elsevier.

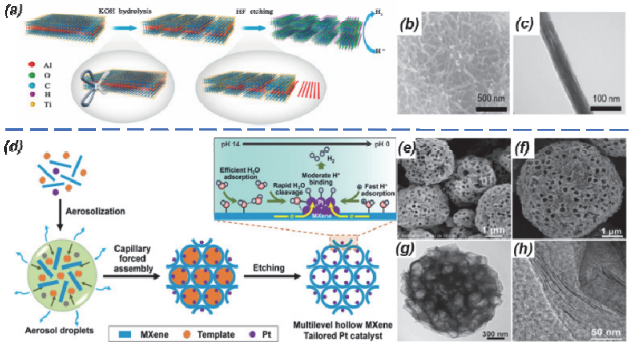

Fig. 21. (a) Synthesis of Ti_3C_2 NFs; High-magnification SEM (b) and TEM (c) images of Ti_3C_2 NFs. Reprinted with permission from Ref. [207]. Copyright 2018, American Chemical Society. (d) Synthesis of a multilevel hollow MXene tailored low-Pt catalyst; SEM images (e,f), TEM image (g) and HRTEM image (h) of the mh-3D MXene with a honeycomb surface. Reprinted with permission from Ref. [209]. Copyright 2020, Wiley-VCH.

had an onset HER overpotential of only 30 mV after two steps involving cooling in liquid nitrogen followed by annealing [208]. Using a template-engaged ultrafast aerosol drying strategy, MXene nanosheets assembled randomly around the template to form a 3D MXene structure (mh-3D MXene) with sufficient diffusion channels, multiple reaction surface areas, high conductivity, hydrophilicity, and anti-aggregation properties (Figs. 21(d)–(h)) [209]. The catalytic HER performance of the 2.4% Pt@mh-3D MXene was superior to that of 20% Pt/C over the entire pH range, which is attributable to the fact that anchoring ultrafine metal nanoparticles on the mh-3D MXene surface effectively improves metal-atom utilization. Moreover, flower-shaped $W_2C@WS_2$ 200–400 nm in size was synthesized using WCl_6 powder, thioacetamide, and ethanol as raw materials and a simple hydrothermal method; it also did not use a MAX precursor [210]. The nanoflowers were basically 10 nm thick and 50–150 nm wide, while W_2C and WS_2 both exist as neat hexagonal structures. While the conductivity and HER onset potential of the nanoflowers are similar to those of the nanosheets, as they are only stacked differently, the Tafel slope of the former is smaller than that of the latter owing to the larger active areas on the depleted surfaces of the nanoflowers. Owing to its continuous conductive network and unique interfacial properties, 3D hollow structures prepared by controlled synthesis promote full MXene utilization during electrocatalysis [209]. The HER/OER performance of MXenes modified using different strategies is summarized in Table 1.

7.5. Constructing heterojunctions

The catalytic activities of MXenes remain limited and are prone to inactivation, despite doping with metal/nonmetal atoms regulating the electronic structures of MXenes and their binding strengths to reaction intermediates. In particular, dissolved oxygen in an aqueous solution combines with the most active edge of an MXene to generate TiO_2, resulting in catalyst degradation [214]. Therefore, 2D MXenes are used as conductive carriers for other species that are catalytically active toward the HER/OER/ORR, which reduces the degree of MXene oxidation and improves performance. Transition-metal-based

Table 1
MXenes modified using different strategies for use in the HER/OER.

Modification strategy	Catalyst	Electrolyte	Application	η_{10} (mV)	Tafel slope (mV dec^{-1})	Ref.
Surface modification	Mo_2CT_x	0.5 mol/L H_2SO_4	HER	189	75	[129]
	E-$Ti_3C_2O_x$	0.5 mol/L H_2SO_4	HER	190	60.7	
	E-$Ti_3C_2(OH)_x$	0.5 mol/L H_2SO_4	HER	217	88.5	[154]
	E-$Ti_3C_2T_x$-450	0.5 mol/L H_2SO_4	HER	266	109.8	
	Ti_2CT_x nanosheets	0.5 mol/L H_2SO_4	HER	170	100	[131]
	I-Na-$Ti_3C_2T_x/MoS_2$	0.5 mol/L H_2SO_4	HER	139	78	[211]
	P-Mo_2CT_x	0.5 mol/L H_2SO_4	HER	186	—	[157]
	$Ti_3C_2T_x$:Co-12h	1 mol/L KOH	HER	103.6	104.42	[58]
		0.1 mol/L $HClO_4$	HER	70	27.7	
	Ru-SA/$Ti_3C_2T_x$	0.1 mol/L $HClO_4$	OER	290	37.9	[121]
		0.1 mol/L $HClO_4$	ORR	0.82	60.4	
Lattice substitution	$Mo_2TiC_2T_x$	0.5 mol/L H_2SO_4	HER	248	74	[129]
	$Mo_2Ti_2C_3T_x$	0.5 mol/L H_2SO_4	HER	275	99	
	Ru_{SA}-N-$Ti_3C_2T_x$	0.5 mol/L H_2SO_4	HER	23	42	[166]
		1 mol/L KOH	HER	28	29	
	Ru_{SA}-N-S-$Ti_3C_2T_x$	0.5 mol/L H_2SO_4	HER	76	90	[165]
	Mo_2CT_x:Co	1 mol/L H_2SO_4	HER	180	59	[137]
	$Ni_{0.9}Co_{0.1}$@ NTM	1 mol/L KOH	HER	43.4	116	[173]
	N-$Ti_3C_2T_x$@600	0.5 mol/L H_2SO_4	HER	198	92	[180]
	N-MXene-35	0.5 mol/L H_2SO_4	HER	162	69	[182]
	P_3-V_2CT_x	0.5 mol/L H_2SO_4	HER	163	74	[189]
	$Ti_3C_{1.6}N_{0.4}$	1 mol/L KOH	OER	—	216.4	[190]
Defect engineering	$Ti_3C_2T_x$-N_6	1 mol/L KOH	HER	119.17	61.81	[27]
			OER	360	76.68	
	D-Mo_2TiC_2/Ni	0.1 mol/L H_2SO_4	HER	780	56.7	[174]
	$Mo_2TiC_2O_2$-V_{Mo}	0.5 mol/L H_2SO_4	HER	—	44	[172]
	$Mo_2TiC_2O_2$-Pt_{SA}	0.5 mol/L H_2SO_4	HER	30	30	
Morphology control	CoP@3D Ti_3C_2-MXene	1 mol/L KOH	HER	168	58	[146]
	3D MX (35%)/NG	0.5 mol/L H_2SO_4	OER	298	51	[212]
	$Nb_4C_3T_x$-180	1 mol/L KOH	HER	398	122.2	[213]
	Ti_3C_2 NFs	0.5 mol/L H_2SO_4	HER	169	97	[207]
	$MoS_2/Ti_3C_2T_x$	0.5 mol/L H_2SO_4	HER	152	70	[208]
	$W_2C@WS_2$ nanoflowers	0.5 mol/L H_2SO_4	HER	320	55.4	[210]
	Pt@mh-3D MXene	1 mol/L KOH	HER	27	42	[209]

compounds are good electrocatalysts and have been extensively studied. Among them, carbides, nitrides, phosphides, and sulfides can catalyze the HER, while oxides and hydroxides tend to promote the OER [215–217]. Unexpectedly, these compounds can become bifunctional electrocatalysts when the MXene is used as the substrate. The heterojunction formed between the non-metallic material and the MXene was also found to exhibit good electrocatalytic activity.

A heterojunction is the electron- and hole-transport interface formed between the MXene and the other material. A Schottky junction, which is commonly found in a photocatalyst, is a type of heterojunction formed between a metal and a semiconductors. An MXene-based heterojunction is generally formed by self-assembly and *in-situ* synthesis. The main self-assembly driving force involves electrostatic interactions between the negative functional groups on the MXene and the positive charges of the main catalyst. Wang *et al*. [218] prepared $Ni_xB/N_{10}TC$ by proportionally mixing N-doped Ti_3C_2 and Ni_xB; electron transfer from $N_{10}TC$ to Ni_xB, as evidenced by XPS, verified heterojunction formation. In addition, a mixture of gC_3N_4 and $Ti_3C_2T_x$ was annealed at 200 °C to form $gC_3N_4/Ti_3C_2T_x$, which was connected only through physical bonding [219]. Nevertheless, the composite showed superior photocatalytic HER properties despite only being physically bonded. Unlike the simple mixing of two or more materials, where the structures of the MXene or the other materials do not change significantly, the *in-situ* synthesis method is used to generate another material directly on the MXene; the heterojunction formed by this method is more stable and generally cannot be separated. Fu *et al*. [220] successfully synthesized an HER/OER catalyst (Co-CoO/Ti_3C_2-MXene) in a mixture of MXene, $CoCl_2$, and $NaBH_4$. Here, $CoCl_2$ is simultaneously reduced to Co-CoO by $NaBH_4$, and Co (with HER performance) and CoO (with OER performance) are *in-situ* loaded on the MXene. Co-CoO/Ti_3C_2-MXene only needed 1.55 V to realize overall water decomposition in an alkaline system. Deposition involves exposing MXene to precursors that react and become attached to the MXene to form MXene-based composites, which is an *in-situ* growth method. Tang *et al*. [221] deposited nickel and iron ions on $N_{10}TC$/NF to form LDHs using electrochemical deposition and *in-situ* growth. The OER performance of NiFe-LDH/$N_{10}TC$ was enhanced by a factor of 8.8 compared to that of NiFe-LDH alone. The heterojunction synthesized through *in-situ* growth was covalently bonded through strong electron coupling and can remain active for more than 50 h during reaction.

An active phase can easily be introduced into an MXene through the construction of a heterojunction, and an MXene-based hybrid contains catalytically active sites from the active phase while retaining the high conductivity of the MXene. In addition, the extra material neutralizes the negative charge on the surface of the MXene, thereby avoiding aggregation. Importantly, the structure of the MXene clearly needs to be protected during compound synthesis to avoid a reduction in catalytic activity associated with its sensitivity to oxidation. In addition, the structure of the compound also affects performance (Fig. 22). A short electron-transfer pathway is conducive

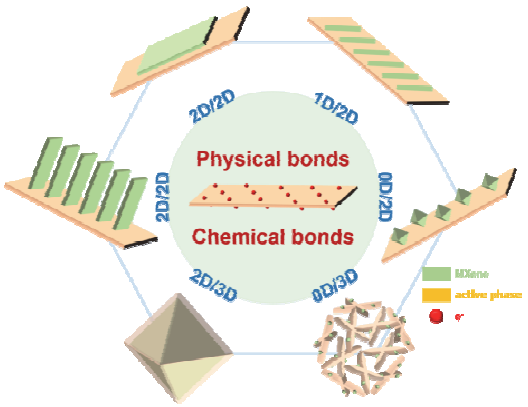

Fig. 22. Different MXene-based heterojunction structures.

to high conductivity in a 0D/2D structure; however, uniformly dispersing 0D materials without the substrate wasting sites is challenging. An array arrangement is beneficial for exposing the active sites in a 2D/2D structure; however, the small contact area limits electron transport.

7.5.1. Metal-MXene heterojunctions

The carbon carriers in Pt/C or Ag/C electrodes are susceptible to corrosion while reacting and MXenes are potential carriers owing to their high conductivities and stable structures [83]. Strong interactions between Pt and the –F, –OH, or –O groups on the surface of an MXene accelerates the Volmer step, resulting in excellent HER performance [110,111]. Fang *et al*. [103] synthesized coral-like Pt nanoparticles approximately 20 nm in size on the surface of an MXene, which slightly improved its catalytic HER performance. Gao *et al*. [110] synthesized Pt-TBA-$Ti_3C_2T_x$ by atomic layer deposition (ALD), in which the Pt clusters were approximately 2 nm in size. How well the Pt nanoparticles are dispersed is related to the number of deposition cycles. The catalyst exhibited the largest ECSA and the best HER performance when 40 deposition cycles were used. Sun *et al*. [111] deposited Pt onto few-layer (less-than-five-layer) MXene using wet-impregnation and a photo-induced reduction method. TBA-$Ti_3C_2T_x$-Pt-20 and D-$Ti_3C_2T_x$-Pt-20 showed η_{10} values of 55 and 70 mV in 0.5 mol/L H_2SO_4, respectively, owing to the fast electron-transfer kinetics of thin-layer MXene [222]. In addition, a binder-free HER electrocatalyst was prepared by immobilizing Pt nanoparticles on porous $Ti_3C_2T_x/Ti_3AlC_2$ using spontaneous redox chemistry; the catalyst exhibited a low η_{10} of 43 mV as its active sites were not blocked by binders [89]. An MXene doped with Ag nanoparticles also exhibited HER activity [223], while Pt [224] and Ag [225] nanostructures supported on MXene afforded many oxygen adsorption sites and a shortened diffusion pathway for adsorbed oxygen, and demonstrated good ORR performance. MXene/NF synergy, where the carrier was NF rather than MXene, also endowed the MXene with high electrocatalytic activity [226]. In addition, as a self-supporting electrode, NF avoids the adverse effects of insulating adhesives, such as sodium phenanthrene, on electrocatalysis [226,227].

Reactive metal-support interactions (RMSIs) can be used to

prepare a metal with an oxide carrier in a bimetallic alloy [228,229]. The presence of precious metal NPs promotes the removal of surface functional groups and the reduction of the M component of an MXene; hence, the M in the MXene can form intermetallic compounds (IMCs) with precious metal NPs through RMSIs [228,230]. Lin *et al*. [85] synthesized cubic Pt_3Ti octahedral nanoparticles (Fig. 23(a)) on the surface of an MXene by *in-situ* reduction. The Pt_3Ti (111) and Pt_3Ti (100) surfaces exhibited ΔG_H* values of −0.01 and −0.05 eV, respectively, which are closer to zero than those of Pt (Fig. 23(b)). Appropriate hydrogen adsorption and fast charge transfer endowed the catalyst with a low overpotential (32.7 mV@10 mA cm^{-2}) and a small Tafel slope (32.3 mV dec^{-1}) (Figs. 23(c)–(h)).

7.5.2. Chalcogenide-MXene heterojunctions

As a typical transition metal dichalcogenide, the 2H(triangular prism coordination)-MoS_2 semiconductor is highly stable toward the HER and can combine with MXenes to form heterostructures that show high catalytic performance [231]. DFT calculations revealed that the vanishing p-type Schottky barriers at the contact interfaces between the MXene and 2H-MoS_2 improved substrate conductivity and the hydrogen-adsorption capacity of 2H-MoS_2, which is the reason for the observed improvement in HER activity [232,233]. The unsaturated Mo-S bond at the edge of MoS_2 is the HER active site, whose ΔG_H is approximately equal to zero [234]. However, MXenes are easily oxidized under hydrothermal conditions [235]. To preserve the structure and properties of an MXene, Qiu *et al*. [236] used carbon nanospheres to prevent oxygen from entering the lattice, thereby effectively maintaining the stability of the MXene; the MoS_2/Ti_3C_2-MXene@C hybrid exhibited an initial HER potential of only 20 mV (Figs. 24(a)–(f)). Furthermore, MoS_2 can be directly generated by annealing the Mo-based MXene at high temperatures in the presence of sulfur [237,238]. Seh *et al*. [238] synthesized $Mo_2CT_x/2H\text{-}MoS_2$ by *in-situ* vulcanization, which effectively inhibited MXene surface oxidation. The epitaxial $Mo_2CT_x/2H\text{-}MoS_2$ lattice interface ensures exceptional HER durability for more than ten days. Studies have shown that MoS_2 exhibits faster charge-transfer kinetics and better HER performance when the interlayer spacing is larger [208,239]. MoS_2/Ti_3C_2, with a MoS_2 layer spacing of 0.94 nm (which is significantly larger than the interlayer distance of the volume crystal (0.64 nm)), was prepared through microwave synthesis and exhibited a low Tafel slope of 40 mV dec^{-1} [239]. Doping with heteroatoms alters the electronic structure of MoS_2 and promotes water-decomposition kinetics under alkaline conditions [240,241]. Fan *et al*. [234] synthesized $Co\text{-}MoS_2/Mo_2CT_x$, which demonstrated superior HER activity (η_{10} = 112 mV) and good stability under alkaline conditions. 1T (octahedral coordination)-phase MoS_2 is more conductive than the corresponding 2H-phase, but is less stable toward the HER [239,242,243]. Therefore, Tao *et al*. [115] stabilized 1T'(twisted octahedral coordination)-phase MoS_2 on a cationically modified MXene surface, on which the properties of 1T'-MoS_2 could be

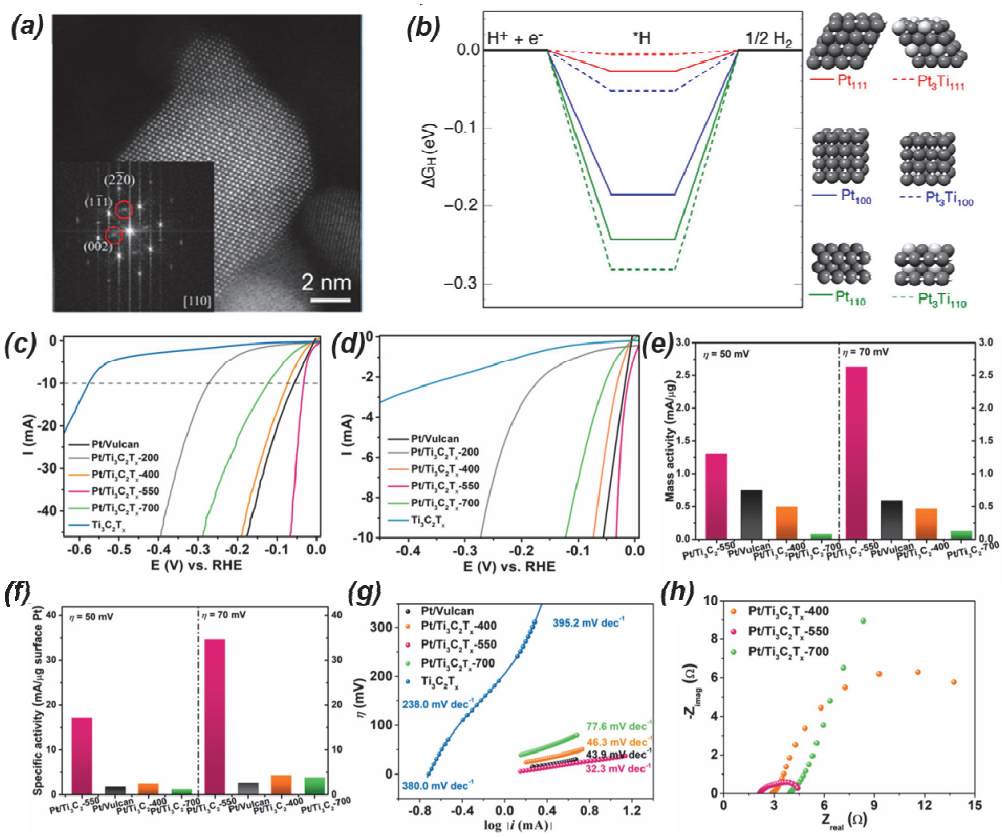

Fig. 23. (a) HAADF-STEM image of used $Pt/Ti_3C_2T_x$-550. (b) DFT calculations. (c) HER polarization curves and (d) a magnification of the 0–10 mA region. (e) Mass activity and (f) specific activity of catalysts. (g) Tafel curves. (h) Nyquist plots of $Pt/Ti_3C_2T_x$. Reprinted with permission from Ref. [85]. Copyright 2019, American Chemical Society.

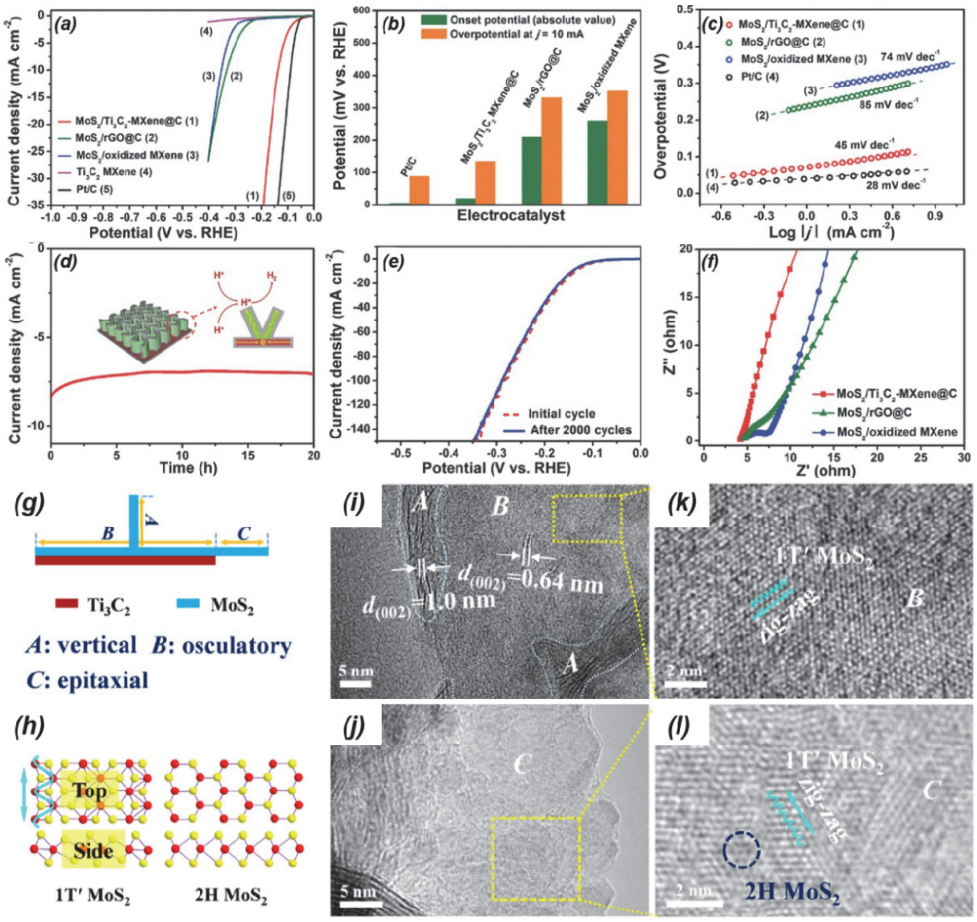

Fig. 24. (a) Polarization curves. (b) A comparison of the catalysts in onset potential and overpotential at j = 10 mA cm^{-2}. (c) Tafel plots. (d) time-dependent current density curves at η = 130 mV for MoS_2/Ti_3C_2-MXene@C catalyst. (e) Polarization curves after continuous potential sweeps of 2000 cycles. (f) EIS spectra at η = 100 mV. Reprinted with permission from Ref. [236]. Copyright 2017, Wiley-VCH. (g) Schematic diagram of the MoS_2-Ti_3C_2 compound. (h) Single-layer polymorph mode of MoS_2. (i,k) HRTEM images of the top profile of MoS_2-Ti_3C_2. (j,l) HRTEM images of epitaxial MoS_2 flakes in MoS_2-Ti_3C_2. Reprinted with permission from Ref. [115]. Copyright 2021, Elsevier.

maintained for long times at low temperatures (Fig. 24(g)-(l)). The hybrid was stable for up to 20 h in the acidic HER process. The 2D/2D interfacial coupling between amorphous MoS_x and MXene is also beneficial for the HER [244].

Other forms of metallic sulfide have been shown to exhibit unexpected catalytic activities [114]. Jaroniec *et al*. [245] compounded NiS_2 nanoparticles onto a V-based MXene by *in-situ* CVD to form a sandwich-shaped heterostructure. Strong electron coupling between NiS_2 and MXene inhibited lamellar stacking and promoted electron transfer, which resulted in the heterostructure exhibiting good HER activity under alkaline conditions. A hydrothermal method was used to prepare the $NiSe_2/Ti_3C_2T_x$ hybrid, which was formed by coating octahedral $NiSe_2$ nanocrystals with ultrathin MXene nanosheets; the hybrid promoted synergistic electrocatalytic water splitting [246].

MoS_2 and other disulfides are not suitable OER electrocatalysts; however, they effectively promote oxygen evolution when heterojunctions with MXenes are formed [245,247]. Tao *et al*. [248] prepared a bifunctional 1T/2H $MoSe_2$/MXene HER/OER electrocatalyst with coexisting 1T and 2H phases. A current density of 10 mA cm^{-2} was achieved at 1.64 V and was maintained for 50 h when used as an alkaline water decomposition electrode. In addition, 1T/2H $MoSe_2$/MXene showed good HER activity (η_{10} = 273 mV) in phosphate buffer.

7.5.3. *Phosphide-MXene heterojunctions*

Metal phosphorus trisulfides (MPS_3), such as TMDs, are materials in which metal layers are enwrapped by both S and P [249,250]. Yan *et al*. [250] used the self-assembly method to synthesize NFPS@MXene nanohybrids by decorating the MXene surface with $Ni_{1-x}Fe_xPS_3$ (Fig. 25(a)); the activity of the catalyst was found to be related to the Ni:Fe ratio. $Ni_{0.7}Fe_{0.3}PS_3$@MXene showed OER activity (η_{10} = 282 mV), while $Ni_{0.9}Fe_{0.1}PS_3$@MXene showed HER activity (η_{10} = 196 mV). High bifunctional HER/OER activities can be achieved using composite materials comprising metal phosphides/selenides and MXenes [251,252]. The CoP/MXene and Co_7Se_8/MXene hybrid systems prepared by Yoo *et al*. [120] demonstrated efficient HER/OER kinetics. In particular, CoP/MXene showed a low potential (1.56 mV@10 mA cm^{-2}) for basic overall water splitting. Due to their poor thermodynamic stabilities, metal sulfides, phosphides, and selenides are converted *in situ* into amorphous metal oxides/oxyhydroxides during the OER process (Figs. 25(b)–(d)) [253–255]. Therefore, the former are considered to be catalyst precursors, while the latter are the real active OER catalysts [255–257]. In addition to

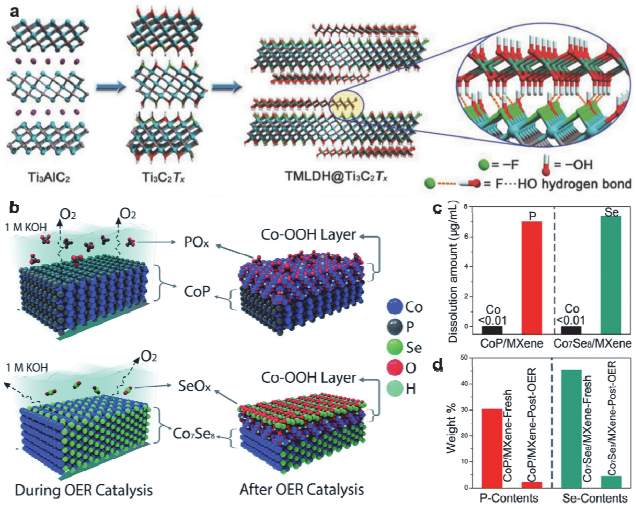

Fig. 25. (a) Synthesis of NFPS@MXene. Reprinted with permission from Ref. [250]. Copyright 2018, WILEY-VCH. (b) Schematic depicting the oxidation of the metal center and the anionic components with subsequent deposition. (c) Dissolved concentrations of Co, P and Se in the electrolyte after the OER. (d) P and Se contents of catalysts before and after the OER. Reprinted with permission from Ref. [120]. Copyright 2019, The Royal Society of Chemistry.

metal ions, combining the anions (P, Se) in catalysts with oxygen also affects the OER performance [120].

Vertically distributed CoP nanosheets were prepared on the surface of an MXene by *in-situ* phosphating Co-LDH/MXene [258]. A current density of 10 mA cm^{-2} was achieved at a battery voltage of 1.578 V when CoP/Ti_3C_2 was used to totally decompose water under alkaline conditions. In addition, hybrid HER catalysis occurs over the full pH range at low potentials. Electrons are transferred from TM atoms to the O atoms of terminal groups when the transition metal phosphide (TMP) is formed at the MXene interface, which weakens interactions between the TM atoms and the OER intermediate (HOO*) as well as those between the O atoms and the HER intermediate (H*) [259]. Despite the TMP being converted into oxides or hydroxides during the OER, Ti_3C_2@$NiCo_2O_4$ exhibited much poorer catalytic HER and OER properties than Ti_3C_2@mNiCoP synthesized by the same method [260].

7.5.4. Carbide/nitride-MXene heterojunctions

While Mo-based carbides exhibit similar catalytic HER performance to that of Pt, they disperse poorly and agglomerate easily [4,261,262]. Que *et al.* [135] successfully prepared P-Mo_2C/Ti_3C_2@NC by polymerization and annealing, in which the MXene acts as the conductive substrate and provides abundant anchorage sites and charge-transport pathways, while phosphorus-doped Mo_2C nanocrystalline dots coated with porous nitrogen-doped carbon outer layers are the HER active centers; MXene-based fabrication led to acidic HER properties (177 mV@10 mA cm^{-2}). Mo can be replaced by Co (with fewer electrons) to form the $Co_xMo_{2-x}C$ bimetallic carbide (Fig. 26(a)) [263]. The center of the p_z band on the $Co_xMo_{2-x}C$/NC carbon surface shifted upward as the number of electrons transferred from the carbide to the NC decreased, which lowered the water dissociation barrier; hence, the $Co_xMo_{2-x}C$/MXene/NC catalyst displayed good HER activity over a wide pH range (Figs. 26(b)–(e)).

Hybrids between MOFs (and their derivatives) and conductive MXenes are potential transition-metal electrocatalysts owing to their high specific surface areas and diverse metal centers and ligands [264–267]. Luo *et al.* [266] embedded 100–200 nm CoNi-ZIF-67 nanoparticles into the $Ti_3C_2T_x$ interlayer using the co-precipitation method, which led to a tenfold increase in the specific surface area (S_{BET}) of the MXene. The surface groups of the MXene interact with Co/Ni, increasing the valence of the metal and significantly enhancing OER activity, as evidenced by a low onset potential of 275 mV and Tafel slope of 65.1 mV dec^{-1}. Metal/nitrogen-doped carbon (MNC), which was prepared from a MOF by calcination at high temperature, inherited the advantages of the MOF and could be attached to the MXene substrate to avoid aggregation [2,268,269]. CoO_x-N-C/TiO_2C prepared by the calcination of CoZn-ZIF/$Ti_3C_2T_x$ at 800 °C was a three-function HER, OER, and ORR electrocatalyst [270]. A cell voltage of only 1.45 V was required at 10 mA cm^{-2} to split water when the catalyst acted as the electrode, which is ascribable to synergy between CoO_x, TiO_2, and graphitic carbon. While the high carbonization temperature ensured high catalytic MNC activity, it irreversibly damaged the MXene, leading to a prolonged charge- and mass-transfer pathway. Using the separation pyrolysis method, Yang *et al.* [269] prepared Fe-N-C@MXene by first carbonizing ZIF-8 at 1100 °C followed by annealing at 350 °C. The catalyst exhibited superior catalytic ORR activity and cycling stability in both alkaline and acidic electrolytes, with half-wave potentials of 0.887 and 0.777 V and restricted diffusion current densities of 6.3 and 5.7 mA cm^{-2}, respectively, which is attributable to

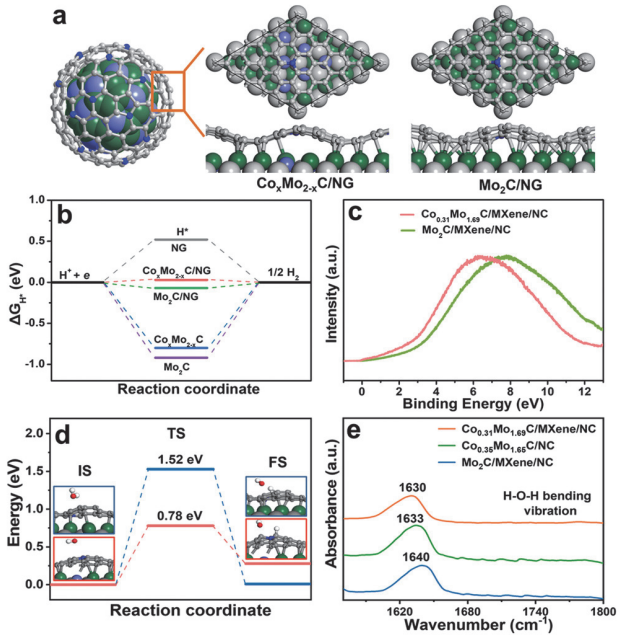

Fig. 26. (a) Structural models of $Co_xMo_{2-x}C$/NG and Mo_2C/NG. (C: silver N: blue, Mo: green, and Co: purple). DFT-calculated HER free energies (b) and reaction energies (d) for water dissociation on $Co_xMo_{2-x}C$/NG and Mo_2C/NG; UPS (c) and FTIR-ATR spectra (e) of $Co_xMo_{2-x}C$/MXene/NC and Mo_2C/MXene/NC. Reprinted with permission from Ref. [263]. Copyright 2019, Wiley-VCH.

the low charge-transfer impedance and high ECSA resulting from coupling between the intact MXene structure and Fe-N-C.

7.5.5. Oxide-MXene heterojunctions

The processes used to prepare metal nanoparticles have some disadvantages, such as long aging and reduction times, and the use of stabilizers and chemical reducing agents [271,272]. Oxides have been extensively researched as electrocatalysts because they are highly stable at high voltages. Zhu *et al*. [273] *in-situ* synthesized $TiOF_2$ nanospheres approximately 20 nm in size on an MXene with the same elemental composition as the MXene surface (Figs. 27(a) and (b)). The $TiOF_2$ increased the layer spacing and prevented the oxidation of the MXene, thereby improving the HER active-site utilization rate as well as the activity and stability of the catalyst. Assisted by solution plasma, He *et al*. [272] synthesized PtO_aPdO_b-NPs@$Ti_3C_2T_x$ nanosheets that were highly electrocatalytically active toward both the HER and OER (Fig. 27(c)), with a current density of 10 mA cm^{-2} achieved at only 1.52 V in an alkaline two-electrode system. HT-PtO_aPdO_bNPs@$Ti_3C_2T_x$ synthesized by the hydrothermal method contained more Pt than that synthesized by solution plasma; however, the former was less electrocatalytically active than the latter, which highlights that strong coupling between the mixed-valence metal oxide and MXene, rather than Pt, is the key factor for improving catalytic performance. Zhi *et al*. [274] prepared Mn_3O_4/MXene, the first heterogeneous non-noble-metal/MXene catalyst for the ORR, which exhibited the same onset potential as Pt/C under alkaline conditions (Fig. 27(d)). The poor conductivities and high diffusion barriers of Ni, Co, and other metal oxide nanomaterials can be improved through the use of MXene substrates, thereby enhancing their OER/ORR activities [118,275].

7.5.6. Hydroxide-MXene heterojunctions

MOOH is regarded to be the most essential active center, to which other transition-metal-based compounds are ultimately converted during the OER. Therefore, MOOH NSs/MXenes were synthesized with the aim of providing excellent electrocatalytic properties. For instance, Yan *et al*. [216] used a hydrothermal method to prepared the VOOH/$Ti_3C_2T_x$ bifunctional HER/OER electrocatalyst. Strong coupling interactions greatly reduce the local electron density at the V center, and the abundant mesoporous structure accelerates mass transfer, resulting in faster dynamics and enhanced performance. A cell composed of VOOH/$Ti_3C_2T_x$ electrodes delivered a current density of 10 mA cm^{-2} at 1.579 V. Li *et al*. [276] delivered improved OER performance by preparing FeOOH NSs/Ti_3C_2, which was prepared by reducing Fe^{2+} with $NaBH_4$ on Ti_3C_2. Furthermore, the MOOH modification (M = Ni, Fe, and V) on the surface of multilayer $V_4C_3T_x$ did not damage the internal MXene framework; the composite required an η_{10} of 275.2 mV for the OER and was highly durable in alkaline media [277]. Cui *et al*. [278] uniformly deposited FeOOH QDs onto a $Ti_3C_2T_x$ support by precipitating Fe^{3+} with ammonium bicarbonate; the $Ti_3C_2T_x$-FeOOH hybrid showed very stable but moderate OER activity, with an η_{10} of 430 mV in 1 mol/L KOH.

Fe-, Co-, and Ni-based hydroxides, including oxyhydroxide (MOOH) nanosheets and layered double hydroxides (LDHs), have been studied for efficient OER use [217]. LDH/MXene hybrids synthesized by *in-situ* growth rather than simple mixing not only preserved the excellent redox capacity of the cationic metal hydroxide layer of the LDH but also retained the high electrical conductivity of the MXene; hence, they have been widely studied as active OER catalysts [279]. The surface functional groups of the MXene adsorb and precipitate metal ions in the presence of urea, thereby promoting vertical LDH array growth and inhibiting MXene stacking (Fig. 28(a)) [280,281]. Yu *et al*. [127] synthesized a FeNi-LDH/Ti_3C_2 nanocomposite by co-precipitating Fe^{3+} and Ni^{2+} under reflux (Fig. 28(b)). Electrostatic interactions between the metal ions and functional groups, such as O and F, where approximately 0.09 e in each NiFe-LDH crystal cell is transferred to Ti_3C_2, not only leads to uniform loading, but also accelerates the $Ni^{2+}/Ni^{3+,4+}$ redox process. Theoretical calculations showed that high-valence metal ions activate oxidized oxygen ions in the LDH/MXene system to become electrophilic centers for the

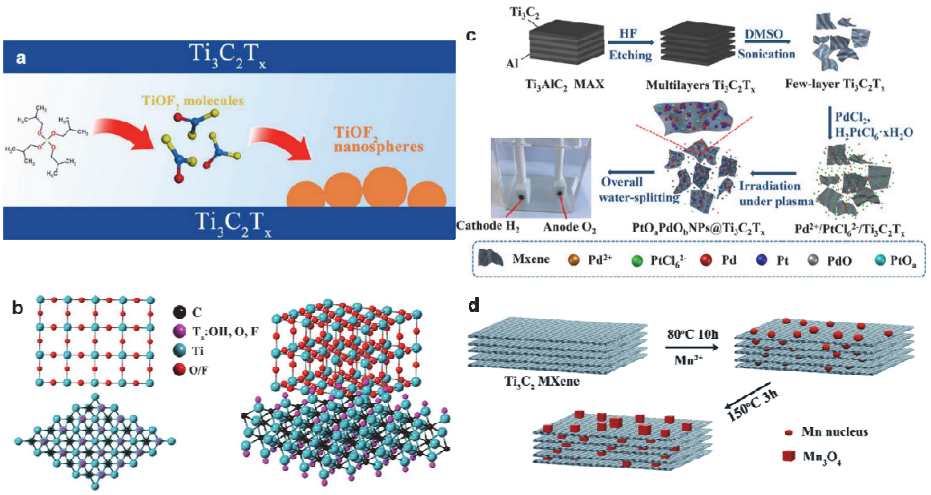

Fig. 27. (a) Synthesis of $TiOF_2$@$Ti_3C_2T_x$. (b) Interfacial structure of $TiOF_2$@$Ti_3C_2T_x$. Reprinted with permission from Ref. [273]. Copyright 2019, Elsevier. (c) Synthesis of PtO_aPdO_bNPs@$Ti_3C_2T_x$. Reprinted with permission from Ref. [272]. Copyright 2018, American Chemical Society. (d) Synthesis of Mn_3O_4/MXene. Reprinted with permission from Ref. [274]. Copyright 2017, The Royal Society of Chemistry.

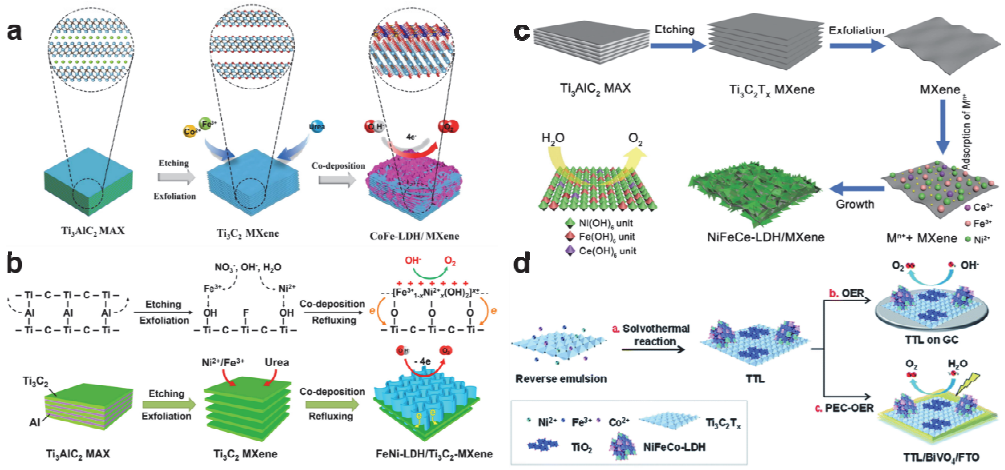

Fig. 28. Syntheses of CoFe-LDH/MXene (a), FeNi-LDH/Ti_3C_2-MXene (b), NiFeCe-LDH/MXene (c), and TTL (d). (a) Reprinted with permission from Ref [280]. Copyright 2019, Elsevier. (b) Reprinted with permission from Ref. [127]. Copyright 2017, Elsevier. (c) Reprinted with permission from Ref. [279]. Copyright 2020, Science Press. (d) Reprinted with permission from Ref. [283]. Copyright 2018, The Royal Society of Chemistry.

OER process, thereby increasing activity [280]. The above compound was subsequently coated on the surface of nickel foam to produce a new hybrid referred to as "NiFe-LDH/MXene/NF" [126]. The hybrid accelerated the HER by facilitating the Volmer step while retaining its original excellent OER activity. The battery assembled with the double-function NiFe-LDH/MXene/NF electrode as both the anode and cathode needed only 1.75 V to deliver a current density of 500 mA cm^{-2}, which is far superior to that generated by an alkaline electrolytic cell assembled using (+)RuO_2/NF//Pt/NF(−). More importantly, the electrode was observed to be highly durable (280 h), since LDH acts as a film that protects the MXene against oxidation at high potential, thereby ensuring structural stability and high conductivity [282]. The addition of a third metal to NiFe-LDH further reduced the OER overpotential [279,283]. The addition of Ce^{3+} as an isomorphic Fe^{3+} substituent not only increased the porosity of the LDH, but also effectively lowered the NiFe-LDH bandgap, thereby increasing the rate of the catalytic OER (Fig. 28(c)) [279]. The hybrid TTL solvothermally prepared by supporting ternary NiFeCo-LDH on partially oxidized $Ti_3C_2T_x$ showed good electrochemical OER activity (Fig. 28(d)) [283].

LDH was fixed on an MXene surface by electrodepositing a metal ion electrolyte solution on an MXene working electrode [119,221]. The ratio of the metal in the LDH was affected by the Co^{2+} and Ni^{2+} concentrations [119]. CoNi LDH/$Ti_3C_2T_x$-18, with a Co^{2+}/Ni^{2+} ratio of 1:1, showed the best OER performance, requiring only 257.4 mV to achieve 100 mA cm^{-2} in 1 mol/L NaOH, with a Tafel slope of 68 mV dec^{-1}. Metal ions were oxidized to high valence accompanied by the transfer of d-electrons to other atoms, which resulted in weaker binding between the LDH and reaction intermediates, which is advantageous for the OER.

7.5.7. Heterojunctions composed of carbon-based materials and MXenes

Two-dimensional carbon-based materials, such as carbon cloth, graphene, and C_3N_4, exhibit excellent electrocatalytic properties and are effective substitutes for noble-metal-based catalysts [158,284,285]. Both MXenes and graphene are HER and ORR active; the active sites in the former exist on the base surface, while they are edge vacancies in the latter [286]. Graphene can be activated by strong interfacial interactions with MXenes [287]. Ti forms covalent bonds with graphitic carbon when a single layer of graphite covers Ti_2C to form a sandwich-type heterostructure, which results in a semiconductor-to-metallic change in graphene properties [288]. The addition of nitrogen atoms to graphene at this time results in the carbon atoms close to the nitrogen atoms gaining additional electrons from the MXene, leading to appropriate binding strengths to HER and ORR intermediates (Figs. 29(a)–(d)) [287]. In particular, G/V_2C and G/Mo_2C have ORR and HER barriers of 0.2 and 1.3 eV, respectively. However, graphene electrostatically (rather than covalently) bonded to M_2CT_2 exhibited different catalytic performance to that of G/M_2C. Fortunately, the strengths of the electrostatic interactions and those involving two graphene layers are comparable, but stronger than those of the MXene layers, thereby avoiding MXene layer stacking [289,290]. Gao *et al.* [291] synthesized nitrogen-doped carbon nanosheets on MXene using polypyrrole as both the nitrogen and carbon source. The highly ordered carbon nanosheets exhibited high ORR activity, with graphitic and pyridinic nitrogens accounting for 66.3% and 17.6% of the total nitrogen, respectively, both of which are active sites for the ORR. The formation of CoN_x-G/MXene by the addition of Co promoted slow hydrogen evolution in alkaline media [292]. Chen *et al.* [125] modulated the surface charge of carbon nitride using Fe metal clusters, which spontaneously combined with the MXene to form a 2D/2D superlattice heterostructure. Fe-N-C/MXene showed a surface area twice that of individual Fe-N-C, leading to more exposed active sites, while interfacial synergy promoted charge transfer, all of which are favorable for oxygen adsorption.

The ability to inhibit MXene flake accumulation is an obvious advantage of carbon nanotubes [293]. Because of their reticulated structures and excellent electrical conductivities,

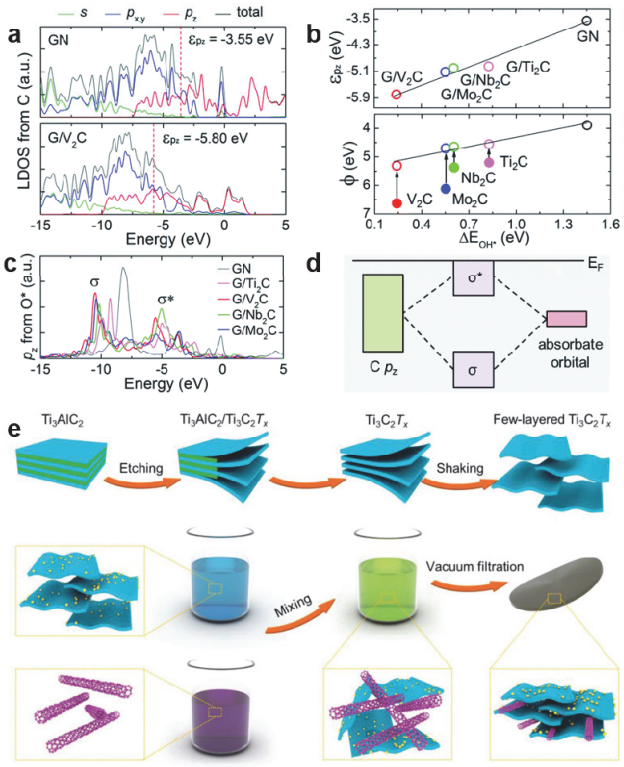

Fig. 29. (a) Local densities of states of surface C atoms on freestanding N-doped graphene and that supported by a V_2C monolayer. (b) The p_z band center (top panel) and work function (bottom panel) as functions of the lowest binding energy of the OH* species for various graphene/MXene heterostructures (colored open circles) and for GN. (c) DOSs of the p_z orbitals of O* species adsorbed on various graphene/MXene heterostructures and on GN. (d) Schematic diagram showing orbital hybridization between C and adsorbate atoms to form fully filled bonding (σ) and antibonding (σ^*) orbitals. Reprinted with permission from Ref. [287]. Copyright 2018, The Royal Society of Chemistry. (e) Preparation of fabrication of MXene@Pt/SWCNTs. Reprinted with permission from Ref. [164]. Copyright 2020, WILEY-VCH.

single-walled carbon nanotubes can be used to bind MXenes to HER catalysts, which neither inhibits charge transfer nor impedes active-site exposure. Wang *et al.* [164] used vacuum-assisted filtration to construct S-M-1Pt and S-M-5Pt films from a mixed colloidal suspension containing MXene@Pt and SWCNTs (Fig. 29(e)). The five-layer S-M-5Pt film exhibited an η_{10} value of 17 mV in 0.5 mol/L H_2SO_4, which was stably maintained for 800 h during the HER. Array-arranged carbon nanotubes can be grown *in situ* on the surface of an MXene by annealing the organics attached to the MXene, which ensures strong interactions across heterogeneous interfaces. Melamine containing a metal cation was first adsorbed onto a negatively charged MXene and then annealed at high temperature to form CNTs@MXene [294]. The CNTs act as conductive bridges between the $Ti_3C_2T_x$ layers, shortening the mass- and charge-transfer pathways, and promoting the alkaline HER (η_{10} = 93 mV). In terms of cobalt species, ZIF-67 and dicyandiamide were converted into cobalt-tipped carbon nanotubes on MXene [124,295]. Owing to the carbon nanotube coating, the small cobalt nanoparticle tips were limited in size and did not grow further. Abundant Co-N/C, carbon nanotube defect sites, and MXene/CNT synergy resulted in the nanocomposite exhibiting electrocatalytic ORR and OER activities in an alkaline electrolyte. Co-CNT/Ti_3C_2-60 exhibited a similar half-wave potential and diffusion-limiting current density to those of commercial Pt/C in 0.1 mol/L KOH, but the Tafel slope of 63 mV dec^{-1} is much lower than that of commercial Pt/C [124]. In addition, the 3D hybrid was found to be highly stable and resistant to methanol crossing; hence it is a promising material for practical battery applications.

7.5.8. *BP-MXene heterojunctions*

The anisotropy of puckered orthorhombic black phosphorus (BP), as a 2D material, engenders it with bandgap tunability and a high hole/charge-transfer rate [296,297]; BP was recently reported to catalyze the OER [5]. While few-layer BP exhibited an onset potential of 1.45 V for the OER in 1 mol/L KOH, its catalytic efficiency was insufficient at high voltage due to its poor conductivity [298]. The nature of BP transforms from semiconductor to metallic only at high pressure (1.7 GPa), which greatly limits its electrocatalysis applications [299]. BP/graphene coupling has been shown to improve BP conductivity [300]. Highly conductive MXene was also selected as a BP substrate, and BPQD/TNS, in which BP quantum dots (BP QDs) are uniformly dispersed on Ti_3C_2, was synthesized by ultrasonication and freeze drying, and was subsequently used for lithium storage (Fig. 30(a)) [301]. Liu *et al.* [235] prepared an HER/OER bifunctional electrode by self-assembling BP QDs

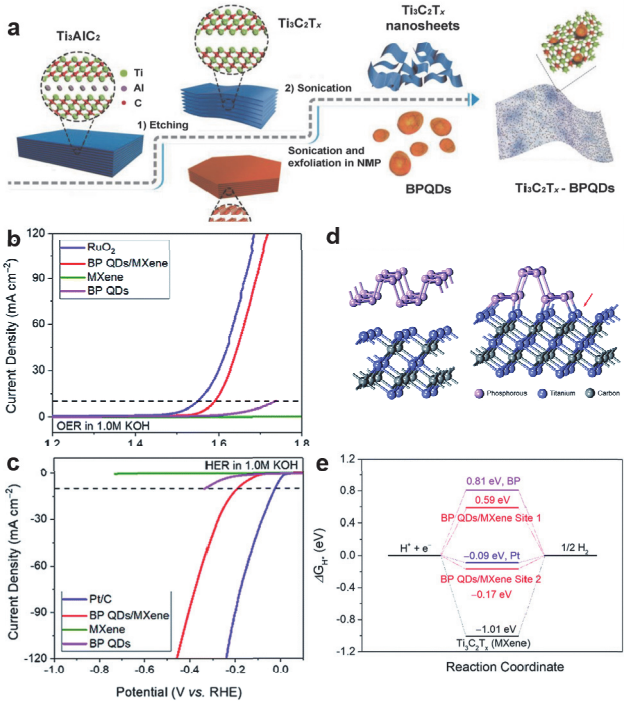

Fig. 30. (a) Synthesis of BPQD/TNS. Reprinted with permission from Ref. [301]. Copyright 2018, WILEY-VCH. (b,c) HER and OER performance of BP QDs/MXene. (d) Computational models for BP, $Ti_3C_2T_x$ and BP QDs/MXene. (e) Diagram showing calculated ΔG for the HER on various electrocatalysts. Sites 1 and 2 that correspond to the adsorption of H* above the BP QDs and near the interface are highlighted in red. Reprinted with permission from Ref. [235]. Copyright 2018, The Royal Society of Chemistry.

onto MXene using van der Waals forces. The BP QDs were 2.5–6.5 nm in size and accounted for 48.2 wt% of the nanohybrid. $Ti_3C_2T_x$ has a negative ΔG_H^* (−1.01 eV) for the HER, while that of BP is positive (0.81 eV); $|\Delta G_H^*|$ was observed to decreased to 0.59 eV at site 1 and 0.17 eV at site 2 as BP was loaded into the $Ti_3C_2T_x$, indicative of significantly higher HER activity (Figs. 30(d) and (e)). Moreover, strong interactions between water and the hybrid are also indicative of good OER activity. A current density of 10 mA cm^{-2} was achieved by the bifunctional electrode at 1.78 V when water was totally decomposed in 1 mol/L KOH (Figs. 30(b) and (c)). Electrocatalysis data for the MXene-based hybrids are summarized in Tables 2–4.

Table 2
HER performance data for MXene-based hybrids.

Catalyst	Electrolyte	η_{10} (mV)	Tafel slope (mV dec^{-1})	Ref.
Ru@B-$Ti_3C_2T_x$	0.5 mol/L H_2SO_4	62.9	100	[29]
Pt NCs-MXene	0.5 mol/L H_2SO_4	40	50.8	[59]
40Pt-TBA-$Ti_3C_2T_x$	0.5 mol/L H_2SO_4	67.8	69.8	[110]
TBA-$Ti_3C_2T_x$-Pt-20	0.5 mol/L H_2SO_4	55	65	[111]
Pt/$Ti_3C_2T_x$-550	1 mol/L KOH	32.7	32.3	[85]
$Ti_3C_2T_x$@0.1Pt	0.5 mol/L H_2SO_4	43	80	[89]
P-Mo_2C/Ti_3C_2@NC	0.5 mol/L H_2SO_4	177	57.3	[135]
MoS_2/Ti_3C_2-MXene@C	0.5 mol/L H_2SO_4	135	45	[236]
Mo_2CT_x/2H-MoS_2	0.5 mol/L H_2SO_4	119	60	[238]
$MoS_2 \perp Ti_3C_2$@220	0.5 mol/L H_2SO_4	95	40	[239]
MD-Ti_3C_2/MoS_x-100	0.5 mol/L H_2SO_4	165	41	[244]
MoS_2-Ti_3C_2	0.5 mol/L H_2SO_4	98	45	[115]
CoS_2@MXene	0.1 mol/L KOH	175	97	[65]
$TiOF_2$@$Ti_3C_2T_x$	0.5 mol/L H_2SO_4	103	56.2	[273]
S-M-5Pt	0.5 mol/L H_2SO_4	62	78	[164]
PtO_aPdO_bNPs@$Ti_3C_2T_x$	0.5 mol/L H_2SO_4	26.5	39	[272]
CoP/MXene	1 mol/L KOH	113	57	[120]
	0.5 mol/L H_2SO_4	71	57.6	
CoP/Ti_3C_2 MXene	1 mol/L PBS	124	96.8	[258]
	1 mol/L KOH	102	68.7	
Ti_3C_2@mNiCoP	1 mol/L KOH	127	103	[260]
	1 mol/L KOH	112	67.1	
Ti_2NT_x@MOF-CoP	1 mol/L PBS	131	125.6	[66]
	0.5 mol/L H_2SO_4	129	96.7	
	0.5 mol/L H_2SO_4	81	24	
$Co_{0.31}Mo_{1.69}C$/MXene/NC	0.1 mol/L PBS	126	46	[263]
	1 mol/L KOH	75	32	
P-TiO_2@Ti_3C_2	1 mol/L KOH	97	48.4	[202]
MX@C	1 mol/L KOH	134	32	[206]
NiS_2/V-MXene	1 mol/L KOH	179	85	[245]
Co-MoS_2/Mo_2CT_x	1 mol/L KOH	112	82	[234]
Ag@N-$Ti_3C_2T_x$	1 mol/L KOH	153	137.9	[223]
Ni_2P/$Ti_3C_2T_x$/NF	1 mol/L KOH	135	86.6	[226]
3D CNTs@$Ti_3C_2T_x$	1 mol/L KOH	93	128	[294]
1T/2H $MoSe_2$/MXene	1 mol/L KOH	95	91	[248]
$NiSe_2$/$Ti_3C_2T_x$	2 mol/L KOH	200	37.7	[246]
$Ni_{0.7}Fe_{0.3}PS_3$@MXene	1 mol/L KOH	282	36.5	[250]
VOOH/$Ti_3C_2T_x$	1 mol/L KOH	100	81.8	[216]
NiFe-LDH/MXene/NF	1 mol/L KOH	132	70	[126]
$NiFe_2O_4$/Ti_3C_2	0.5 mol/L KOH	173	112.2	[31]
Co-CoO/Ti_3C_2-MXene	1 mol/L KOH	45	47	[220]
BP QDs/MXene	1 mol/L KOH	190	83	[235]

Table 3
OER performance data for MXene-based hybrids.

Catalyst	Electrolyte	η_{10} (mV)	Tafel slope (mV dec^{-1})	Ref.
CoNi-ZIF-67@$Ti_3C_2T_x$	0.1 mol/L KOH	323	65.1	[266]
$Ti_3C_2T_x$/TiO_2/NiFeCo-LDH	0.1 mol/L KOH	320	98.4	[283]
PtO_aPdO_bNPs@$Ti_3C_2T_x$	0.1 mol/L KOH	320	78	[272]
Co-CoO/Ti_3C_2-MXene	1 mol/L KOH	271	47	[220]
$NiFe_2O_4$/Ti_3C_2	0.5 mol/L KOH	266	73.6	[31]
FeOOH NSs/Ti_3C_2	1 mol/L KOH	400	95	[276]
M_3OOH@$V_4C_3T_x$	1 mol/L KOH	275.2	51.4	[277]
$Ti_3C_2T_x$-FeOOH	1 mol/L KOH	430	31.7	[278]
CoFe-LDH/MXene	1 mol/L KOH	319	50	[280]
FeCo-LDH/MXene	1 mol/L KOH	268	85	[281]
NiFeCe-LDH/MXene	1 mol/L KOH	260	42.8	[279]
FeNi-LDH/Ti_3C_2-MXene	1 mol/L KOH	298	43	[127]
Co-LDH@$Ti_3C_2T_x$	1 mol/L KOH	340	82	[282]
CoNi LDH/$Ti_3C_2T_x$	1 mol/L KOH	—	68	[119]
NiFe LDH/N_{10}TC/NF	1 mol/L KOH	196	68.4	[221]
NiCoFe-LDH/Ti_3C_2 MXene/NCNT	0.1 mol/L KOH	332	60	[30]
VOOH/$Ti_3C_2T_x$	1 mol/L KOH	238	81.6	[216]
NiFe-LDH/MXene/NF	1 mol/L KOH	229	44	[126]
1T/2H $MoSe_2$/MXene	1 mol/L KOH	340	90	[248]
$Ni_{0.9}Fe_{0.1}PS_3$@MXene	1 mol/L KOH	196	114	[250]
CoS_2@MXene	0.1 mol/L KOH	270	92	[65]
CoP/MXene	1 mol/L KOH	230	50	[120]
CoP/Ti_3C_2 MXene	1 mol/L KOH	280	95.4	[258]
Ti_3C_2@mNiCoP	1 mol/L KOH	237	104	[260]
BP QDs/MXene	1 mol/L KOH	360	64.3	[235]

8. Summary and outlook

The numerous surface-active sites, large surface areas, high conductivities, and other favorable properties of MXenes are very applicable to electrocatalysis. In this review, we summarize the design principles and synthesis strategies for MXene-based electrocatalysts and emphasize structure-activity relationships for the HER, OER, and ORR. While pristine 2D Mo_2CT_x and Ti_2CT_x nanosheets exhibit HER performance without additional modification, to date most MXene HER activities and all OER/ORR activities have been derived using strategies that include surface modification, lattice substitution, defect engineering, morphology control, and heterojunction construction. Atomic-species and arrangement diversities enable MXenes to be designed at the atomic level, which provides both opportunities and challenges. Introducing heteroatoms into an MXene can adjust its electronic state to ensure that reaction intermediates are moderately adsorbed. For example, heteroatom doping has led to the syntheses of excellently performing single-atom catalysts. Heterojunctions constructed with MXenes as carriers are more likely to show excellent catalytic activities and stabilities. Coupling between an active phase (with its own active sites) and a highly conductive MXene reduces the surface work function, improves the stability of the

Table 4
ORR performance data for MXene-based hybrids.

Catalyst	Electrolyte	E_{onset} (V *vs.* RHE)	$E_{1/2}$ (V *vs.* RHE)	Ref.
$Ru/Ti_3C_2T_x$	0.1 mol/L $HClO_4$	0.92	0.80	[121]
$Pt/Ti_3C_2T_x$	0.1 mol/L $HClO_4$	—	0.847	[302]
$Pt/Ti_3C_2T_x$	1 mol/L KOH	0.95	—	[224]
$MXene/NW\text{-}Ag_{0.9}Ti_{0.1}$	1 mol/L KOH	0.921	0.782	[225]
$Pt\ NWs/Ti_3C_2T_x\text{-}CNT$	0.1 mol/L $HClO_4$	1.02	0.896	[303]
$Pt/CNT\text{-}Ti_3C_2T_x$	0.1 mol/L $HClO_4$	—	0.876	[304]
$Pd/Ti_3C_2T_x\text{-}CNT$	0.1 mol/L KOH	1.085	0.925	[293]
$FeCo\text{-}N\text{-}d\text{-}Ti3C_2$	0.1 mol/L KOH	0.96	0.80	[305]
$Fe\text{-}N\text{-}C@Ti_3C_2T_x$	0.1 mol/L $HClO_4$ 0.1 mol/L KOH	— —	0.777 0.887	[269]
$Fe\text{-}N\text{-}C/Ti_3C_2T_x$	0.1 mol/L KOH	1	0.814	[306]
$Fe\text{-}N\text{-}C/Ti_3C_2T_x$	0.1 mol/L KOH	0.92	0.84	[125]
$FePc/Ti_3C_2T_x$	0.1 mol/L KOH	0.97	0.89	[307]
$g\text{-}C_3N_4/Ti_3C_2$	0.1 mol/L KOH	0.92	0.79	[105]
$MoS_2QDs@Ti_3C_2T_xQDs@MWCNTs$	1.0 mol/L KOH	0.87	0.75	[205]
MXene@PPy-800	0.1 mol/L KOH	0.85	0.710	[291]
$Co\text{-}CNT/Ti_3C_2\text{-}60$	0.1 mol/L KOH	—	0.820	[124]
$Ti_3C_2/NSCD\text{-}600$	0.1 mol/L KOH	0.98	0.81	[308]
$Co_3O_4/NCNT/Ti_3C_2$	0.1 mol/L KOH	—	0.79	[309]
$CoS_2@MXene$	0.1 mol/L KOH	0.87	0.80	[65]
$NiFeMn\text{-}N/N\text{-}Ti_3C_2$	0.1 mol/L KOH	0.95	0.84	[310]
$N\text{-}CoSe_2/Ti_3C_2T_x$	0.1 mol/L KOH	0.95	0.79	[311]
$NiCo_2O_4/MXene$	0.1 mol/L KOH	—	0.70	[118]
$Mn_3O_4/MXene$	0.1 mol/L KOH	0.89	—	[274]
$NiCoFe\text{-}LDH/Ti_3C_2$ MXene/NCNT	0.1 mol/L KOH	0.93	0.78	[30]

MXene, avoids sheet aggregation, and increases the active-site utilization rate, thereby enhancing electrocatalytic activity. Unfortunately, no further information on such heterojunction interfaces, other than their coordination structures, appears to exist; therefore, the specific role of the interface remains unclear.

Despite the existence of various strategies for overcoming the weaknesses of MXenes, research is still in its early stages. First, the metallic properties and stability of an MXene appears to depend completely on its flake structure, and hot pressing and acid etching cannot guarantee a controllable structure. Therefore, the development of efficient and green methods for the syntheses of materials with controllable structures and defects is necessary. In addition, more *in-situ* characterization studies and theoretical calculations are required to better explain the electrocatalytic HER/OER/ORR mechanisms. Moreover, the abundance of variety is the biggest advantage that MXenes have over other 2D materials; however, only a few types of MXene have been successfully synthesized and used in electrocatalysis applications. MXenes based on middle and late transition metals, which display theoretically superior properties, have not been synthesized to date, and N-based MXenes also require further study. In addition, studies into ordered alloying and disordered solid solutions of MXenes are rare, with almost no experimental data and only a few theoretical predictions reported. Machine learning needs to be more fully used when designing and sorting promising pristine MXenes prior to experimental work. Overall, MXenes are new 2D materials with strong electrocatalysis potential; they are expected to flourish in the electrocatalysis field and even become extended to other fields if more MXene-based nanocomposites can be easily fabricated.

References

[1] Y. Y. Birdja, E. Pérez-Gallent, M. C. Figueiredo, A. J. Göttle, F. Calle-Vallejo, M. T. M. Koper, *Nat. Energy*, **2019**, 4, 732–745.
[2] L. Shang, H. Yu, X. Huang, T. Bian, R. Shi, Y. Zhao, G. I. N. Waterhouse, L.-Z. Wu, C.-H. Tung, T. Zhang, *Adv. Mater.*, **2016**, 28, 1668–1674.
[3] T. F. Jaramillo, K. P. Jorgensen, J. Bonde, J. H. Nielsen, S. Horch, I. Chorkendorff, *Science*, **2007**, 317, 100–102.
[4] J.-S. Li, Y. Wang, C.-H. Liu, S.-L. Li, Y.-G. Wang, L.-Z. Dong, Z.-H. Dai, Y.-F. Li, Y.-Q. Lan, *Nat. Commun.*, **2016**, 7, 11204.
[5] Q. Jiang, L. Xu, N. Chen, H. Zhang, L. Dai, S. Wang, *Angew. Chem. Int.*

Graphical Abstract

Chin. J. Catal., 2022, 43: 2057–2090 doi: 10.1016/S1872-2067(21)64030-5

MXenes for electrocatalysis applications: Modification and hybridization

Xue Bai, Jingqi Guan *
Jilin University

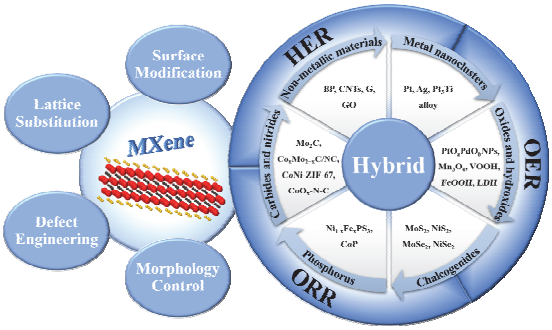

This review summarizes the progress of MXene-based electrocatalysts for the HER, OER, and ORR, including regulating pristine MXenes and modifying hybrid MXenes, from both theoretical and experimental perspectives.

Ed., **2016**, 55, 13849–13853.
[6] D. Zhou, Z. Cai, X. Lei, W. Tian, Y. Bi, Y. Jia, N. Han, T. Gao, Q. Zhang, Y. Kuang, J. Pan, X. Sun, X. Duan, *Adv. Energy Mater.*, **2018**, 8, 1701905.
[7] L. Cheng, X. Li, H. Zhang, Q. Xiang, *J. Phys. Chem. Lett.*, **2019**, 10, 3488–3494.
[8] K. Li, S. Zhang, Y. Li, J. Fan, K. Lv, *Chin. J. Catal.*, **2021**, 42, 3–14.
[9] Q. Zhong, Y. Li, G. Zhang, *Chem. Eng. J.*, **2021**, 409, 128099.
[10] L. Yao, Q. Gu, X. Yu, *ACS Nano*, **2021**, 15, 3228–3240.
[11] C. Chen, X. Xie, B. Anasori, A. Sarycheva, T. Makaryan, M. Zhao, P. Urbankowski, L. Miao, J. Jiang, Y. Gogotsi, *Angew. Chem. Int. Ed.*, **2018**, 57, 1846–1850.
[12] T. Shang, Z. Lin, C. Qi, X. Liu, P. Li, Y. Tao, Z. Wu, D. Li, P. Simon, Q. H. Yang, *Adv. Funct. Mater.*, **2019**, 29, 1903960.
[13] L. Yu, L. Hu, B. Anasori, Y.-T. Liu, Q. Zhu, P. Zhang, Y. Gogotsi, B. Xu, *ACS Energy Lett.*, **2018**, 3, 1597–1603.
[14] A. S. Levitt, M. Alhabeb, C. B. Hatter, A. Sarycheva, G. Dion, Y. Gogotsi, *J. Mater. Chem. A*, **2019**, 7, 269–277.
[15] J. Liu, H. B. Zhang, R. Sun, Y. Liu, Z. Liu, A. Zhou, Z. Z. Yu, *Adv. Mater.*, **2017**, 29, 1702367.
[16] L. Liang, R. Yang, G. Han, Y. Feng, B. Zhao, R. Zhang, Y. Wang, C. Liu, *ACS Appl. Mater. Interfaces*, **2020**, 12, 2644–2654.
[17] P. Song, H. Qiu, L. Wang, X. Liu, Y. Zhang, J. Zhang, J. Kong, J. Gu, *Sustain. Mater. Technol.*, **2020**, 24, e00153.
[18] Y.-J. Wan, K. Rajavel, X.-M. Li, X.-Y. Wang, S.-Y. Liao, Z.-Q. Lin, P.-L. Zhu, R. Sun, C.-P. Wong, *Chem. Eng. J.*, **2021**, 408, 127303.
[19] Y. Ma, Y. Yue, H. Zhang, F. Cheng, W. Zhao, J. Rao, S. Luo, J. Wang, X. Jiang, Z. Liu, N. Liu, Y. Gao, *ACS Nano*, **2018**, 12, 3209–3216.
[20] J. Liu, H. B. Zhang, X. Xie, R. Yang, Z. Liu, Y. Liu, Z. Z. Yu, *Small*, **2018**, 14, 1802479.
[21] Z. Yang, L. Jiang, J. Wang, F. Liu, J. He, A. Liu, S. Lv, R. You, X. Yan, P. Sun, C. Wang, Y. Duan, G. Lu, *Sens. Actuator B*, **2021**, 326, 128828.
[22] A. D. Handoko, S. N. Steinmann, Z. W. Seh, *Nanoscale Horiz.*, **2019**, 4, 809–827.
[23] G. Deysher, C. E. Shuck, K. Hantanasirisakul, N. C. Frey, A. C. Foucher, K. Maleski, A. Sarycheva, V. B. Shenoy, E. A. Stach, B. Anasori, Y. Gogotsi, *ACS Nano*, **2020**, 14, 204–217.
[24] X. Sang, Y. Xie, D. E. Yilmaz, R. Lotfi, M. Alhabeb, A. Ostadhossein, B. Anasori, W. Sun, X. Li, K. Xiao, P. R. C. Kent, A. C. T. van Duin, Y. Gogotsi, R. R. Unocic, *Nat. Commun.*, **2018**, 9, 2266.
[25] T. Y. Ma, J. L. Cao, M. Jaroniec, S. Z. Qiao, *Angew. Chem. Int. Ed.*, **2016**, 55, 1138–1142.
[26] Z. W. Seh, K. D. Fredrickson, B. Anasori, J. Kibsgaard, A. L. Strickler, M. R. Lukatskaya, Y. Gogotsi, T. F. Jaramillo, A. Vojvodic, *ACS Energy Lett.*, **2016**, 1, 589–594.
[27] X. Chen, X. Zhai, J. Hou, H. Cao, X. Yue, M. Li, L. Chen, Z. Liu, G. Ge, X. Guo, *Chem. Eng. J.*, **2021**, 420, 129832.
[28] B. Ding, W.-J. Ong, J. Jiang, X. Chen, N. Li, *Appl. Surf. Sci.*, **2020**, 500, 143987.
[29] M. Bat-Erdene, M. Batmunkh, B. Sainbileg, M. Hayashi, A. S. R. Bati, J. Qin, H. Zhao, Y. L. Zhong, J. G. Shapter, *Small*, **2021**, 17, 2102218.
[30] M. Faraji, N. Arianpouya, *J. Electroanal. Chem.*, **2021**, 901, 115797.
[31] P. V. Shinde, P. Mane, B. Chakraborty, C. Sekhar Rout, *J. Colloid Interface Sci.*, **2021**, 602, 232–241.
[32] L. M. Azofra, N. Li, D. R. MacFarlane, C. Sun, *Energy Environ. Sci.*, **2016**, 9, 2545–2549.
[33] W. Peng, M. Luo, X. Xu, K. Jiang, M. Peng, D. Chen, T. S. Chan, Y. Tan, *Adv. Energy Mater.*, **2020**, 10, 2001364.
[34] J. Zhao, L. Zhang, X.-Y. Xie, X. Li, Y. Ma, Q. Liu, W.-H. Fang, X. Shi, G. Cui, X. Sun, *J. Mater. Chem. A*, **2018**, 6, 24031–24035.
[35] Y. Fang, Z. Liu, J. Han, Z. Jin, Y. Han, F. Wang, Y. Niu, Y. Wu, Y. Xu, *Adv. Energy Mater.*, **2019**, 9, 1803406.
[36] Q. Zhao, C. Zhang, R. Hu, Z. Du, J. Gu, Y. Cui, X. Chen, W. Xu, Z. Cheng, S. Li, B. Li, Y. Liu, W. Chen, C. Liu, J. Shang, L. Song, S. Yang, *ACS Nano*, **2021**, 15, 4927–4936.
[37] N. Li, X. Chen, W. J. Ong, D. R. MacFarlane, X. Zhao, A. K. Cheetham, C. Sun, *ACS Nano*, **2017**, 11, 10825–10833.
[38] F. He, B. Zhu, B. Cheng, J. Yu, W. Ho, W. Macyk, *Appl. Catal. B*, **2020**, 272, 119006.
[39] Z. Zeng, Y. Yan, J. Chen, P. Zan, Q. Tian, P. Chen, *Adv. Funct. Mater.*, **2019**, 29, 1806500.
[40] C. Yang, Q. Tan, Q. Li, J. Zhou, J. Fan, B. Li, J. Sun, K. Lv, *Appl. Catal. B*, **2020**, 268, 118738.
[41] Q. Zhang, Y. Li, T. Chen, L. Li, S. Shi, C. Jin, B. Yang, S. Hou, *J. Electroanal. Chem.*, **2021**, 894, 115338.
[42] Y. Sun, Y. Zhou, Y. Liu, Q. Wu, M. Zhu, H. Huang, Y. Liu, M. Shao, Z. Kang, *Nano Res.*, **2020**, 13, 2683–2690.
[43] Z. Lang, Z. Zhuang, S. Li, L. Xia, Y. Zhao, Y. Zhao, C. Han, L. Zhou, *ACS Appl. Mater. Interfaces*, **2020**, 12, 2400–2406.
[44] C. Yang, Q. Jiang, H. Liu, L. Yang, H. He, H. Huang, W. Li, *J. Mater. Chem. A*, **2021**, 9, 15432–15440.
[45] Z. Jin, C. Liu, Z. Liu, J. Han, Y. Fang, Y. Han, Y. Niu, Y. Wu, C. Sun, Y. Xu, *Adv. Energy Mater.*, **2020**, 10, 2000797.
[46] Y. Ding, J. Zhang, A. Guan, Q. Wang, S. Li, A. M. Al-Enizi, L. Qian, L. Zhang, G. Zheng, *Nano Converg*, **2021**, 8, 14.
[47] K. Chu, Y. Luo, P. Shen, X. Li, Q. Li, Y. Guo, *Adv. Energy Mater.*, **2022**, 12, 2103022.
[48] V. M. Hong Ng, H. Huang, K. Zhou, P. S. Lee, W. Que, J. Z. Xu, L. B. Kong, *J. Mater. Chem. A*, **2017**, 5, 3039–3068.
[49] S. G. Peera, C. Liu, J. Shim, A. K. Sahu, T. G. Lee, M. Selvaraj, R. Koutavarapu, *Ceram. Int.*, **2021**, 47, 28106–28121.
[50] S. Sultan, J. N. Tiwari, A. N. Singh, S. Zhumagali, M. Ha, C. W. Myung, P. Thangavel, K. S. Kim, *Adv. Energy Mater.*, **2019**, 9, 1900624.
[51] S. Ghosh, R. N. Basu, *Nanoscale*, **2018**, 10, 11241–11280.
[52] V. Vij, S. Sultan, A. M. Harzandi, A. Meena, J. N. Tiwari, W.-G. Lee, T. Yoon, K. S. Kim, *ACS Catal.*, **2017**, 7, 7196–7225.
[53] G. Zhao, K. Rui, S. X. Dou, W. Sun, *Adv. Funct. Mater.*, **2018**, 28, 1803291.
[54] Z. W. Seh, J. Kibsgaard, C. F. Dickens, I. Chorkendorff, J. K. Norskov, T. F. Jaramillo, *Science*, **2017**, 355, eaad4998.
[55] Y. Zhu, Q. Lin, Y. Zhong, H. A. Tahini, Z. Shao, H. Wang, *Energy Environ. Sci.*, **2020**, 13, 3361–3392.
[56] W. Sheng, Z. Zhuang, M. Gao, J. Zheng, J. G. Chen, Y. Yan, *Nat. Commun.*, **2015**, 6, 5848.
[57] H. Nam, E. S. Sim, M. Je, H. Choi, Y. C. Chung, *ACS Appl. Mater. Interfaces*, **2021**, 13, 37035–37043.
[58] R. Luo, R. Li, C. Jiang, R. Qi, M. Liu, C. Luo, H. Lin, R. Huang, H. Peng, *Int. J. Hydrogen Energy*, **2021**, 46, 32536–32545.
[59] X. Jian, T.-T. Wei, M.-M. Zhang, R. Li, J.-X. Liu, Z.-H. Liang, *J. Electrochem. Soc.*, **2021**, 168, 096504.
[60] N. T. Suen, S. F. Hung, Q. Quan, N. Zhang, Y. J. Xu, H. M. Chen, *Chem. Soc. Rev.*, **2017**, 46, 337–365.
[61] R. Ma, G. Lin, Y. Zhou, Q. Liu, T. Zhang, G. Shan, M. Yang, J. Wang, *NPJ Comput. Mater.*, **2019**, 5, 1–15.
[62] A. Valdes, J. Brillet, M. Gratzel, H. Gudmundsdottir, H. A. Hansen, H. Jonsson, P. Klupfel, G. J. Kroes, F. Le Formal, I. C. Man, R. S. Martins, J. K. Norskov, J. Rossmeisl, K. Sivula, A. Vojvodic, M. Zach, *Phys. Chem. Chem. Phys.*, **2012**, 14, 49–70.
[63] C. Hu, L. Zhang, J. Gong, *Energy Environ. Sci.*, **2019**, 12, 2620–2645.
[64] I. E. Stephens, A. S. Bondarenko, F. J. Perez-Alonso, F. Calle-Vallejo, L. Bech, T. P. Johansson, A. K. Jepsen, R. Frydendal, B. P. Knudsen, J. Rossmeisl, I. Chorkendorff, *J. Am. Chem. Soc.*, **2011**, 133, 5485–5491.

[65] S. Han, Y. Chen, Y. Hao, Y. Xie, D. Xie, Y. Chen, Y. Xiong, Z. He, F. Hu, L. Li, J. Zhu, S. Peng, *Sci. China Mater.*, **2020**, 64, 1127–1138.
[66] H. Zong, R. Qi, K. Yu, Z. Zhu, *Electrochim. Acta*, **2021**, 393, 139068.
[67] Q. Tang, Z. Zhou, P. Shen, *J. Am. Chem. Soc.*, **2012**, 134, 16909–16916.
[68] M. Ghidiu, M. R. Lukatskaya, M. Q. Zhao, Y. Gogotsi, M. W. Barsoum, *Nature*, **2014**, 516, 78–81.
[69] Z. Ling, C. E. Ren, M. Q. Zhao, J. Yang, J. M. Giammarco, J. Qiu, M. W. Barsoum, Y. Gogotsi, *Proc. Natl. Acad. Sci. USA*, **2014**, 111, 16676–16681.
[70] A. Lipatov, M. Alhabeb, M. R. Lukatskaya, A. Boson, Y. Gogotsi, A. Sinitskii, *Adv. Electronic Mater.*, **2016**, 2, 1600255.
[71] H. Ghassemi, W. Harlow, O. Mashtalir, M. Beidaghi, M. R. Lukatskaya, Y. Gogotsi, M. L. Taheri, *J. Mater. Chem. A*, **2014**, 2, 14339–14343.
[72] Z. Li, L. Wang, D. Sun, Y. Zhang, B. Liu, Q. Hu, A. Zhou, *Mater. Sci. Eng. B*, **2015**, 191, 33–40.
[73] K. Wang, Y. Zhou, W. Xu, D. Huang, Z. Wang, M. Hong, *Ceram. Int.*, **2016**, 42, 8419–8424.
[74] M. Wu, B. Wang, Q. Hu, L. Wang, A. Zhou, *Materials*, **2018**, 11, 2112.
[75] J. Li, Y. Du, C. Huo, S. Wang, C. Cui, *Ceram. Int.*, **2015**, 41, 2631–2635.
[76] Z. Guo, J. Zhou, C. Si, Z. Sun, *Phys. Chem. Chem. Phys.*, **2015**, 17, 15348–15354.
[77] Z. H. Fu, Q. F. Zhang, D. Legut, C. Si, T. C. Germann, T. Lookman, S. Y. Du, J. S. Francisco, R. F. Zhang, *Phy. Rev. B*, **2016**, 94, 104103.
[78] A. Lipatov, H. Lu, M. Alhabeb, B. Anasori, A. Gruverman, Y. Gogotsi, A. Sinitskii, *Sci. Adv.*, **2018**, 4, eaat0491.
[79] A. Lipatov, M. Alhabeb, H. Lu, S. Zhao, M. J. Loes, N. S. Vorobeva, Y. Dall'Agnese, Y. Gao, A. Gruverman, Y. Gogotsi, A. Sinitskii, *Adv. Electronic Mater.*, **2020**, 6, 1901382.
[80] N. C. Frey, J. Wang, G. I. Vega Bellido, B. Anasori, Y. Gogotsi, V. B. Shenoy, *ACS Nano*, **2019**, 13, 3031–3041.
[81] C. Xu, L. Wang, Z. Liu, L. Chen, J. Guo, N. Kang, X. L. Ma, H. M. Cheng, W. Ren, *Nat. Mater.*, **2015**, 14, 1135–1141.
[82] M. Naguib, O. Mashtalir, J. Carle, V. Presser, J. Lu, L. Hultman, Y. Gogotsi, M. W. Barsoum, *ACS Nano*, **2012**, 6, 1322–1331.
[83] Y. Wang, J. Wang, G. Han, C. Du, Q. Deng, Y. Gao, G. Yin, Y. Song, *Ceram. Int.*, **2019**, 45, 2411–2417.
[84] B. Anasori, C. Shi, E. J. Moon, Y. Xie, C. A. Voigt, P. R. C. Kent, S. J. May, S. J. L. Billinge, M. W. Barsoum, Y. Gogotsi, *Nanoscale Horiz.*, **2016**, 1, 227–234.
[85] Z. Li, Z. Qi, S. Wang, T. Ma, L. Zhou, Z. Wu, X. Luan, F. Y. Lin, M. Chen, J. T. Miller, H. Xin, W. Huang, Y. Wu, *Nano Lett.*, **2019**, 19, 5102–5108.
[86] A. Feng, T. Hou, Z. Jia, Y. Zhang, F. Zhang, G. Wu, *Nanomaterials*, **2020**, 10, 162.
[87] M. Ghidiu, M. Naguib, C. Shi, O. Mashtalir, L. M. Pan, B. Zhang, J. Yang, Y. Gogotsi, S. J. Billinge, M. W. Barsoum, *Chem. Commun.*, **2014**, 50, 9517–9520.
[88] Y. Xue, J. Feng, S. Huo, P. Song, B. Yu, L. Liu, H. Wang, *Chem. Eng. J.*, **2020**, 397, 125336.
[89] C. Cui, R. Cheng, C. Zhang, X. Wang, *Chin. Chem. Lett.*, **2020**, 31, 988–991.
[90] B. Ahmed, D. H. Anjum, M. N. Hedhili, Y. Gogotsi, H. N. Alshareef, *Nanoscale*, **2016**, 8, 7580–7587.
[91] M. Alhabeb, K. Maleski, T. S. Mathis, A. Sarycheva, C. B. Hatter, S. Uzun, A. Levitt, Y. Gogotsi, *Angew. Chem. Int. Ed.*, **2018**, 57, 5444–5448.
[92] Y. Guan, S. Jiang, Y. Cong, J. Wang, Z. Dong, Q. Zhang, G. Yuan, Y. Li, X. Li, *2D Mater.*, **2020**, 7, 025010.
[93] V. Natu, R. Pai, M. Sokol, M. Carey, V. Kalra, M. W. Barsoum, *Chem*, **2020**, 6, 616–630.
[94] X. Li, M. Li, Q. Yang, G. Liang, Z. Huang, L. Ma, D. Wang, F. Mo, B. Dong, Q. Huang, C. Zhi, *Adv. Energy Mater.*, **2020**, 10, 2001791.
[95] S. Yang, P. Zhang, F. Wang, A. G. Ricciardulli, M. R. Lohe, P. W. M. Blom, X. Feng, *Angew. Chem. Int. Ed.*, **2018**, 57, 15491–15495.
[96] P. Urbankowski, B. Anasori, T. Makaryan, D. Er, S. Kota, P. L. Walsh, M. Zhao, V. B. Shenoy, M. W. Barsoum, Y. Gogotsi, *Nanoscale*, **2016**, 8, 11385–11391.
[97] M. Li, J. Lu, K. Luo, Y. Li, K. Chang, K. Chen, J. Zhou, J. Rosen, L. Hultman, P. Eklund, P. O. Å. Persson, S. Du, Z. Chai, Z. Huang, Q. Huang, *J. Am. Chem. Soc.*, **2019**, 141, 4730–4737.
[98] X. Xie, Y. Xue, L. Li, S. Chen, Y. Nie, W. Ding, Z. Wei, *Nanoscale*, **2014**, 6, 11035–11040.
[99] L. Huang, T. Li, Q. Liu, J. Gu, *Electrochem. Commun.*, **2019**, 104, 106472.
[100] T. Li, L. Yao, Q. Liu, J. Gu, R. Luo, J. Li, X. Yan, W. Wang, P. Liu, B. Chen, W. Zhang, W. Abbas, R. Naz, D. Zhang, *Angew. Chem. Int. Ed.*, **2018**, 57, 6115–6119.
[101] T. Li, X. Yan, L. Huang, J. Li, L. Yao, Q. Zhu, W. Wang, W. Abbas, R. Naz, J. Gu, Q. Liu, W. Zhang, D. Zhang, *J. Mater. Chem. A*, **2019**, 7, 14462–14465.
[102] Y. Chen, X. Xie, X. Xin, Z.-R. Tang, Y.-J. Xu, *ACS Nano*, **2019**, 13, 295–304.
[103] B. Li, R. Ye, Q. Wang, X. Liu, P. Fang, J. Hu, *Ionics*, **2021**, 27, 1221–1231.
[104] J. Wang, Y. Liu, G. Yang, *Mater. Res. Express*, **2019**, 6, 025056.
[105] X. Yu, W. Yin, T. Wang, Y. Zhang, *Langmuir*, **2019**, 35, 2909–2916.
[106] Z. Fan, Y. Wang, Z. Xie, D. Wang, Y. Yuan, H. Kang, B. Su, Z. Cheng, Y. Liu, *Adv. Sci.*, **2018**, 5, 1800750.
[107] P. Lian, Y. Dong, Z.-S. Wu, S. Zheng, X. Wang, W. Sen, C. Sun, J. Qin, X. Shi, X. Bao, *Nano Energy*, **2017**, 40, 1–8.
[108] X. Wang, S. Kajiyama, H. Iinuma, E. Hosono, S. Oro, I. Moriguchi, M. Okubo, A. Yamada, *Nat. Commun.*, **2015**, 6, 6544.
[109] K. Hantanasirisakul, Y. Gogotsi, *Adv. Mater.*, **2018**, 30, 1804779.
[110] X. Zhang, B. Shao, Z. Sun, Z. Gao, Y. Qin, C. Zhang, F. Cui, X. Yang, *Ind. Eng. Chem. Res.*, **2020**, 59, 1822–1828.
[111] Y. Yuan, H. Li, L. Wang, L. Zhang, D. Shi, Y. Hong, J. Sun, *ACS Sustain. Chem. Eng.*, **2019**, 7, 4266–4273.
[112] J. Halim, M. R. Lukatskaya, K. M. Cook, J. Lu, C. R. Smith, L.-Å. Näslund, S. J. May, L. Hultman, Y. Gogotsi, P. Eklund, M. W. Barsoum, *Chem. Mater.*, **2014**, 26, 2374–2381.
[113] P. Wang, H. Cui, C. Wang, *Nano Energy*, **2019**, 66, 104196.
[114] R. Xiao, C. Zhao, Z. Zou, Z. Chen, L. Tian, H. Xu, H. Tang, Q. Liu, Z. Lin, X. Yang, *Appl. Catal. B*, **2020**, 268, 118382.
[115] X. Li, X. Lv, X. Sun, C. Yang, Y.-Z. Zheng, L. Yang, S. Li, X. Tao, *Appl. Catal. B*, **2021**, 284, 119708.
[116] A. Djire, X. Wang, C. Xiao, O. C. Nwamba, M. V. Mirkin, N. R. Neale, *Adv. Funct. Mater.*, **2020**, 30, 2001136.
[117] Y. Wang, Y. Zhou, M. Han, Y. Xi, H. You, X. Hao, Z. Li, J. Zhou, D. Song, D. Wang, F. Gao, *Small*, **2019**, 15, 1805435.
[118] H. Lei, S. Z. Tan, L. Ma, Y. Liu, Y. Liang, M. S. Javed, Z. Wang, Z. Zhu, W. Mai, *ACS Appl. Mater. Interfaces*, **2020**, 12, 44639–44647.
[119] L. Hu, M. Li, X. Wei, H. Wang, Y. Wu, J. Wen, W. Gu, C. Zhu, *Chem. Eng. J.*, **2020**, 398, 125605.
[120] N. C. S. Selvam, J. Lee, G. H. Choi, M. J. Oh, S. Xu, B. Lim, P. J. Yoo, *J. Mater. Chem. A*, **2019**, 7, 27383–27393.
[121] X. Peng, S. Zhao, Y. Mi, L. Han, X. Liu, D. Qi, J. Sun, Y. Liu, H. Bao, L. Zhuo, H. L. Xin, J. Luo, X. Sun, *Small*, **2020**, 16, 2002888.
[122] Z. Pan, L. Kang, T. Li, M. Waqar, J. Yang, Q. Gu, X. Liu, Z. Kou, Z.

Wang, L. Zheng, J. Wang, *ACS Nano*, **2021**, 15, 12975–12987.
[123] S. Y. Pang, Y. T. Wong, S. Yuan, Y. Liu, M. K. Tsang, Z. Yang, H. Huang, W. T. Wong, J. Hao, *J. Am. Chem. Soc.*, **2019**, 141, 9610–9616.
[124] J. Chen, X. Yuan, F. Lyu, Q. Zhong, H. Hu, Q. Pan, Q. Zhang, *J. Mater. Chem. A*, **2019**, 7, 1281–1286.
[125] L. Jiang, J. Duan, J. Zhu, S. Chen, M. Antonietti, *ACS Nano*, **2020**, 14, 2436–2444.
[126] M. Yu, Z. Wang, J. Liu, F. Sun, P. Yang, J. Qiu, *Nano Energy*, **2019**, 63, 103880.
[127] M. Yu, S. Zhou, Z. Wang, J. Zhao, J. Qiu, *Nano Energy*, **2018**, 44, 181–190.
[128] Y. Yoon, A. P. Tiwari, M. Lee, M. Choi, W. Song, J. Im, T. Zyung, H.-K. Jung, S. S. Lee, S. Jeon, K.-S. An, *J. Mater. Chem. A*, **2018**, 6, 20869–20877.
[129] A. D. Handoko, K. D. Fredrickson, B. Anasori, K. W. Convey, L. R. Johnson, Y. Gogotsi, A. Vojvodic, Z. W. Seh, *ACS Appl. Energy Mater.*, **2017**, 1, 173–180.
[130] S. Ma, X. Fan, Y. An, D. Yang, Z. Luo, Y. Hu, N. Guo, *J. Mater. Sci.*, **2019**, 54, 11378–11389.
[131] S. Li, P. Tuo, J. Xie, X. Zhang, J. Xu, J. Bao, B. Pan, Y. Xie, *Nano Energy*, **2018**, 47, 512–518.
[132] Z. Chen, S. Huang, B. Huang, M. Wan, N. Zhou, *Appl. Surf. Sci.*, **2020**, 509, 145319.
[133] C. Y. Liu, E. Y. Li, *ACS Appl. Mater. Interfaces*, **2019**, 11, 1638–1644.
[134] D. Kan, D. Wang, X. Zhang, R. Lian, J. Xu, G. Chen, Y. Wei, *J. Mater. Chem. A*, **2020**, 8, 3097–3108.
[135] Y. Tang, C. Yang, M. Sheng, X. Yin, W. Que, *ACS Sustainable Chem. Eng.*, **2020**, 8, 12990–12998.
[136] C. Ling, L. Shi, Y. Ouyang, J. Wang, *Chem. Mater.*, **2016**, 28, 9026–9032.
[137] D. A. Kuznetsov, Z. Chen, P. V. Kumar, A. Tsoukalou, A. Kierzkowska, P. M. Abdala, O. V. Safonova, A. Fedorov, C. R. Muller, *J. Am. Chem. Soc.*, **2019**, 141, 17809–17816.
[138] D. Kan, R. Lian, D. Wang, X. Zhang, J. Xu, X. Gao, Y. Yu, G. Chen, Y. Wei, *J. Mater. Chem. A*, **2020**, 8, 17065–17077.
[139] B. Huang, N. Zhou, X. Chen, W. J. Ong, N. Li, *Chem. Eur. J.*, **2018**, 24, 18479–18486.
[140] X. Sang, Y. Xie, M. W. Lin, M. Alhabeb, K. L. Van Aken, Y. Gogotsi, P. R. C. Kent, K. Xiao, R. R. Unocic, *ACS Nano*, **2016**, 10, 9193–9200.
[141] H. Lind, B. Wickman, J. Halim, G. Montserrat-Sisó, A. Hellman, J. Rosen, *Adv. Sustainable Syst.*, **2020**, 5, 2000158.
[142] J. Gan, F. Li, Q. Tang, *J. Phys. Chem. Lett.*, **2021**, 12, 4805–4813.
[143] K. Rajavel, X. Yu, P. Zhu, Y. Hu, R. Sun, C. Wong, *ACS Appl. Mater. Interfaces*, **2020**, 12, 49737–49747.
[144] F. Xia, J. Lao, R. Yu, X. Sang, J. Luo, Y. Li, J. Wu, *Nanoscale*, **2019**, 11, 23330–23337.
[145] M. Pandey, K. S. Thygesen, *J. Phys. Chem. C*, **2017**, 121, 13593–13598.
[146] L. Xiu, Z. Wang, M. Yu, X. Wu, J. Qiu, *ACS Nano*, **2018**, 12, 8017–8028.
[147] M. Mahmood, S. Zulfiqar, M. F. Warsi, M. Aadil, I. Shakir, S. Haider, P. O. Agboola, M. Shahid, *Ceram. Int.*, **2022**, 48, 2345–2354.
[148] Y. Zhu, K. Rajouâ, S. Le Vot, O. Fontaine, P. Simon, F. Favier, *Nano Energy*, **2020**, 73, 104734.
[149] Y. Cui, Z. Liu, Y. Zhang, P. Liu, M. Ahmad, Q. Zhang, B. Zhang, *Carbon*, **2021**, 181, 58–68.
[150] M. Q. Zhao, X. Xie, C. E. Ren, T. Makaryan, B. Anasori, G. Wang, Y. Gogotsi, *Adv. Mater.*, **2017**, 29, 1702410.
[151] J. Peng, X. Chen, W.-J. Ong, X. Zhao, N. Li, *Chem*, **2019**, 5, 18–50.
[152] Y. Lee, S. J. Kim, Y.-J. Kim, Y. Lim, Y. Chae, B.-J. Lee, Y.-T. Kim, H. Han, Y. Gogotsi, C. W. Ahn, *J. Mater. Chem. A*, **2020**, 8, 573–581.
[153] S. Doo, A. Chae, D. Kim, T. Oh, T. Y. Ko, S. J. Kim, D. Y. Koh, C. M. Koo, *ACS Appl. Mater. Interfaces*, **2021**, 13, 22855–22865.
[154] Y. Jiang, T. Sun, X. Xie, W. Jiang, J. Li, B. Tian, C. Su, *ChemSusChem*, **2019**, 12, 1368–1373.
[155] J. Zhu, A. Chroneos, J. Eppinger, U. Schwingenschlögl, *Appl. Mater. Today*, **2016**, 5, 19–24.
[156] S. Wang, L. Chen, Y. Wu, Q. Zhang, *ChemPhysChem*, **2018**, 19, 3380–3387.
[157] G. Qu, Y. Zhou, T. Wu, G. Zhao, F. Li, Y. Kang, C. Xu, *ACS Appl. Energy Mater.*, **2018**, 1, 7206–7212.
[158] J. Guan, Z. Duan, F. Zhang, S. D. Kelly, R. Si, M. Dupuis, Q. Huang, J. Q. Chen, C. Tang, C. Li, *Nat. Catal.*, **2018**, 1, 870–877.
[159] J. Deng, H. Li, J. Xiao, Y. Tu, D. Deng, H. Yang, H. Tian, J. Li, P. Ren, X. Bao, *Energy Environ. Sci.*, **2015**, 8, 1594–1601.
[160] Z. Shen, X. Fan, S. Ma, Y. An, D. Yang, N. Guo, Z. Luo, Y. Hu, *Int. J. Hydrogen Energy*, **2020**, 45, 14396–14406.
[161] X. Zhang, L. Chen, Q. Sun, Y. Pang, X. Yang, Z. Yang, *Int. J. Hydrogen Energy*, **2021**, 46, 25457–25467.
[162] P. Li, J. Zhu, A. D. Handoko, R. Zhang, H. Wang, D. Legut, X. Wen, Z. Fu, Z.W. Seh, Q. Zhang, *J Mater. Chem. A*, **2018**, 6, 4271–4278.
[163] J. Gan, F. Li, Y. Tang, Q. Tang, *ChemSusChem*, **2020**, 13, 6005–6015.
[164] C. Cui, R. Cheng, H. Zhang, C. Zhang, Y. Ma, C. Shi, B. Fan, H. Wang, X. Wang, *Adv. Funct. Mater.*, **2020**, 30, 2000693.
[165] V. Ramalingam, P. Varadhan, H. C. Fu, H. Kim, D. Zhang, S. Chen, L. Song, D. Ma, Y. Wang, H. N. Alshareef, J. H. He, *Adv. Mater.*, **2019**, 31, 1903841.
[166] H. Liu, Z. Hu, Q. Liu, P. Sun, Y. Wang, S. Chou, Z. Hu, Z. Zhang, *J. Mater. Chem. A*, **2020**, 8, 24710–24717.
[167] H. Bao, Y. Qiu, X. Peng, J.A. Wang, Y. Mi, S. Zhao, X. Liu, Y. Liu, R. Cao, L. Zhuo, J. Ren, J. Sun, J. Luo, X. Sun, *Nat. Commun.*, **2021**, 12, 238.
[168] Y. Cheng, J. Dai, Y. Song, Y. Zhang, *ACS Appl. Energy Mater.*, **2019**, 2, 6851–6859.
[169] B. Wei, Z. Fu, D. Legut, T. C. Germann, S. Du, H. Zhang, J. S. Francisco, R. Zhang, *Adv. Mater.*, **2021**, 33, 2102595.
[170] Z. Kou, W. Zang, W. Pei, L. Zheng, S. Zhou, S. Zhang, L. Zhang, J. Wang, *J. Mater. Chem. A*, **2020**, 8, 3071–3082.
[171] W. Jiang, X. Zou, H. Du, L. Gan, C. Xu, F. Kang, W. Duan, J. Li, *Chem. Mater.*, **2018**, 30, 2687–2693.
[172] J. Zhang, Y. Zhao, X. Guo, C. Chen, C.-L. Dong, R.-S. Liu, C.-P. Han, Y. Li, Y. Gogotsi, G. Wang, *Nat. Catal.*, **2018**, 1, 985–992.
[173] C. F. Du, X. Sun, H. Yu, Q. Liang, K. N. Dinh, Y. Zheng, Y. Luo, Z. Wang, Q. Yan, *Adv. Sci.*, **2019**, 6, 1900116.
[174] Y. Zhu, G. Xu, W. Song, Y. Zhao, Z. He, Z. Miao, *Ceram. Int.*, **2021**, 47, 30005–30011.
[175] Y.-W. Cheng, J.-H. Dai, Y.-M. Zhang, Y. Song, *J. Phys. Chem. C*, **2018**, 122, 28113–28122.
[176] X. Wang, C. Wang, S. Ci, Y. Ma, T. Liu, L. Gao, P. Qian, C. Ji, Y. Su, *J. Mater. Chem. A*, **2020**, 8, 23488–23497.
[177] T. L. Tan, H. M. Jin, M. B. Sullivan, B. Anasori, Y. Gogotsi, *ACS Nano*, **2017**, 11, 4407–4418.
[178] B. Anasori, Y. Xie, M. Beidaghi, J. Lu, B.C. Hosler, L. Hultman, P. R. C. Kent, Y. Gogotsi, M. W. Barsoum, *ACS Nano*, **2015**, 9, 9507–9516.
[179] C. Lu, L. Yang, B. Yan, L. Sun, P. Zhang, W. Zhang, Z. Sun, *Adv. Funct. Mater.*, **2020**, 30, 2000852.
[180] T. A. Le, Q. V. Bui, N. Q. Tran, Y. Cho, Y. Hong, Y. Kawazoe, H. Lee, *ACS Sustainable Chem. Eng.*, **2019**, 7, 16879–16888.
[181] M. Han, J. Yang, J. Jiang, R. Jing, S. Ren, C. Yan, *J Colloid Interface*

Sci, **2021**, 582, 1099–1106.
[182] S. Zhang, H. Ying, P. Huang, T. Yang, W.-Q. Han, *Nano Res.*, **2022**, 15, 2746–2755.
[183] E. Balcı, Ü. Ö. Akkuş, S. Berber, *J. Mater. Chem. C*, **2017**, 5, 5956–5961.
[184] N. Miao, J. Wang, Y. Gong, J. Wu, H. Niu, S. Wang, K. Li, A. R. Oganov, T. Tada, H. Hosono, *Chem. Mater.*, **2020**, 32, 6947–6957.
[185] Z. Guo, J. Zhou, Z. Sun, *J. Mater. Chem. A*, **2017**, 5, 23530–23535.
[186] B. Zhang, J. Zhou, Z. Guo, Q. Peng, Z. Sun, *Appl. Surf. Sci.*, **2020**, 500, 144248.
[187] X. Liu, X. Ge, Y. Dong, K. Fu, F. Meng, R. Si, M. Zhang, X. Xu, *Mater. Chem. Phys.*, **2020**, 253, 123334.
[188] A. A. Rezaie, Z. Yan, J. P. Scheifers, J. Zhang, J. Guo, B. P. T. Fokwa, *J. Mater. Chem. A*, **2020**, 8, 1646–1651.
[189] Y. Yoon, A. P. Tiwari, M. Choi, T. G. Novak, W. Song, H. Chang, T. Zyung, S. S. Lee, S. Jeon, K. S. An, *Adv. Funct. Mater.*, **2019**, 29, 1903443.
[190] Y. Tang, C. Yang, Y. Tian, Y. Luo, X. Yin, W. Que, *Nanoscale Adv.*, **2020**, 2, 1187–1194.
[191] J. Halim, J. Palisaitis, J. Lu, J. Thörnberg, E. J. Moon, M. Precner, P. Eklund, P. O. Å. Persson, M. W. Barsoum, J. Rosen, *ACS Appl. Nano Mater.*, **2018**, 1, 2455–2460.
[192] N. Chen, Y. Zhou, S. Zhang, H. Huang, C. Zhang, X. Zheng, X. Chu, H. Zhang, W. Yang, J. Chen, *Nano Energy*, **2021**, 85, 106007.
[193] I. C. Onyia, S. O. Ezeonu, D. Bessarabov, K. O. Obodo, *Comp. Mater. Sci.*, **2021**, 197, 110613.
[194] C. Ling, L. Shi, Y. Ouyang, Q. Chen, J. Wang, *Adv. Sci.*, **2016**, 3, 1600180.
[195] E. Toyoda, R. Jinnouchi, T. Hatanaka, Y. Morimoto, K. Mitsuhara, A. Visikovskiy, Y. Kido, *J. Phys. Chem. C*, **2011**, 115, 21236–21240.
[196] M. P. Hyman, J. W. Medlin, *J. Phys. Chem. C*, **2007**, 111, 17052–17060.
[197] R. Zheng, C. Shu, Z. Hou, A. Hu, P. Hei, T. Yang, J. Li, R. Liang, J. Long, *ACS Appl. Mater. Interfaces*, **2019**, 11, 46696–46704.
[198] R. Zheng, C. Shu, Z. Hou, A. Hu, J. Zhao, Y. Guo, M. He, Y. Yan, J. Long, *Carbon*, **2020**, 166, 273–283.
[199] Y. Wang, X. Hu, H. Song, Y. Cai, Z. Li, D. Zu, P. Zhang, D. Chong, N. Gao, Y. Shen, C. Li, *Appl. Catal. B*, **2021**, 299, 120677.
[200] Y. Wang, R. Du, Z. Li, H. Song, Z. Chao, D. Zu, D. Chong, N. Gao, C. Li, *Ceram. Int.*, **2021**, 47, 28321–28327.
[201] X. Xu, Y. Zhang, H. Sun, J. Zhou, Z. Liu, Z. Qiu, D. Wang, C. Yang, Q. Zeng, Z. Peng, S. Guo, *Adv. Mater.*, **2021**, 33, 2100272.
[202] L. Deng, B. Chang, D. Shi, X. Yao, Y. Shao, J. Shen, B. Zhang, Y. Wu, X. Hao, *Renew. Energy*, **2021**, 170, 858–865.
[203] Y. Li, L. Ding, Z. Liang, Y. Xue, H. Cui, J. Tian, *Chem. Eng. J.*, **2020**, 383, 123178.
[204] H. Wang, J.-M. Lee, *J. Mater. Chem. A*, **2020**, 8, 10604–10624.
[205] X. Yang, Q. Jia, F. Duan, B. Hu, M. Wang, L. He, Y. Song, Z. Zhang, *Appl. Surf. Sci.*, **2019**, 464, 78–87.
[206] D. N. Nguyen, G. S. Gund, M. G. Jung, S. H. Roh, J. Park, J. K. Kim, H. S. Park, *ACS Nano*, **2020**, 14, 17615–17625.
[207] W. Yuan, L. Cheng, Y. An, H. Wu, N. Yao, X. Fan, X. Guo, *ACS Sustainable Chem. Eng.*, **2018**, 6, 8976–8982.
[208] J. Liu, Y. Liu, D. Xu, Y. Zhu, W. Peng, Y. Li, F. Zhang, X. Fan, *Appl. Catal. B*, **2019**, 241, 89–94.
[209] L. Xiu, W. Pei, S. Zhou, Z. Wang, P. Yang, J. Zhao, J. Qiu, *Adv. Funct. Mater.*, **2020**, 30, 1910028.
[210] T. P. Nguyen, S. Y. Kim, T. H. Lee, H. W. Jang, Q. V. Le, I. T. Kim, *Appl. Surf. Sci.*, **2020**, 504, 144389.
[211] M. Li, Y. Wang, T. Li, J. Li, L. Huang, Q. Liu, J. Gu, D. Zhang, *J. Mater. Chem. A*, **2021**, 9, 922–927.
[212] B. Shen, H. Huang, H. Liu, Q. Jiang, H. He, *Int. J. Hydrogen Energy*, **2021**, 46, 29984–29993.
[213] Y. Tan, Z. Zhu, X. Zhang, J. Zhang, Y. Zhou, H. Li, H. Qin, Y. Bo, Z. Pan, *Int. J. Hydrogen Energy*, **2021**, 46, 1955–1966.
[214] C. J. Zhang, S. Pinilla, N. McEvoy, C. P. Cullen, B. Anasori, E. Long, S.-H. Park, A. Seral-Ascaso, A. Shmeliov, D. Krishnan, C. Morant, X. Liu, G. S. Duesberg, Y. Gogotsi, V. Nicolosi, *Chem. Mater.*, **2017**, 29, 4848–4856.
[215] J. Zhu, L. Hu, P. Zhao, L. Y. S. Lee, K.-Y. Wong, *Chem. Rev.*, **2020**, 120, 851–918.
[216] L. Yan, X. Chen, X. Liu, L. Chen, B. Zhang, *J. Mater. Chem. A*, **2020**, 8, 23637–23644.
[217] Z. P. Wu, X. F. Lu, S. Q. Zang, X. W. Lou, *Adv. Funct. Mater.*, **2020**, 30, 1910274.
[218] X. Ding, X. Wang, W. Song, X. Wei, J. Zhu, Y. Tang, M. Wang, *New J. Chem.*, **2021**, 45, 21905–21911.
[219] Y. Sun, D. Jin, Y. Sun, X. Meng, Y. Gao, Y. Dall'Agnese, G. Chen, X.-F. Wang, *J. Mater. Chem. A*, **2018**, 6, 9124–9131.
[220] D. Guo, X. Li, Y. Jiao, H. Yan, A. Wu, G. Yang, Y. Wang, C. Tian, H. Fu, *Nano Res.*, **2021**, 15, 238–247.
[221] J. Wang, X. Wei, W. Song, X. Shi, X. Wang, W. Zhong, M. Wang, J. Ju, Y. Tang, *ChemSusChem*, **2021**, 14, 1948–1954.
[222] P. Nayak, Q. Jiang, R. Mohanraman, D. Anjum, M. N. Hedhili, H. N. Alshareef, *Nanoscale*, **2018**, 10, 17030–17037.
[223] Z. Yuan, L. Wang, J. Cao, L. Zhao, W. Han, *Adv. Mater. Interfaces*, **2020**, 7, 2001449.
[224] C. Zhang, B. Ma, Y. Zhou, C. Wang, *J. Electroanal. Chem.*, **2020**, 865, 114142.
[225] Z. Zhang, H. Li, G. Zou, C. Fernandez, B. Liu, Q. Zhang, J. Hu, Q. Peng, *ACS Sustainable Chem. Eng.*, **2016**, 4, 6763–6771.
[226] Z. Lv, M. Wang, D. Liu, K. Jian, R. Zhang, J. Dang, *Inorg. Chem.*, **2021**, 60, 1604–1611.
[227] K. Xiong, L. Li, L. Zhang, W. Ding, L. Peng, Y. Wang, S. Chen, S. Tan, Z. Wei, *J. Mater. Chem. A*, **2015**, 3, 1863–1867.
[228] Z. Li, Y. Cui, Z. Wu, C. Milligan, L. Zhou, G. Mitchell, B. Xu, E. Shi, J. T. Miller, F. H. Ribeiro, Y. Wu, *Nat. Catal.*, **2018**, 1, 349–355.
[229] S. Penner, D. Wang, D. S. Su, G. Rupprechter, R. Podloucky, R. Schlögl, K. Hayek, *Surf. Sci.*, **2003**, 532–535, 276–280.
[230] Z. Li, L. Yu, C. Milligan, T. Ma, L. Zhou, Y. Cui, Z. Qi, N. Libretto, B. Xu, J. Luo, E. Shi, Z. Wu, H. Xin, W. N. Delgass, J. T. Miller, Y. Wu, *Nat. Commun.*, **2018**, 9, 5258.
[231] J. D. Benck, T. R. Hellstern, J. Kibsgaard, P. Chakthranont, T. F. Jaramillo, *ACS Catal.*, **2014**, 4, 3957–3971.
[232] J. You, C. Si, J. Zhou, Z. Sun, *J. Phys. Chem. C*, **2019**, 123, 3719–3726.
[233] L. Hu, Y. Sun, S.-J. Gong, H. Zong, K. Yu, Z. Zhu, *New J. Chem.*, **2020**, 44, 7902–7911.
[234] J. Liang, C. Ding, J. Liu, T. Chen, W. Peng, Y. Li, F. Zhang, X. Fan, *Nanoscale*, **2019**, 11, 10992–11000.
[235] X.-D. Zhu, Y. Xie, Y.-T. Liu, *J. Mater. Chem. A*, **2018**, 6, 21255–21260.
[236] X. Wu, Z. Wang, M. Yu, L. Xiu, J. Qiu, *Adv. Mater.*, **2017**, 29, 1607017.
[237] M. Benchakar, V. Natu, T. A. Elmelegy, M. Sokol, J. Snyder, C. Comminges, C. Morais, S. Célérier, A. Habrioux, M. W. Barsoum, *J. Electrochem. Soc.*, **2020**, 167, 124507.
[238] K. R. G. Lim, A. D. Handoko, L. R. Johnson, X. Meng, M. Lin, G. S. Subramanian, B. Anasori, Y. Gogotsi, A. Vojvodic, Z. W. Seh, *ACS Nano*, **2020**, 14, 16140–16155.
[239] N. H. Attanayake, S. C. Abeyweera, A. C. Thenuwara, B. Anasori, Y. Gogotsi, Y. Sun, D. R. Strongin, *J. Mater. Chem. A*, **2018**, 6, 16882–16889.

[240] Q. Xiong, Y. Wang, P.-F. Liu, L.-R. Zheng, G. Wang, H.-G. Yang, P.-K. Wong, H. Zhang, H. Zhao, *Adv. Mater*., **2018**, 30, 1801450.
[241] X. Dai, K. Du, Z. Li, M. Liu, Y. Ma, H. Sun, X. Zhang, Y. Yang, *ACS Appl. Mater. Inter*., **2015**, 7, 27242–27253.
[242] C. K. Chua, A. H. Loo, M. Pumera, *Chem.-Eur. J*., **2016**, 22, 14336–14341.
[243] G. Li, D. Zhang, Q. Qiao, Y. Yu, D. Peterson, A. Zafar, R. Kumar, S. Curtarolo, F. Hunte, S. Shannon, Y. Zhu, W. Yang, L. Cao, *J. Am. Chem. Soc*., **2016**, 138, 16632–16638.
[244] S. Li, X. Que, X. Chen, T. Lin, L. Sheng, J. Peng, J. Li, M. Zhai, *ACS Appl. Energy Mater*., **2020**, 3, 10882–10891.
[245] P. Kuang, M. He, B. Zhu, J. Yu, K. Fan, M. Jaroniec, *J. Catal*., **2019**, 375, 8–20.
[246] H. Jiang, Z. Wang, Q. Yang, L. Tan, L. Dong, M. Dong, *Nano-Micro Lett.*, **2019**, 11, 31.
[247] E. German, R. Gebauer, *Appl. Surf. Sc*i., **2020**, 528, 146591.
[248] N. Li, Y. Zhang, M. Jia, X. Lv, X. Li, R. Li, X. Ding, Y.-Z. Zheng, X. Tao, *Electrochim. Acta,* **2019**, 326, 134976.
[249] J. Chu, F. Wang, L. Yin, L. Lei, C. Yan, F. Wang, Y. Wen, Z. Wang, C. Jiang, L. Feng, J. Xiong, Y. Li, J. He, *Adv. Funct. Mater*., **2017**, 27, 1701342.
[250] C.-F. Du, K. N. Dinh, Q. Liang, Y. Zheng, Y. Luo, J. Zhang, Q. Yan, *Adv. Energy Mater*., **2018**, 8, 1801127.
[251] J. Masud, A. T. Swesi, W. P. R. Liyanage, M. Nath, *ACS Appl. Mater. Inter*., **2016**, 8, 17292–17302.
[252] A. Dutta, N. Pradhan, *J. Phys. Chem. Lett.*, **2017**, 8, 144–152.
[253] A. Dutta, A. K. Samantara, S. K. Dutta, B. K. Jena, N. Pradhan, *ACS Energy Lett.*, **2016**, 1, 169–174.
[254] L.-A. Stern, L. Feng, F. Song, X. Hu, *Energy Environ. Sci.*, **2015**, 8, 2347–2351.
[255] O. Mabayoje, A. Shoola, B. R. Wygant, C. B. Mullins, *ACS Energy Lett*., **2016**, 1, 195–201.
[256] S. Jin, *ACS Energy Lett*., **2017**, 2, 1937–1938.
[257] M. S. Burke, L. J. Enman, A. S. Batchellor, S. Zou, S. W. Boettcher, *Chem. Mater*., **2015**, 27, 7549–7558.
[258] L. Yan, B. Zhang, S. Wu, J. Yu, *J. Mater. Chem. A*, **2020**, 8, 14234–14242.
[259] Y. Cheng, Y. Zhang, Y. Li, J. Dai, Y. Song, *J. Mater. Chem. A*, **2019**, 7, 9324–9334.
[260] Q. Yue, J. Sun, S. Chen, Y. Zhou, H. Li, Y. Chen, R. Zhang, G. Wei, Y. Kang, *ACS Appl. Mater. Interfaces*, **2020**, 12, 18570–18577.
[261] W. Gao, Y. Shi, Y. Zhang, L. Zuo, H. Lu, Y. Huang, W. Fan, T. Liu, *ACS Sustainable Chem. Eng*., **2016**, 4, 6313–6321.
[262] T. Meng, L. Zheng, J. Qin, D. Zhao, M. Cao, *J. Mater. Chem. A*, **2017**, 5, 20228–20238.
[263] X. Wu, S. Zhou, Z. Wang, J. Liu, W. Pei, P. Yang, J. Zhao, J. Qiu, *Adv. Energy Mater*., **2019**, 9, 1901333.
[264] X. Li, Q. Jiang, S. Dou, L. Deng, J. Huo, S. Wang, *J. Mater. Chem. A*, **2016**, 4, 15836–15840.
[265] S. Li, S. Peng, L. Huang, X. Cui, A. M. Al-Enizi, G. Zheng, *ACS Appl. Mater. Interfaces*, **2016**, 8, 20534–20539.
[266] Y. Wen, Z. Wei, C. Ma, X. Xing, Z. Li, D. Luo, *Nanomaterials*, **2019**, 9,775.
[267] L. Zhao, B. Dong, S. Li, L. Zhou, L. Lai, Z. Wang, S. Zhao, M. Han, K. Gao, M. Lu, X. Xie, B. Chen, Z. Liu, X. Wang, H. Zhang, H. Li, J. Liu, H. Zhang, X. Huang, W. Huang, *ACS Nano*, **2017**, 11, 5800–5807.
[268] X. Zheng, X. Cao, Z. Sun, K. Zeng, J. Yan, P. Strasser, X. Chen, S. Sun, R. Yang, *Appl. Catal. B*, **2020**, 272, 118967.
[269] W.-T. Wang, N. Batool, T.-H. Zhang, J. Liu, X.-F. Han, J.-H. Tian, R. Yang, *J. Mater. Chem. A*, **2021**, 9, 3952–3960.
[270] L. He, J. Liu, B. Hu, Y. Liu, B. Cui, D. Peng, Z. Zhang, S. Wu, B. Liu, *J. Power Sources*, **2019**, 414, 333–344.
[271] L. Wang, J. Zhang, Y. Zhu, S. Xu, C. Wang, C. Bian, X. Meng, F.-S. Xiao, *ACS Catal*., **2017**, 7, 7461–7465.
[272] B. Cui, B. Hu, J. Liu, M. Wang, Y. Song, K. Tian, Z. Zhang, L. He, *ACS Appl. Mater. Interfaces*, **2018**, 10, 23858–23873.
[273] Z. Wang, K. Yu, Y. Feng, R. Qi, J. Ren, Z. Zhu, *Appl. Surf. Sci.*, **2019**, 496, 143729.
[274] Q. Xue, Z. Pei, Y. Huang, M. Zhu, Z. Tang, H. Li, Y. Huang, N. Li, H. Zhang, C. Zhi, *J. Mater. Chem. A*, **2017**, 5, 20818–20823.
[275] Y. Lu, D. Fan, Z. Chen, W. Xiao, C. Cao, X. Yang, *Sci. Bull*., **2020**, 65, 460–466.
[276] K. Zhao, X. Ma, S. Lin, Z. Xu, L. Li, *ChemistrySelect*, **2020**, 5, 1890–1895.
[277] C. F. Du, X. Sun, H. Yu, W. Fang, Y. Jing, Y. Wang, S. Li, X. Liu, Q. Yan, *InfoMat*, **2020**, 2, 950–959.
[278] N. Li, S. Wei, Y. Xu, J. Liu, J. Wu, G. Jia, X. Cui, *Electrochim. Acta*, **2018**, 290, 364–368.
[279] Y. Wen, Z. Wei, J. Liu, R. Li, P. Wang, B. Zhou, X. Zhang, J. Li, Z. Li, *J. Energy Chem*., **2021**, 52, 412–420.
[280] C. Hao, Y. Wu, Y. An, B. Cui, J. Lin, X. Li, D. Wang, M. Jiang, Z. Cheng, S. Hu, *Mater. Today Energy*, **2019**, 12, 453–462.
[281] M. Tian, Y. Jiang, H. Tong, Y. Xu, L. Xia, *ChemNanoMat*, **2019**, 6, 154–159.
[282] M. Benchakar, T. Bilyk, C. Garnero, L. Loupias, C. Morais, J. Pacaud, C. Canaff, P. Chartier, S. Morisset, N. Guignard, V. Mauchamp, S. Célérier, A. Habrioux, *Adv. Mater. Interfaces*, **2019**, 6, 1901328.
[283] N. Hao, Y. Wei, J. Wang, Z. Wang, Z. Zhu, S. Zhao, M. Han, X. Huang, *RSC Adv.*, **2018**, 8, 20576–20584.
[284] L. Bai, J. Guan, *Sustain. Energy Fuels*, **2018**, 2, 2160–2164.
[285] J. Guan, X. Wen, Q. Zhang, Z. Duan, *Carbon*, **2020**, 164, 121–128.
[286] X. Chia, M. Pumera, *Nat. Catal*., **2018**, 1, 909–921.
[287] S. Zhou, X. Yang, W. Pei, N. Liu, J. Zhao, *Nanoscale*, **2018**, 10, 10876–10883.
[288] P. Paul, P. Chakraborty, T. Das, D. Nafday, T. Saha-Dasgupta, *Phy. Rev. B*, **2017**, 96, 035435.
[289] Y. Aierken, C. Sevik, O. Gülseren, F. M. Peeters, D. Çakır, *J. Mater. Chem. A*, **2018**, 6, 2337–2345.
[290] Y. T. Du, X. Kan, F. Yang, L. Y. Gan, U. Schwingenschlogl, *ACS Appl. Mater. Interfaces*, **2018**, 10, 32867–32873.
[291] Y. Lei, N. Tan, Y. Zhu, D. Huo, S. Sun, Y. Zhang, G. Gao, *J. Electrochem. Soc*., **2020**, 167, 116503.
[292] S. Li, Y. Wang, H. Wang, Q. Zhang, Z. Zhang, H. Liu, *J. Appl. Electrochem*., **2021**, 51, 871–878.
[293] P. Zhang, R. Wang, T. Xiao, Z. Chang, Z. Fang, Z. Zhu, C. Xu, L. Wang, J. Cheng, *Energy Technol.*, **2020**, 8, 2000306.
[294] X. Wang, S. Wang, J. Qin, X. Xie, R. Yang, M. Cao, *Inorg. Chem*., **2019**, 58, 16524–16536.
[295] Y. Zhang, H. Jiang, Y. Lin, H. Liu, Q. He, C. Wu, T. Duan, L. Song, *Adv. Mater. Interfaces*, **2018**, 5, 1800392.
[296] D. Xiang, C. Han, J. Wu, S. Zhong, Y. Liu, J. Lin, X. A. Zhang, W. Ping Hu, B. Ozyilmaz, A. H. Neto, A. T. Wee, W. Chen, *Nat. Commun*., **2015**, 6, 6485.
[297] P. Chen, N. Li, X. Chen, W.-J. Ong, X. Zhao, *2D Mater*., **2017**, 5, 014002.
[298] X. Ren, J. Zhou, X. Qi, Y. Liu, Z. Huang, Z. Li, Y. Ge, S. C. Dhanabalan, J. S. Ponraj, S. Wang, J. Zhong, H. Zhang, *Adv. Energy Mater*., **2017**, 7, 1700396.
[299] H. Liu, Y. Du, Y. Deng, P. D. Ye, *Chem. Soc. Rev*., **2015**, 44, 2732–2743.
[300] P. Nakhanivej, X. Yu, S. K. Park, S. Kim, J. Y. Hong, H. J. Kim, W. Lee, J. Y. Hwang, J. E. Yang, C. Wolverton, J. Kong, M. Chhowalla,

H. S. Park, *Nat. Mater.*, **2019**, 18, 156–162.
[301] R. Meng, J. Huang, Y. Feng, L. Zu, C. Peng, L. Zheng, L. Zheng, Z. Chen, G. Liu, B. Chen, Y. Mi, J. Yang, *Adv. Energy Mater.*, **2018**, 8, 1801514.
[302] X. Xie, S. Chen, W. Ding, Y. Nie, Z. Wei, *Chem. Commun.*, **2013**, 49, 10112–10114.
[303] R. Wang, Z. Chang, Z. Fang, T. Xiao, Z. Zhu, B. Ye, C. Xu, J. Cheng, *Int. J. Hydrogen Energy*, **2020**, 45, 28190–28195.
[304] C. Xu, C. Fan, X. Zhang, H. Chen, X. Liu, Z. Fu, R. Wang, T. Hong, J. Cheng, *ACS Appl. Mater. Interfaces*, **2020**, 12, 19539–19546.
[305] L. Chen, Y. Lin, J. Fu, J. Xie, R. Chen, H. Zhang, *ChemElectroChem*, **2018**, 5, 3307–3314.
[306] Y. Wen, C. Ma, Z. Wei, X. Zhu, Z. Li, *RSC Adv.*, **2019**, 9, 13424–13430.
[307] Z. Li, Z. Zhuang, F. Lv, H. Zhu, L. Zhou, M. Luo, J. Zhu, Z. Lang, S. Feng, W. Chen, L. Mai, S. Guo, *Adv. Mater.*, **2018**, 30, 1803220.
[308] H. Parse, I. M. Patil, A. S. Swami, B. A. Kakade, *ACS Appl. Nano Mater.*, **2021**, 4, 1094–1103.
[309] J. Liu, L. Mi, Y. Xing, T. Wang, F. Wang, *Renew. Energy*, **2020**, 160, 1168–1173.
[310] Z. Wu, H. Wang, P. Xiong, G. Li, T. Qiu, W.B. Gong, F. Zhao, C. Li, Q. Li, G. Wang, F. Geng, *Nano Lett.*, **2020**, 20, 2892–2898.
[311] Z. Zeng, G. Fu, H. B. Yang, Y. Yan, J. Chen, Z. Yu, J. Gao, L. Y. Gan, B. Liu, P. Chen, *ACS Mater. Lett.*, **2019**, 1, 432–439.

过渡金属碳氮化物在电催化领域的应用：改性和杂化

白　雪, 管景奇*
吉林大学化学学院, 物理化学研究所, 吉林长春130021

摘要: 化石能源过度消耗导致的环境污染问题使发展绿色可持续替代能源成为人们需要面对的重要问题. 寻找绿色高效的方法生产可再生燃料是一个有效的策略, 在减少二氧化碳排放的同时可满足能源需求. 电催化是一种实现清洁能源的重要途径, 可将地球上含量丰富的H_2O, N_2, CO_2和O_2等转化为燃料和化合物. 尽管贵金属Pt, RuO_2等具有优异的电催化性能, 但由于成本高、储量少限制了其大规模应用, 因此开发一种高活性且低成本的电催化剂是实现大规模应用的关键. 由于具有独特的形貌和电子结构, 石墨烯, 黑磷和二硫化钼等二维材料已经在电催化领域得到了广泛应用. 作为一种新型的二维材料, 碳化物、氮化物和碳氮化物(MXenes)不仅具有良好的机械性能和大比表面积, 其较好的导电性和基底面上丰富的活性位点在促进可持续能源发展方面发挥了更重要的作用. 自MXenes首次被用于析氢反应(HER)以来, 大量的工作预测并合成了具有多种元素的MXenes及其复合材料, 并用于电催化反应.

本文从理论和实验两方面综述了基于MXenes在HER、析氧反应(OER)和氧还原反应(ORR)方面的研究进展, 包括对原始MXenes的结构形态调控和对杂化MXenes的修饰. 简要介绍了MXenes的蚀刻合成法(氢氟酸蚀刻、熔融盐蚀刻和电化学蚀刻等), 提出了设计MXene基电催化剂的基本原则(提高稳定性、导电性和固有活性)并将其电催化性能与M, X, T和空位以及形貌的关系进行了总结. 对于HER, 原始MXene表面的氧官能团是活性位点, 通过调节M, X和空位的类型可以调节表面氧原子的电子结构, 从而使氢吸附吉布斯自由能趋于零, 提高MXene的固有活性. 对于OER和ORR, 原始MXene不具备固有催化活性, 然而某些金属(Pt, Ru等)在T位上以单原子形式掺杂从而形成的MXene基单原子催化剂表现出良好的催化性能. 在总结了原子取代、功能修饰、缺陷工程和形貌控制等方面的研究策略后, 重点讨论了MXenes与金属纳米颗粒、氧化物、氢氧化物、硫化物、磷化物等其他纳米结构异质结的构建. 最后提出了MXenes目前面临的问题和挑战, 并展望了其在电催化领域的应用前景.

关键词: 析氢反应; 过渡金属碳氮化物; 析氧反应; 氧还原反应; 水分解

收稿日期: 2021-12-25. 接受日期: 2022-01-28. 上网时间: 2022-06-20.
*通讯联系人. 电子信箱: guanjq@jlu.edu.cn
基金来源: 国家自然科学基金(22075099); 吉林省教育厅(JJKH20220967KJ).
本文的电子版全文由Elsevier出版社在ScienceDirect上出版(http://www.sciencedirect.com/journal/chinese-journal-of-catalysis).